ABSTRACT

Title: THE IMPACT OF UPPER-LEVEL PROCESSES ON THE INTENSITY AND STRUCTURAL CHANGES OF HURRICANE SANDY (2012)

JungHoon Shin, Doctor of Philosophy, 2016

Directed By: Professor Da-Lin Zhang
Department of Atmospheric and Oceanic Science

The first part of this study examines the relative roles of frontogenesis and tropopause undulation in determining the intensity and structural changes of Hurricane Sandy (2012) using a high-resolution cloud-resolving model. A 138-h simulation reproduces Sandy's four distinct development stages: (i) rapid intensification, (ii) weakening, (iii) steady maximum surface wind but with large continued sea-level pressure (SLP) falls, and (iv) re-intensification. Results show typical correlations between intensity changes, sea-surface temperature and vertical wind shear during the first two stages. The large SLP falls during the last two stages are mostly caused by Sandy's moving northward into lower-tropopause regions associated with an eastward-propagating midlatitude trough, where the associated lower-stratospheric warm air wraps into the storm and its surrounding areas. The steady maximum surface wind occurs because of the widespread SLP falls with weak pressure gradients lacking significant inward advection of absolute angular momentum (AAM). Meanwhile, there is a continuous frontogenesis in the outer region during the last three stages. Cyclonic inward advection of AAM along each frontal rainband accounts for the continued expansion of the tropical-storm-force wind and structural changes, while deep convection in the eyewall and merging of the

final two survived frontal rainbands generate a spiraling jet in Sandy's northwestern quadrant, leading to its re-intensification prior to landfall.

The physical, kinematic and dynamic aspects of an upper-level outflow layer and its possible impact on the re-intensification of Sandy are examined in the second part of this study. Above the outflow layer isentropes are tilted downward with radius as a result of the development of deep convection and an approaching upper-level trough, causing weak subsidence. Its maximum outward radial velocity is located above the cloud top, so the outflow channel experiences cloud-induced long-wave cooling. Because Sandy has two distinct convective regions (an eyewall and a frontal rainband), it has multiple outflow layers, with the eyewall's outflow layer located above that of the frontal rainband. During the re-intensification stage, the eyewall's outflow layer interacts with a jet stream ahead of the upper-level trough axis. Because of the presence of inertial instability on the anticyclonic side of the jet stream and symmetric instability in the inner region of the outflow layer, Sandy's secondary circulation intensifies. Its re-intensification ceases when these instabilities disappear. The relationship between the intensity of the secondary circulation and dynamic instabilities of the outflow layer suggests that the re-intensification occurs in response to these instabilities. Additionally, it is verified that the long-wave cooling in the outflow layer helps induce symmetric instability by reducing static stability.

THE IMPACT OF UPPER-LEVEL PROCESSES ON THE INTENSITY AND STRUCTURAL CHANGES OF HURRICANE SANDY (2012)

By

JungHoon Shin

Dissertation submitted to the Faculty of the Graduate School of the
University of Maryland, College Park, in partial fulfillment
of the requirements for the degree of
Doctor of Philosophy
2016

Advisory Committee:
Professor Da-Lin Zhang, Chair
Professor Tao Yang (Dean's Representative)
Professor Daryl Kleist
Professor Xin-Zhong Liang
Professor Kayo Ide

Acknowledgement

First of all, I would like to thank my advisor, Dr. Da-Lin Zhang who guided my research for a long time. I have learned not only scientific knowledge but also scientific mind from him, which gave me an opportunity to grow as a scientist. I also thank my research group members Hua, Stefan, Lin, Wallace, William, Nancy, Daniel, Xin, and Dr. Chanh Kieu, because I also learned a lot from them. Above all, thanks to my mother and father who always concern and support me.

A part of my dissertation is come from "The impact of moist frontogenesis and tropopause undulation on the intensity, size and structural changes of Hurricane Sandy (2012)" which was submitted to *Journal of the Atmospheric Sciences*. My Ph.D study was supported by NASA Grant NNX12AJ78G. The Gridded satellite (GridSat-B1) data, developed by Knapp et al. (2011) of NOAA CDR Program, was downloaded from National Climatic Data Center (http://www.ncdc.noaa.gov).

Table of Contents

List of Figures

Chapter 1. Introduction

1.1. Background

It is well known that the structural and intensity changes of tropical cyclones (TCs) involve multiscale interactions ranging from planetary waves to mesoscale convective systems (MCSs), cloud microphysics (Zhu and Zhang 2006; Tao et al. 2011), and cloud-radiation interaction (Bu et al. 2014). They are determined by various environmental parameters such as sea surface temperature (SST), vertical wind shear (VWS; Frank and Ritchie 1999; Kieu and Zhang 2008; Riemer et al. 2010), low-level humidity (Kaplan and DeMaria 2003), and some internal processes (e.g., convective bursts; Heymsfield et al. 2001; Chen and Zhang 2013), as well as structural changes such as eyewall replacement cycle, and spiral rainbands (Willoughby et al. 1982; Powell 1990a, b; Zhu et al. 2004; Wang 2009; Sitkowski et al. 2011; Carrasco et al. 2014).

Several studies have examined the influences of storm sizes on the intensity change of TCs. From the statistical study by using the second generation North Atlantic hurricane database (HURDAT2) and extended best-track dataset, Carrasco et al. (2014) found a negative correlation between the radius of maximum wind (RMW) (or 34-knot wind radius) and rapid intensification (RI) of TCs. That is, TCs with small size have great likelihood to experience RI. An idealized TC simulation study of Wang (2009) showed that the expansion of low pressure areas of TCs can reduce the maximum wind near the RMW by decreasing the pressure gradient force.

Some attention has recently been paid to the importance of upper-level process in the TC intensity change. In the Carnot engine theory, Emanuel (1986) showed that the tropopause temperature is an important parameter in determining the heat engine efficiency and the intensity of TCs. In the global view, it has been proposed that colder temperatures in the upper troposphere or the lower tropopause may increase the potential intensity of TCs (Vecchi et al. 2013). Zhang and Chen (2012) showed the influence of the lower stratospheric warming on the RI of Hurricane Wilma (2005). By utilizing an idealized WRF model with constant SST, Wang et al. (2014) found that under the radiative-convective equilibrium condition, the maximum intensity of TCs increases by about 0.4 m s^{-1} when the tropopause temperature decreases by 1K. Molinari and Vollaro (1989) noted that because of the weak inertial stability of an outflow layer, TCs could be easily influenced by their environments. Rappin et al. (2011) studied the influence of an upper-level jet stream on the outflow channel of a TC. They found that weak inertial stability at the vicinity of the upper-level jet provides less resistance for the outflow channel of the eyewall convection. As a result, if the environmental inertial stability is reduced by the approaching of an upper-level jet stream, the outflow curvature will be reduced, allowing more stretched outflow patterns. Similarly, when an upper-level trough approaches a TC, it can increase the outflow or spin up the TC vortex through the eddy momentum flux (Molinari and Vollaro 1989; Molinari et al. 2006). From the case study of TC Dora (2007), Leroux et al. (2013) argued that the inward cyclonic potential vorticity (PV) flux in the 200-500-hPa layer associated with an approaching trough can spin up and

intensify the storm. However, the influence of inertial instability on TCs is not well examined by previous studies.

Zhang and Chen (2012), and Chen and Zhang (2013) have shown the importance of the upper-level warming in the rapid intensification (RI) of Hurricane Wilma (2005). By utilizing the hydrostatic equation, they concluded that it is the upper-level (or lower stratospheric) warming above 380-K isentropic surface (~12 km height) that causes the RI of Wilma. This strong warming is induced by the compensating subsidence associated with convective bursts.

Recently, it has been suggested that radiative process may affect the structure and evolution of mature TCs and its outflow layer (Bu et al. 2014; Molinari et al. 2014; Molinari and Vollaro 2014; Dunion et al. 2014; Tang and Zhang 2016). Because long-wave radiative cooling has a tendency to reduce stability and increase relative humidity, it facilitates convective development (Melhauser and Zhang 2014). For this reason, both idealized (Bu et al. 2014) and real case (Tang and Zhang 2016) TC simulation studies showed that long-wave cooling invigorates deep convection in the outer regions, resulting in a lager storm and a stronger secondary circulation. From the observational data of Hurricane Ivan (2004), Molinari et al. (2014) verified that the turbulent outflow layer, where bulk Richardson number (R_B) is low, was present above the cirrus base and within central dense overcast (CDO). They suggested that the radiative cooling at the cloud top reduces the static stability, leading to the formation of turbulence. From the composite dropsonde data of Atlantic hurricanes between 1998 and 2011, Duran and Molinari (2016) showed that low R_B was more frequently observed in hurricanes than tropical storms or depressions. Dunion et al.

(2014) suggested that long-wave cooling in the outflow layer may reduce the resistance of the outflow channel by reducing the PV through the static stability. Morinali and Vollaro (2014) also hypothesized that radiative process within the outflow layer can affect the slope of isentropes.

It is well known that the roles of low-level processes in determining the intensity change of TCs have been extensively studied. However, the influence of upper-level processes has received much less attention by the TC research community due to the lack of observational data. This is especially true for TCs moving to the middle latitudes, which experience the so-called extratropical transition (ET) – a process in which warm-core and non-frontal TCs are transformed into cold-core and frontal extratropical cyclones (Jones et al. 2003).

Although there is not a universal definition of ET, the ET of a tropical cyclone (TC) often involves losing symmetric appearance, increasing radius of gale forced winds, increasing central sea-level pressure (SLP), weakening or vertical tilting of a warm core, transformation from a warm to a cold core, and the appearance of a frontal structure under the influences of decreasing sea-surface temperature (SST), and increasing vertical wind shear (VWS) and baroclinicity (Klein et al. 2000; Jones et al. 2003). Perhaps the most prominent structural change of an ET TC is the development of an extensive coverage of clouds and precipitation associated with warm frontogenesis when it interacts with low-level baroclinicity to the north (Harr and Elsberry 2000; Klein et al 2000; Atallah and Bosart 2003; Colle 2003). After its warm core is replaced by a cold core, the TC may appear like an extratropical cyclone (Evans and Hart 2008). In some cases, the lower-tropospheric warm core could still

be retained during ET (Browning et al. 1998; Thorncroft and Jones 2000; Evans and Hart 2003), which resembles a warm-core seclusion that is similar to that described in the conceptual model of Shapiro and Keyser (1990) for a mature extratropical cyclone (Galarneau et al. 2013). Re-intensification of these systems, as often measured by central SLP drops, may occur in response to interaction with upper-level troughs (Harr and Elsberry 2000; Klein et al. 2000; Ritchie and Elsberry 2007).

Despite considerable research, ET is still a challenging subject due to the complex interaction mechanism between a warm-core TC and midlatitude baroclinic systems. Specifically, as shown in Torn et al. (2015), the interaction between the upper-level disturbances (jet streams or troughs/ridges) and TCs during ET could reduce the predictability of transforming storms. Although strong VWS generated by an upper-level jet stream/trough may bring negative impact on the intensity of TCs, some studies have shown that such an upper-level system can intensify the storm by facilitating the upper-level divergence (Klein et al. 2002; Evans and Prater-Mayes 2004). As shown in the ET case of Hurricane Irene (1999), the upper-level jet entrance region of an approaching trough can contribute to the re-intensification of the transforming TC. The upper-level jet stream could also modify the environmental inertial stability that affects the intensity of TCs (Rappin et al. 2011). Not only the upper-level jet stream, but also a upper-level trough (i.e., tropopause undulation) has a great potential that could bring a huge impact on TCs, because some previous research studied the interaction between the tropopause undulation and the transforming TCs (Bosart and Lackmann 1995; Atallah and Bosart 2003). In short, ET processes provides valuable opportunities to investigate the roles of various

upper-level disturbances and processes in determining the intensity and structural changes of TCs.

Although previous studies showed some interesting results, some aspects associated with the upper-level processes are not studied or verified yet, which are given below.

1. What is the impact of lower-stratospheric warm air associated with tropopause undulation?

Hirschberg and Fritsch (1991a, b) already verified the influence of lower-stratospheric warm air on extratropical cyclogenesis, but its effect on the transforming TCs is not validated. Because TCs are easily influenced by the upper-level trough during ET, there is high possibility that stratospheric warm air affects storms.

2. What is the detailed structure of the outflow for TCs undergoing transformations?

Although Molinari et al. (2014) investigated the outflow structure of major Hurricane Ivan, it was done with dropsonde data. Emanuel and Rotunno (2011) suggested the self-stratification of outflow channel, but their study is based on two dimensional idealized TC model. So three dimensional outflow structure of TCs is not examined with high resolution data. Especially, the outflow layer structures and their influences during ET were not studied due to the lack of interests in the past.

3. Can radiative cooling result in dynamic instabilities in the outflow layer?

Papers from Dunion et al. (2014) and Morinali and Vollaro (2014) imply that this diabatic process may affect the instability of the outflow layer, but it has not been validated yet.

4. What is the role of dynamic instabilities of the upper outflow channel in determining the intensity changes of TCs during ET?

Previous ET studies (Klein et al. 2002; Evans and Prater-Mayes 2004) focused on the divergence effect associated with the upper-level jet stream during re-intensification of TCs. However the impact of dynamic instabilities, which are induced by the jet stream, on the outflow channel and intensity changes of TCs during ET is not studied.

Thus, the goal of this study is to investigate (i) the roles of the lower-stratospheric warmth associated with the tropopause undulation and low-level frontogenesis in determining the multiple intensity and structural changes of Hurricane Sandy (2012), (ii) three dimensional structures of the outflow layer during its ET, (iii) the dynamic instabilities within in the outflow layer, and (iv) the impact of dynamic instabilities on the intensity changes of transforming TCs.

1.2 Objectives of this study

Hurricane Sandy (2012) is chosen for the present study because it underwent (i) ET via the interaction with midlatitude baroclinic systems, and (ii) complex structural and intensity changes during its life cycle. Sandy's life was influenced by various upper-level systems such as jet and tropopause undulation, thus this hurricane is a suitable case to study the effect of upper-level processes on the evolution of TCs. In addition, we will pay attention to the importance of low-level ET processes in affecting the intensity and structural changes of the storm.

The objectives of the first part of this study are to (i) document the life cycle of Hurricane Sandy (2012) from its genesis to landfall; and (ii) examine different roles of low-level baroclinic processes, especially those occurring within its vortex circulation, and tropopause undulation in determining the intensity, size and structural changes of the storm. The above objectives will be achieved mostly through a 138-h (0000 UTC 24 – 1800 UTC 29 October 2012) high-resolution, quadruply nested-grid simulation of the case using the Weather Research and Forecast (WRF) model, in addition to synoptic analysis.

When Sandy re-intensified, it interacts with an upper-level jet stream, developing a very large outflow channel. The upper-level jet stream tends to generate dynamic instabilities on its anticyclonic shear side, which can affect the outflow layer structures of the re-intensifying storm. However, Sandy's outflows appear to be generated by both deep convection in the eyewall and in the frontal rainbands in the outer regions. Then, a challenging issue is to separate the outflow of the eyewall convection from that of the frontal rainbands, and investigate their associated dynamics and thermodynamics.

Thus, the objectives of the second part of this study are to (i) develop a new methodology to distinguish multiple outflow layers, (ii) examine the impact of dynamic instability on the outflow channel, (iii) find the link between long-wave radiative cooling and symmetric instability within the outflow layer, and (iv) explore the possible roles of dynamic instability in the re-intensification of Sandy.

My dissertation is organized as follows. The next chapter provides the overview of Hurricane Sandy, experiment settings and model verification. Chapter 3

investigates how low-level moist frontogenesis and lower-stratospheric warm air associated with tropopause undulation determine the structural and intensity changes of Sandy during its entire life cycle. Chapter 4 focuses on the features of an outflow layer and its possible impacts on the re-intensification of Sandy. The final chapter summarizes the results, and provides additional future work.

Chapter 2. The life cycle of Hurricane Sandy

2.1. Previous studies

Hurricane Sandy (2012) was one of the most destructive hurricanes causing more than $50 billion damage and a total of 147 casualties (Blake et al. 2013). It has a record-breaking storm size in the extended best track that began in 1988, with an averaged radius of the tropical-storm-force wind of 660 km at 24 h prior to landfall (Blake et al. 2013). The storm underwent several intensity changes with continuous size expansion as it moved from the southwestern Caribbean Sea to landfall at the New Jersey shoreline.

Although Sandy's track and landfall were well predicted 5 days in advance (Blake et al. 2013; Magnusson et al. 2014), the northwestward movement of this storm was very unusual. Previous studies of Sandy's unusual motion had similar conclusions; the negatively-tilted upper-level trough (the upper-level ridge) on the west (northeast) of Sandy caused the northwestward movement prior to landfall (Barnes et al. 2013; Bassill 2015; Lackmann 2015; Torn et al. 2015). Bassill (2015) used the WRF model with various entrainment coefficients of simplified Arakawa Schubert scheme to test the sensitivity of Sandy's track. From this study, Bassill (2015) concluded that latent heating in the northwestern quadrant of the storm has an influence on the tilted pattern of the upper-level trough which determines the motion of the storm. From the ensemble members of the National Centers for Environmental Prediction (NCEP) Global Forecast System (GFS), Torn et al. (2015) argued that the

divergent outflow associated with Sandy amplified the ridge on the north of the storm through lower potential vorticity (PV) advection.

The intensity change of Sandy has also been studied. Galarneau et al. (2013) utilized the AHW (Advanced Hurricane WRF) model with the finest grid size of 4 km to investigate the re-intensification of the storm. By applying the Sawyer-Eliassen equations to the model simulation, they found that Sandy's re-intensification results primarily from the secondary circulation associated with moist frontogenesis as Sandy's vortex interacts with an approaching large-scale cold front. The frontal convection in the western semicircle region of Sandy generates positive PV, and this PV is advected inward via the inward flow of the storm vortex, leading to the axisymmetrization of the TC vortex. They also suggested that the unusual northwestward motion may cause the re-intensification of Sandy.

It should be mentioned, however, that Galarneau et al. (2013) only studied Sandy's re-intensification during its warm seclusion stage, i.e., after colder air encircles its warm core, and the subsequent landfall using the AHW model that is initialized at 0000 UTC 28 October, i.e., 24 hours prior to landfall. In other words, there is no case study that has investigated the entire life cycle of Sandy, and most of the previous studies focused on the track of this storm. As noted by Blake et al. (2013) Sandy underwent complex intensity and structural changes, but uncertainty remains concerning on the physical processes leading to the multiple intensity changes, and the continued growth of the storm size during its life cycle as well as the timing of its extratropical transition (ET). Furthermore, it still remains unclear about the roles of

two upper-level troughs (i.e., a polar and a subtropical one) and low-level baroclinicity in determining the re-intensification of the storm prior to landfall.

Chapter 2 is organized as follows. Chapter 2.2 provides an overview of the structures and evolution of Sandy based on the National Hurricane Center (NHC) best track data and the National Centers for Environmental Prediction (NCEP) final analysis. Chapters 2.3 and 2.4 describe the model configurations and validation of the numerical simulation, respectively. Chapter 3 shows the non-observable structures and evolution of the storm, and examines the different roles of lower- and upper-level processes in the intensity, structural and size changes of Sandy using the 138-h model simulation. A summary and concluding remark are given in the last part of Chapter 3.

2.2. Overview of Hurricane Sandy

Hurricane Sandy (2012) originated from the Caribbean Sea on 22 October 2012. During the period of 24-26 October, Sandy moved nearly northward over a warm SST region and made the first landfall in the eastern portion of Cuba Islands around 0600 UTC 25 October (Fig. 2.1a). On 27-29 October the storm drifted northeastward slightly, which was 450 km to the east of the Gulf Stream. During this period the underlying SST was about 2~3°C colder than that earlier. Around 0600 UTC 29 October Sandy recurved northwestward and it made landfall along the New Jersey shoreline by 2330 UTC 29 October after moving across the Gulf Stream.

Figure 2.1b shows that at 0000 UTC 24 October, a cold front extended from north-central Canada to central US with a warm front stretched to the east coast, and an east-Canadian high was distributed from Hudson Bay southward to Bahamas. This implies that Sandy would be influenced by *an approaching extratropical baroclinic*

system (Galarneau et al. 2013), and *a zonally distributed baroclinic zone with an easterly flow from the east-Canadian high*, after moving into the midlatitudes. Figure2.2a shows that indeed Sandy, carrying high-equivalent potential temperature (θ_e) air of tropical origin, began to encounter an eastward-propagating upper-level trough with a vast low-θ_e air mass behind the surface cold front, and another low-θ_e air mass in eastern Canada, after moving northward to the east of Florida Peninsula at 0000 UTC 27 October; the leading edges of both air masses can be traced by θ_e = 310K at 900 hPa or z = 1 km. The high (low)-θ_e air was cyclonically advected poleward (equatorward) in the eastern (western) semicircle regions of the storm; such a thermal pattern typically occurs during the ET of TCs (Harr and Elsberry 2000; Klein et al 2000).

A vertical cross section through the upper-level trough and Sandy's core region, given in Fig. 2.2b, depicts a tropopause undulation that is similar to that discussed by Hirschberg and Fritsch (1991a). That is, the tropopause, as defined by 2 PVU (potential vorticity unit; 1 PVU = 10^{-6} K m^2 kg^{-1} s^{-1}), became sharply lower across the two air-mass interface to the northwest, with reversed horizontal potential temperature (θ) gradients in the trough region above 250 hPa. As will be seen in Chapter 3, this relatively warmer air mass in the northwestern lower stratosphere played an important role in determining Sandy's structural and intensity changes at its later stages when it was advected into Sandy's core region and its surrounding areas.

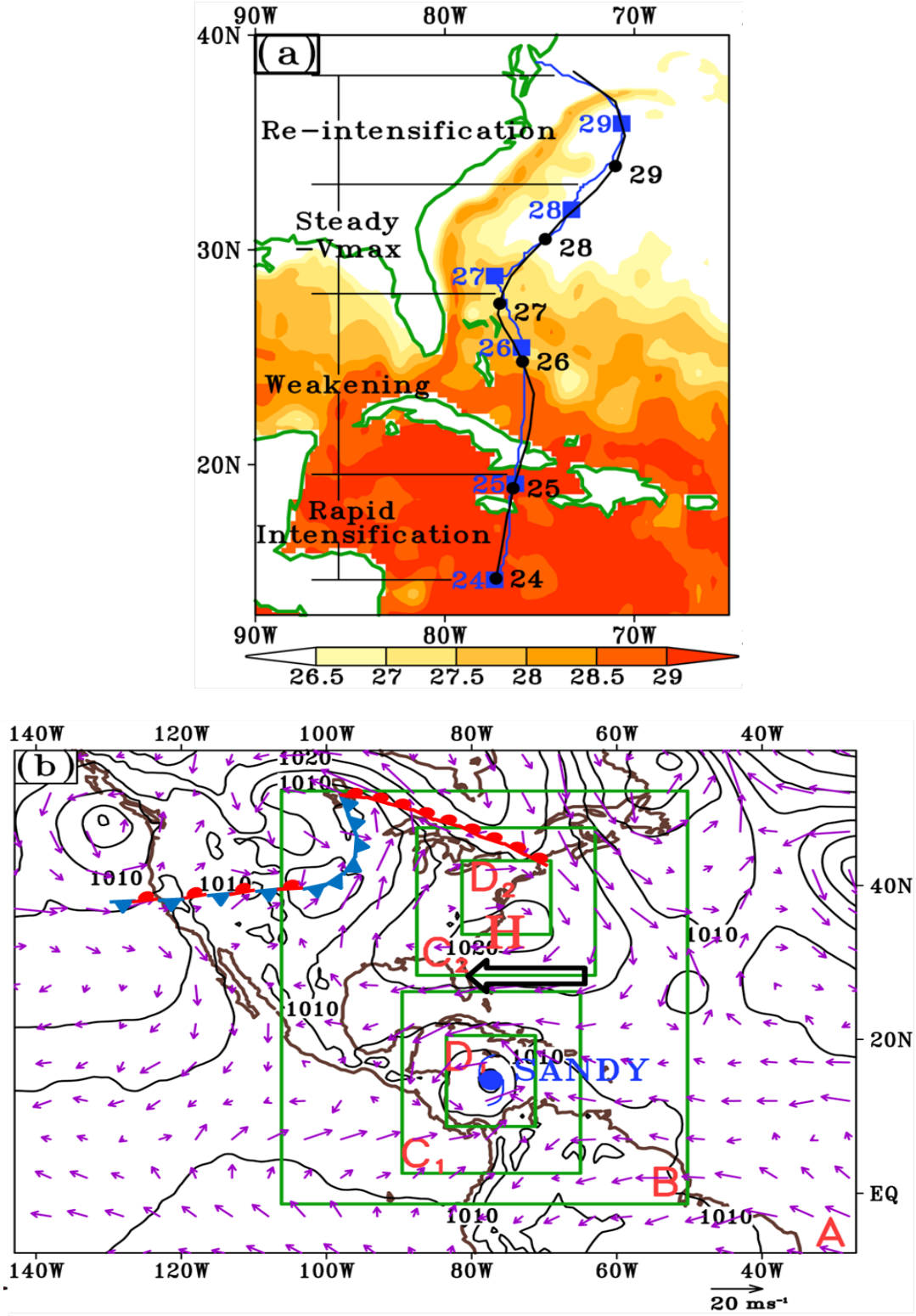

Figure 2.1. (a) Comparison of the simulated track (blue) to the best track (black) of Hurricane Sandy during the period of 0000 UTC 24 to 1800 UTC 29 October 2012, superimposed with the AVHRR-SST (shaded, °C) distribution. Four different stages

of Sandy's life cycle are indicated; similarly for the rest of figures. (b) Model domain configuration, superimposed with SLP (contoured at 5-hPa intervals), 900-hPa wind vectors, and frontal distribution (plotted only over the eastern US region) from the NCEP final analysis at 0000 UTC 24 October 2012. Domains A, B, C and D have 45, 15, 5 and 1.667-km resolutions, respectively. C_1 and D_1 (C_2 and D_2) depict the initial (final) locations of the 5- and 1.667-km resolution domains, respectively. Letter, "H", denotes portion of the east-Canadian high pressure system with an arrow highlighting its associated easterly flow.

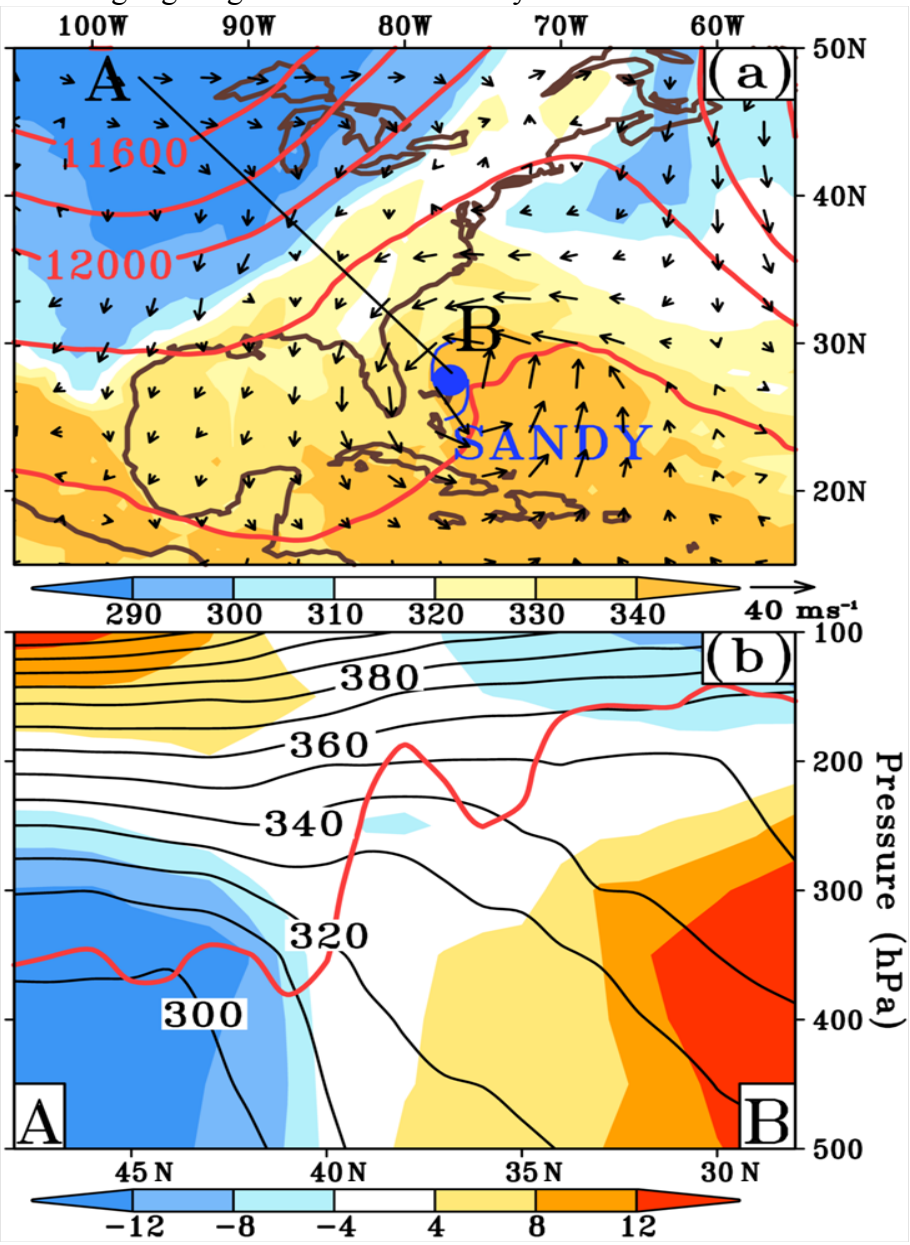

Figure 2.2. (a) The NCEP final analysis of the equivalent potential temperature (θ_e, shaded, K) and horizontal wind vectors at 900 hPa, and the geopotential height (red-contoured at intervals of 200 m) at 200 hPa at 0000 UTC 27 October 2012. A hurricane symbol indicates the location of Sandy; similarly for the rest of figures.

(b) Vertical cross section of potential temperature (black-contoured at 10K intervals), the dynamic tropopause defined by a 2-PVU red line, and temperature deviations (shaded, °C) from the corresponding level-averaged value along line AB given in (a). All fields are ± 110 km laterally averaged on the meridional direction.

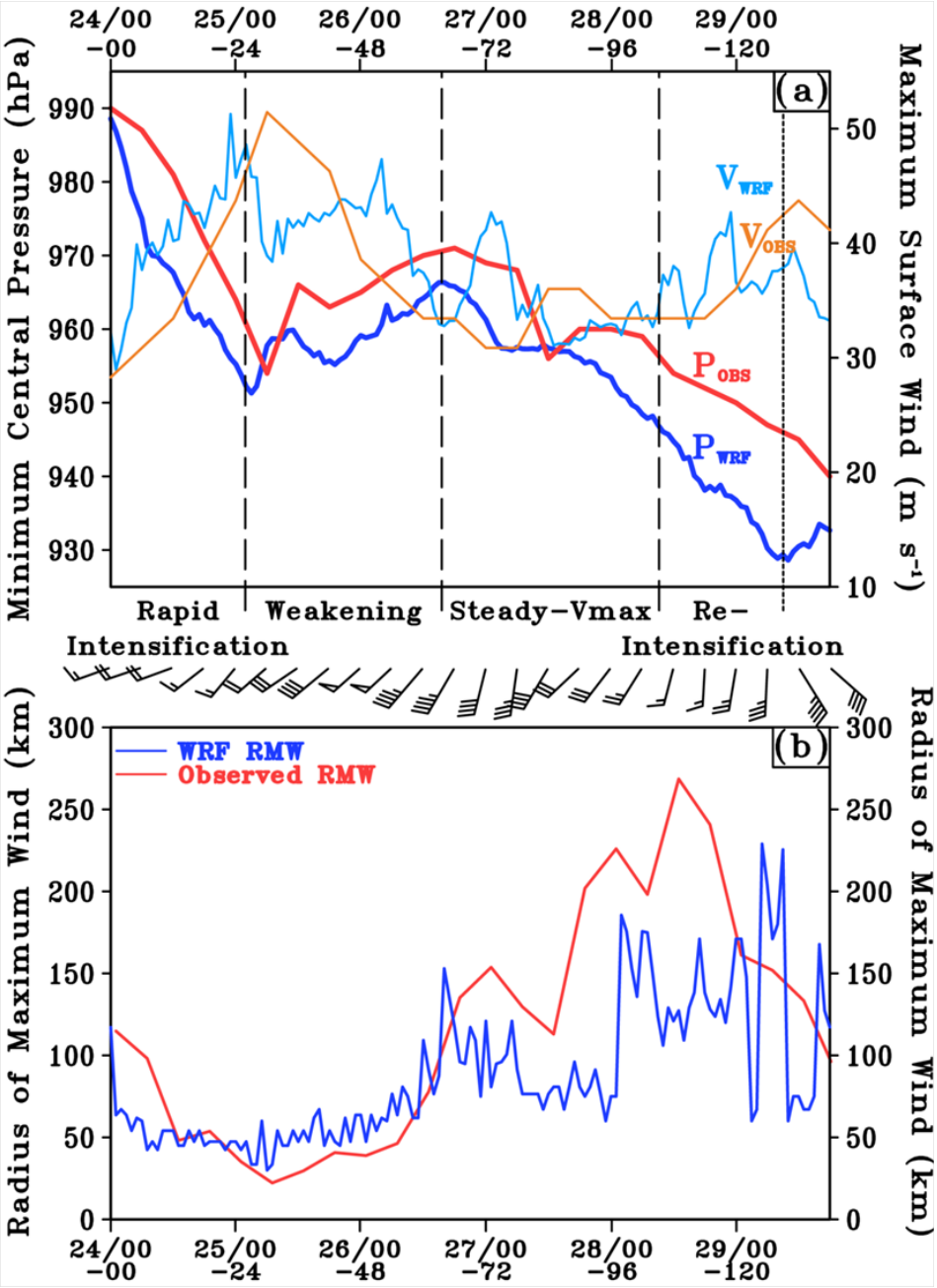

Figure 2.3. (a) Time series of the simulated minimum central pressure (P_{WRF}: thick blue) and maximum surface wind (V_{WRF}: thin blue) and the corresponding best track data (P_{MIN}: thick red; V_{MAX}: thin orange) during the period of 0000 UTC 24 to 1800 UTC 29 October 2012. Note that V_{WRF} is obtained within a 300 km radius

from Sandy's vortex center. Time series of wind barbs (a full barb is 5 m s^{-1}), given at 6-h intervals, represent (1000 km × 1000 km) area-averaged vertical wind shears in the 200-850 hPa layer. Four distinct development stages are defined, based on the model simulation (see text); similarly for the rest of figures. (b) Time series of the simulated (blue) and observed (red) RMW (km).Data from the WRF 15-km resolution domain are used.

Time series of the minimum central SLP (P_{MIN}) and the surface maximum wind (V_{MAX}), given in Fig. 2.3a, shows that Sandy underwent multi-intensity changes during the study period of 0000 UTC 24 – 1800 UTC 29 October 2012. They could be divided into the following four distinct stages: (i) rapid intensification (RI), (ii) weakening, (iii) steady V_{MAX} but with continued falls in P_{MIN}, and (iv) re-intensification. During the RI stage of 0000 UTC 24 - 0600 UTC 25 October, V_{MAX} increased from 28 to51 m s^{-1} (i.e., category-3 intensity) with a 24-h intensifying rate greater than the RI rate defined by Kaplan and DeMaria (2003), while P_{MIN} decreased from 990 to 954 hPa. Sandy weakened rapidly to category-1 intensity (i.e., 33 m s^{-1}) after making landfall at Cuba near 0600 UTC 25 October, and its weakening continued, albeit at a reduced rate, even after it moved across the Cuba island into a warm SST region. V_{MAX} remained nearly constant, e.g., varying between 30 and 35 m s^{-1}, so called the steady-V_{MAX} stage, during the 48-h period of 1800 UTC26 – 1800 UTC 28 October. Of interest is that *while V_{MAX} changed little in amplitude, P_{MIN} kept dropping for a total of 19 hPa in 48 h in spite of Sandy's moving over a colder SST region* (cf. Figs. 2.1a and 2.3a). Thus, as one of the objectives of this study, we must address what process could account for such an unusual phenomenon, namely, continuous drops in P_{MIN} but with little changes in V_{MAX}. The storm re-intensified during the period of 1800 UTC 28-1800 UTC 29 October, with V_{MAX} reaching to a

secondary peak value of 43 m s^{-1} (i.e., category-2 intensity) just prior to landfall. To understand these unusual intensity changes of the storm, especially its associated structural and size changes, we have to invoke high-resolution simulations of the case, as described below.

2.3. Model description

In this study, Hurricane Sandy is explicitly simulated using a two-way interactive, quadruply nested grid (45/15/5/1.667 km) Version 3.4.1 of the WRF model with the finest grid size of 1.667 km (Skamarock et al. 2008). Horizontal (x, y) dimensions for the nested 45/15/5/1.667 km domains are 250 × 170, 361 × 406, 475 × 475, and 709× 709, respectively (Fig. 2.1b). The 5- and 1.667-km resolution domains are storm-following nests, with the storm centered in them. In the vertical, 44 sigma levels are used with higher resolution at the bottom and upper levels. They are 1.0000, 0.9974, 0.9927, 0.9857, 0.9767, 0.9657, 0.9527, 0.9372, 0.9195, 0.8995, 0.8770, 0.8526, 0.8256, 0.7969, 0.7664, 0.7343, 0.7007, 0.6655, 0.6293, 0.5925, 0.5555, 0.5185, 0.4815, 0.4445, 0.4075, 0.3707, 0.3345, 0.2993, 0.2657, 0.2336, 0.2031, 0.1744, 0.1474, 0.1230, 0.1005, 0.0805, 0.0628, 0.0473, 0.0343, 0.0233, 0.0143, 0.0073, 0.0026, and 0.0000. The model top is set at 30 hPa. All domains are initialized at 0000 UTC 24 October, which is just prior to the onset of RI, and integrated 138 h until 1800 UTC 29 October, i.e., shortly after Sandy reached its second intensity peak.

An advanced bogussing algorithm developed by Kwon and Cheong (2010) is applied. To follow their bogussing algorithm, the NCEP 1°-resolution final analysis is interpolated into 0.175°-resolution data, and then used to specify the model initial and

outermost lateral boundary conditions. A bogus vortex is implanted into the interpolated NCEP analysis at the model initial time, based on the NHC's best track data (i.e., P_{MIN}, location, V_{MAX} and 17 m s^{-1} wind radius). SSTs are specified from the 0.25°-resolution Advanced Very High Resolution Radiometer (AVHRR) SST data at the model initial time, and they remain constant during the 138-h simulation period. This high-resolution SST dataset appears to be important for obtaining realistic simulations because it resolves the narrow Gulf Stream (Fig. 2.1a).

The model physics schemes used include: (i) the Kain-Fritsch cumulus parameterization scheme (Kain 2004) for the three outer domains; (ii) the WSM5 single-moment 5-class microphysics scheme (Hong et al. 2004; Hong and Lim 2006) for all the domains; (iii) the Yonsei University planetary boundary layer (PBL) parameterization with the Monin-Obukhov surface layer scheme (Hong et al. 2006); (iv) a modified surface flux scheme for high surface winds (Donelan et al. 2004; Davis et al. 2008); and (v) the Rapid Radiative Transfer Model (RRTM) scheme for longwaves (Mlawer et al. 1997) and Dudiha (1989) short-wave radiation scheme.

2.4. Model verification

Before the model simulation can be used to analyze Sandy's meso-β-scale structures and evolution, it is necessary to verify it against all available observations. It is apparent from Fig. 2.1a that the WRF reproduces remarkably well the best track during the 138-h integration period, including Sandy's curved movements and relative position to the Gulf Stream. However, the simulated storm begins to move poleward notably faster than the observed after 24 h into the integration, i.e., from

0000 UTC 25 October, hereafter referred to as 25/00-24. The simulated 5-day track error at 29/00-120 is 220 km, which is smaller than the official 5-day forecast error of 275 km (Blake et al. 2013). Because of the faster movement, the simulated storm begins its northwestward recurvature about 6 h earlier than the observed around 29/06-126. As a result, the simulated Sandy moves across the Gulf Stream and reaches its second peak intensity slightly earlier than the observed.

The time series of P_{MIN} and V_{MAX} between the best track and WRF simulation is compared in Fig. 2.3, showing that despite some differences in details due partly to different spatial and temporal resolutions between the WRF simulation and best track, the model reproduces reasonably well the above-mentioned four distinct stages: RI, weakening, steady-V_{MAX}, and re-intensification. Because of the slight-faster poleward movements, the simulated storm reaches its first peak intensity in P_{MIN} and V_{MAX} of 952 hPa and 49 m s^{-1}, respectively, around 25/02-26, which occurs just prior to landfall on Cube Island, about 4 h earlier than the observations. Then, it decays to its weakest intensity of 966 hPa and 33 m s^{-1} around 26/16-64, and re-intensifies to its second peak intensity of 929 hPa and 38 m s^{-1} shortly after passing cross the Gulf Stream at 29/10-130 (cf. Figs. 2.1a and 2.3).

The model simulates on average the intensifying rate of about 34 hPa day^{-1} in P_{MIN} and more than 16 m s^{-1} day^{-1} in V_{MAX} during the RI stage (i.e., from 24/00-00 to 25/02-26), and the weakening rate of about 9 hPa day^{-1} in P_{MIN} and 10 m $s^{-1}day^{-1}$ in V_{MAX} during the weakening stage (i.e., from 25/02-26 to 26/16-64), the fluctuating V_{MAX} around 35 m s^{-1} but the continued deepening rate of 11 hPa day^{-1} during the steady-V_{MAX} stage (i.e., from 26/16-64 to 28/10-106), and the intensifying rate of 17

hPa day^{-1} in P_{MIN} and about 3 m s^{-1} day^{-1} in V_{MAX} during the re-intensification stage (i.e., from 28/10-106 to 29/10-130). The four stages coincide with the periods of moderate VWS (i.e., varying between 11 to 7 m s^{-1} in the 200-850 hPa layer), increasing VWS (i.e., from 7 to 26 m s^{-1}), intense VWS but with decreasing magnitudes at the later period (i.e., from 26 to 9 m s^{-1}), and increasing VWS once again (i.e., from 9 to 21 m s^{-1}), respectively (Fig. 2.3a). The two periods of increasing VWS correspond to Sandy's approaching to a jet stream ahead of two upper-level troughs, respectively. It is encouraging that the model reproduces well the magnitude of V_{MAX} ~35 m s^{-1}and the observed mean deepening rate in P_{MIN} during the steady-V_{MAX} stage.

A comparison of the simulated RMW to that in the H*wind data (Powell et al. 1998) also shows that the model captures the initial rapid contraction to 50 km and the subsequent near-constant RMW during RI, and the later expansion of the RMW to about 150 km (Fig. 2.3b). The simulated RMW exhibits pronounced fluctuations, i.e., between 60 and 200 km, after 28/00-96 because of the development of another RMW associated with an intense spiral band in the outer regions, as will be shown in chapter 3.1. The smaller RMW associated with the eyewall decreases from about 110 to 60 km during the re-intensification stage, which is consistent with the contraction of Sandy's vortex in the H*wind data.

To show further the quality of the model simulation, Fig. 2.4 compares the simulated cloud structures to the observed outgoing long-wave radiation (OLR) at cloud top. Sandy exhibits a typical mature TC's structures shortly after reaching its first peak intensity from both the simulation and satellite infrared image (IR) (cf.

Figs. 2.4a and 2.4e), with a clear eye inside a full eyewall and two spiral rainbands (an inner one spiraling from the northwestern to southeastern and then southwestern quadrant and an outer rainband extending from the northwestern to northeastern quadrant). The weakening stage corresponds to reduced convective activity in the eyewall, scattered clouds in the inner and outer rainbands (Figs. 2.4b and 2.4f). The steady-V_{MAX} stage is characterized by an eyewall that is somewhat separated from an

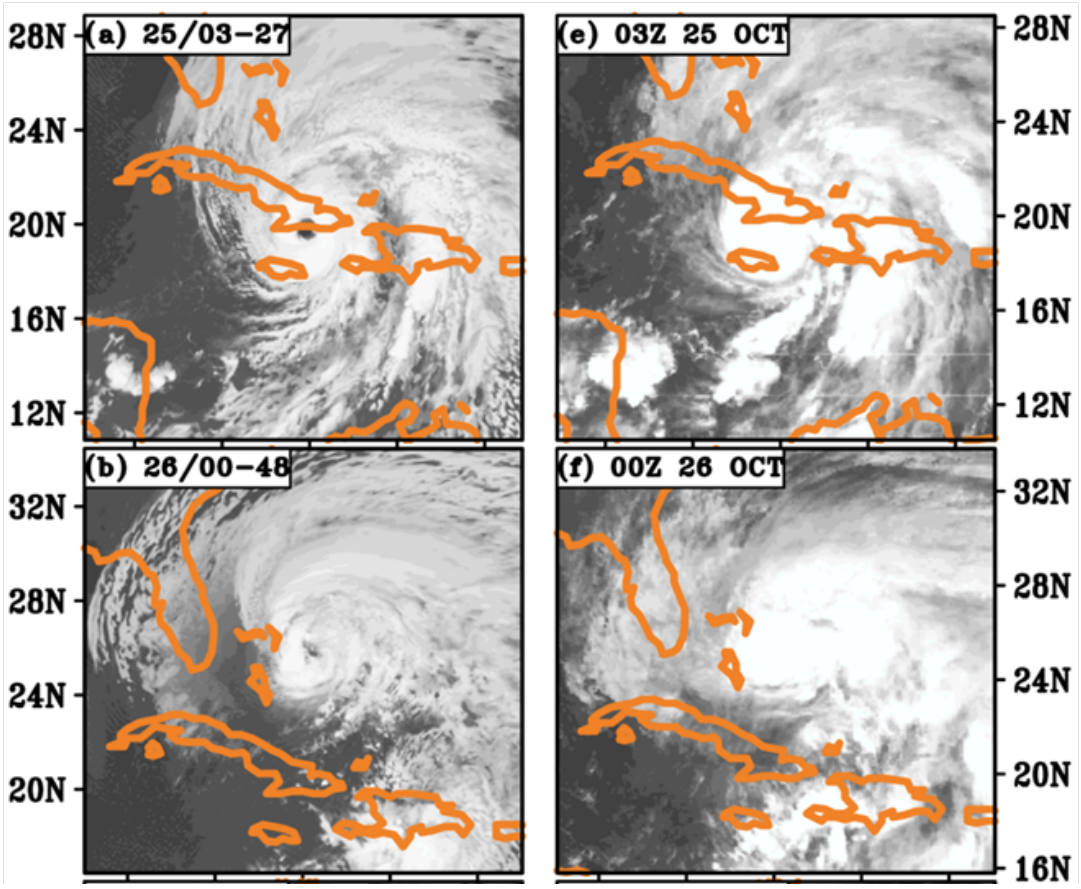

Figure 2.4. (a)-(d) The simulated outgoing long-wave radiation (OLR, shaded, W m^{-2}) from the 5-km resolution domain at25/03-27, 26/00-48, 27/15-87, and 29/03-123, respectively. (e)-(h) As in (a)-(d), but for the satellite IR images at the given time from the Gridded Satellite (GridSat-B1) data archive of National Climatic Data Center of NOAA (http://www.ncdc.noaa.gov).

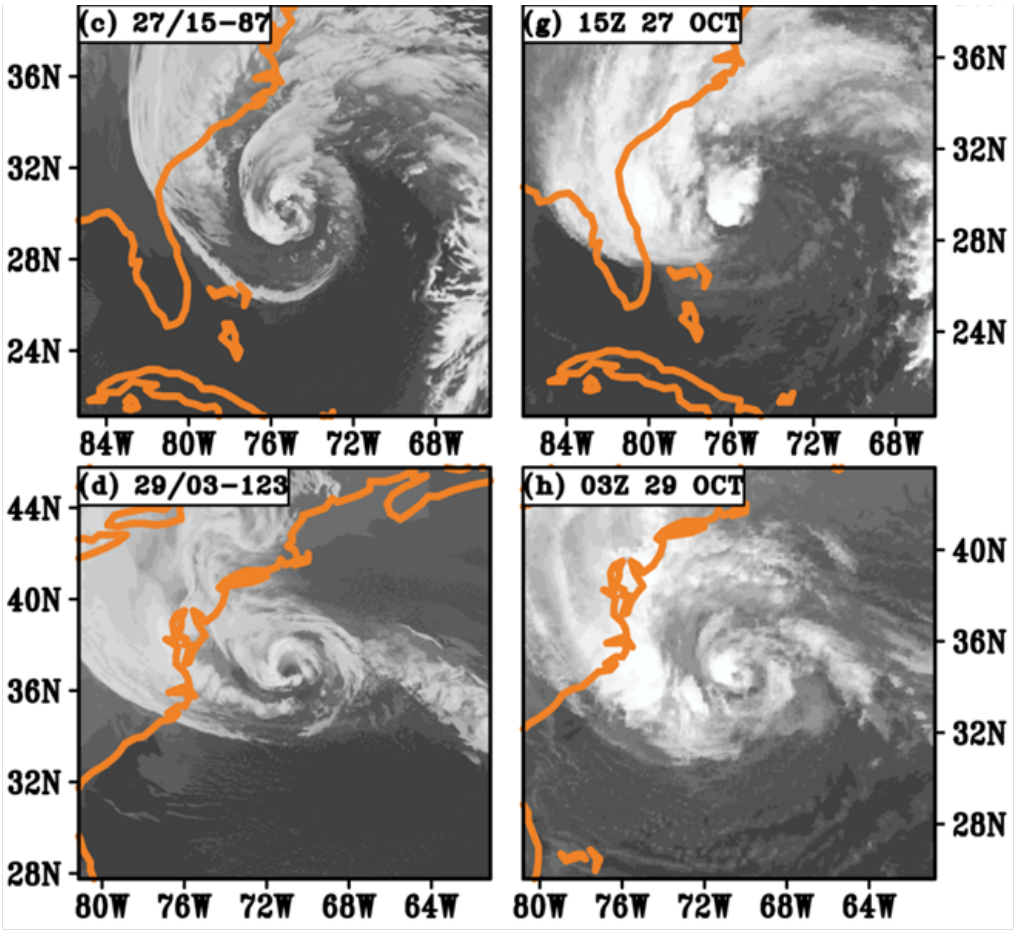

Figure 2.4. (Continued)

extensive, wide outflow channel associated with the outer rainband as it moves cyclonically to the western semicircle (cf. Figs. 2.4c and 2.4g). At the final stage, this outflow channel extends from the southern semicircle to eastern Canada with a much smaller sized eyewall (Fig. 2.4h). The WRF captures well these structures and their changes, especially the break-up of the spiral rainband in the southeastern quadrant (Figs. 2.4d,h), except for cloud activity in the inner-core region during the final two stages (cf. Figs. 2.4c,g and 2.4d,h).

Based on the above verifications, we may state that the WRF simulates reasonably well the life cycle of Hurricane Sandy (2012) in terms of track and

intensity changes, even though later stages begin somewhat earlier than the observations. The WRF also reproduces well the structural and size evolution of the storm, including the RMW and cloud coverage. Thus, the model simulation could be used in the next to address the objectives of the present study and examine some non-observable features of the storm. Because of the timing errors in track, the four distinct development stages will be based on the model-simulated wind intensity for the sake of subsequent discussions.

Chapter 3. The impact of the lower-stratospheric warming and low-level frontogenesis

In this chapter, we present the evolution of Sandy's intensity, size and structural changes and then examine the relative contributions of low- and upper-level processes to these changes using the model-simulation data.

3.1. General structural evolution and warm frontogenesis

Figure 3.1 shows the horizontal structural evolution of Sandy during its four different stages. At the first peak intensity near 25/02-26, we see typical cloud structures (Figs. 2.4a and 3.1a) and wind-pressure fields (Fig. 3.1h) associated with a mature TC: a well-defined eye, and a relatively compact and symmetric eyewall with an RMW of about 50 km, several spiral rainbands distributed mostly in the northeastern outer semicircle; and dense (very coarse) isobars in the inner-core (outer) regions. In addition, Sandy is surrounded by higher (lower) than 345K-θ_e air of tropical (polar) origin in the southern (northern) environment. As VWS increases and Sandy weakens, the more symmetric rainfall distribution in the eyewall evolves gradually to a wavenumber-1 structure, with intense precipitation occurring on the downshear-left side, i.e., in the northwestern quadrant (cf. Figs. 2.4a,b and 3.1a,b). Similarly, the TC circulation becomes elliptically shaped, with its low-SLP center close to more active convection to the northwest. Meanwhile, Sandy's northward movement over cooler water toward the northern baroclinic zone associated with the east-Canadian high tends to decrease θ_e in the PBL and increase meridional θ_e

gradients, as indicated by the approaching lower than 330K-θ_e air in the north (Fig. 3.1b). In particular, Sandy's south- to southeasterly high-θ_e current converges with this easterly lower-θ_e current in the northeastern quadrant (e.g., along the θ_e=345K contour), leading to the formation of a warm-frontogenetic zone (labeled as "A" in Fig. 3.1i) with increased θ_e-gradients, along which a robust spiral rainband is developed (Figs. 3.1b,i). This type of frontogenesis is a typical feature of ET (Klein et al. 2000; Jones et al. 2003; Colle 2003). Frontogenesis in the present study is defined by a scalar frontogenesis function (in blue in Figs. 3.1h-n) associated with divergence and horizontal deformation on horizontal θ gradients, following Keyser et al. (1988), and it is given by Equation (3.1).

$$F_n = -\frac{1}{|\nabla\theta|}\left[\frac{\partial\theta}{\partial x}\left(-\frac{\partial u}{\partial x}\frac{\partial\theta}{\partial x}-\frac{\partial v}{\partial x}\frac{\partial\theta}{\partial y}\right)+\frac{\partial\theta}{\partial y}\left(-\frac{\partial u}{\partial y}\frac{\partial\theta}{\partial x}-\frac{\partial v}{\partial y}\frac{\partial\theta}{\partial y}\right)\right] \quad (3.1)$$

where the first and second term represents divergence and deformation (i.e., confluence) effect on frontogenesis, respectively.

Clearly, deep convection would enhance the mass and moisture convergence, facilitating the generation of wind streaks and SLP falls through cyclonically inward advection of the absolute angular momentum (AAM), as discussed by Yau et al. (2004). It would also augment the frontogenetic forcing, assisting further convective organization. In fact, a swirling jet of exceeding 30 m s^{-1} begins to develop along the outer frontogenetic zone (Fig. 3.1i).

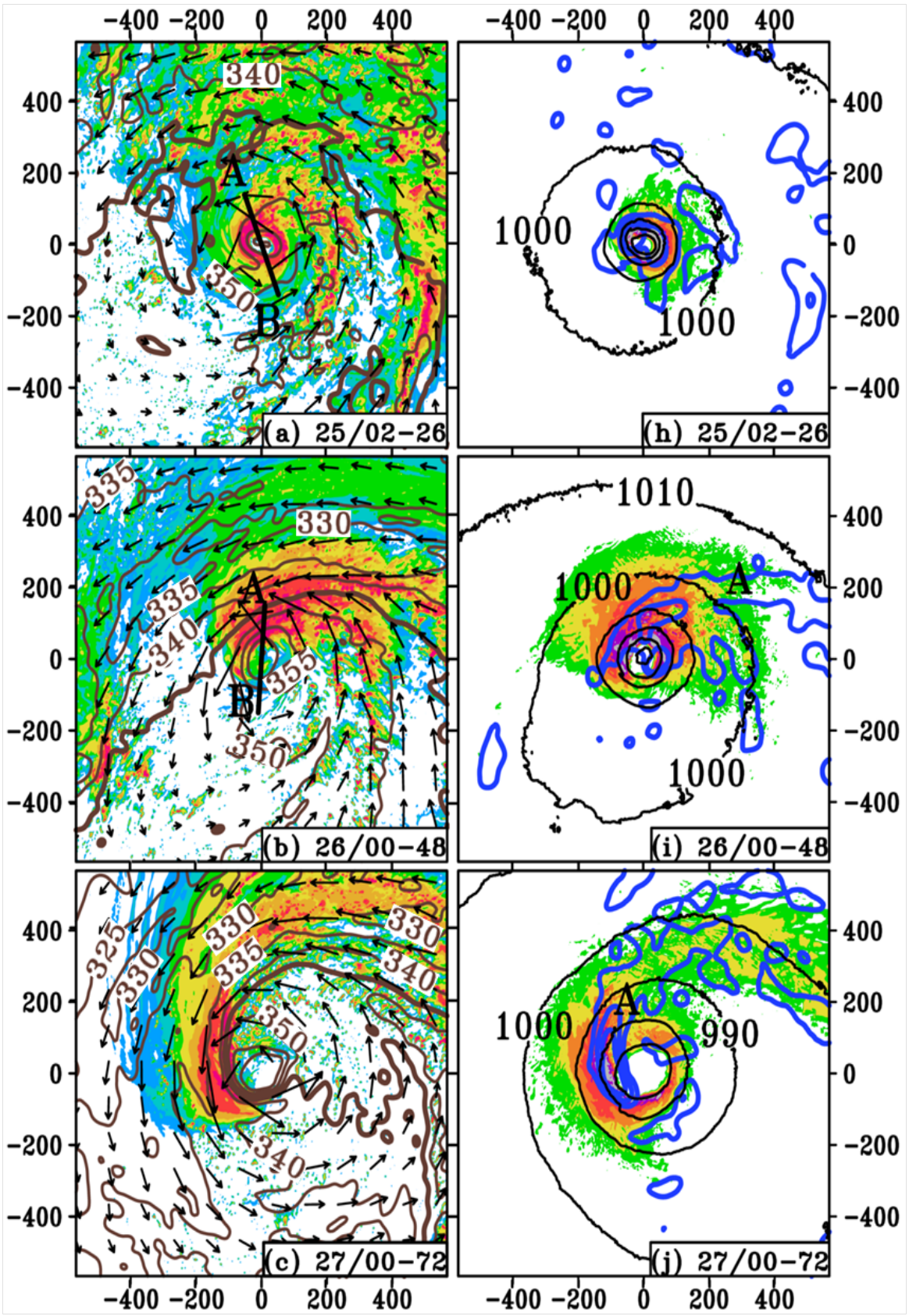
(a) 25/02-26
(h) 25/02-26
(b) 26/00-48
(i) 26/00-48
(c) 27/00-72
(j) 27/00-72
A
B
340
350
330
335
355
325
1000
1010
990

Figure 3.1. (a) – (g) Horizontal distribution of composite radar reflectivity (shaded, dBZ), equivalent potential temperature (θ_e, contoured at 5K intervals with θ_e= 310 and 345K highlighted in brown) and horizontal wind vectors at z = 1 km from the WRF 1.667-km resolution (567 km × 567 km) subdomain, valid at 25/02-26, 26/00-48, 27/00-72, 28/00-96, 28/18-114, 29/03-123, and 29/09-129, respectively. Line AB denotes the locations of vertical cross sections shown in Fig. 3.8. (h) – (n) As in (a) – (g) but for horizontal distribution of SLP (black-contoured at 10-hPa intervals), horizontal wind speeds (shaded, m s^{-1}), and two-dimensional scalar frontogenesis function [blue-contoured at 4, 20 and 40K (100 km)$^{-1}$ h^{-1}] that is multiplied by -1 at z = 1 km. Letters, "A", "B", "C", "D", and "E", shown in (i) – (n), denote various frontal rainbands (see text).Horizontal and vertical axes indicate the distance (km) from Sandy's vortex center.

Because of the asymmetric locations of the eyewall convection relative to the low SLP center, Sandy's movement exhibits trochoidal oscillations as shown by Newman and Boyd (1962), and Liu et al. (1999), with the associated vortex core being advected within a larger-scale elliptically-shaped circulation (Figs. 3.1b,c). By 27/00-72, we see a comma-shaped swirling jet varying from over 55 m s^{-1} in the eyewall to 35 m s^{-1} at R = 500 km, which corresponds to the distribution of the eyewall convection and spiral frontal rainband (Figs. 3.1c,j).

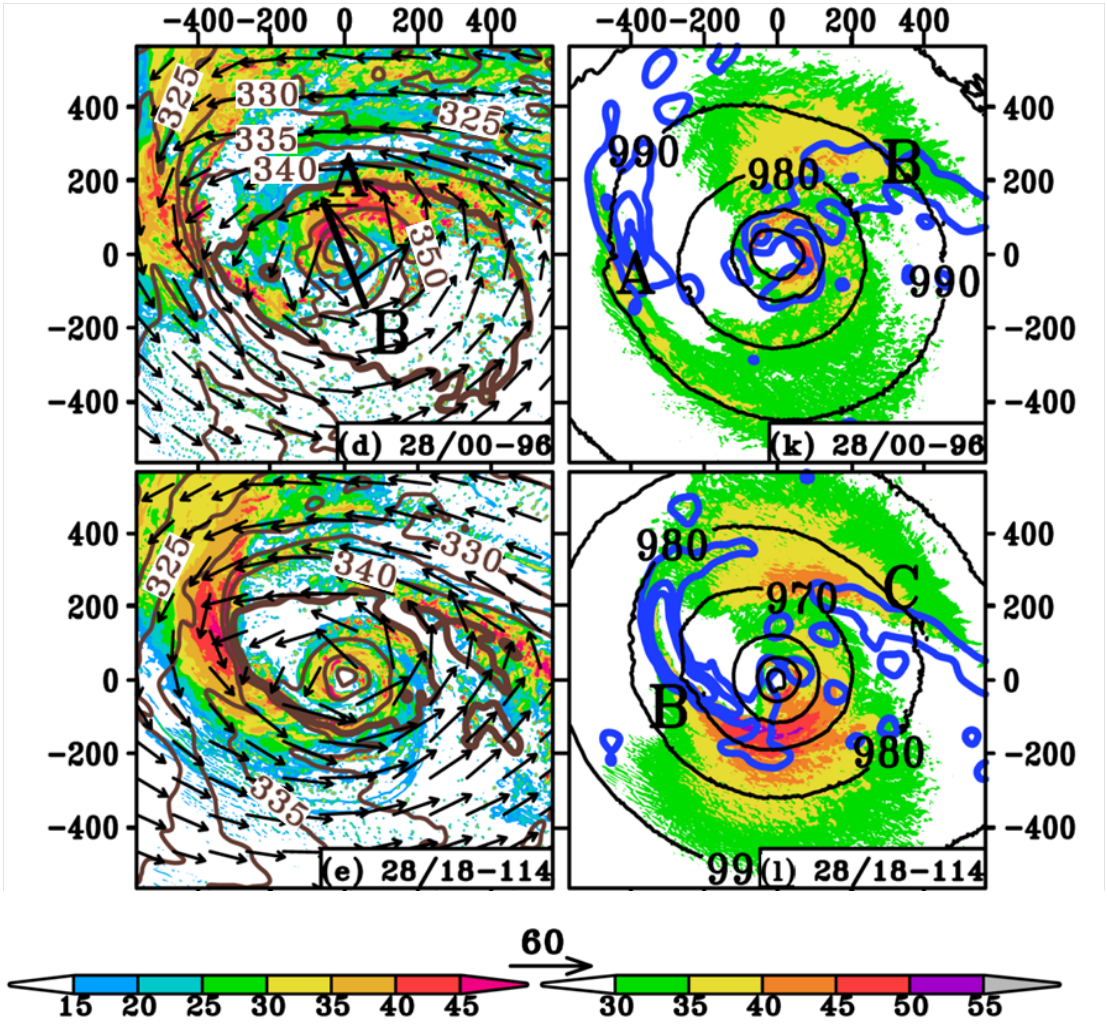

Figure 3.1.(Continued)

At 28/00-96, the cyclonic advection of the vortex core within the elliptically shaped circulation, plus easterly flows outside 200-km radius associated with the east-Canadian high (cf. Figs. 3.1d and 2.1b), almost decouples the eyewall convection from the frontal rainband, as the latter is fast-advected to the northwest (cf. Figs. 3.1c and 3.1d). Of interest is the development of another frontogenetic zone (labeled as "B" in Fig. 3.1k) with a spiral rainband in the northeastern quadrant, which occurs again due to the confluence and convergence between Sandy's southeasterly flow and

the easterly flow (Figs. 3.1d,k). For the same reason, a third frontogenetic zone/rainband, labeled as "C" in Fig. 3.1l, develops in Sandy's northeastern quadrant by 28/18-114. In contrast, little cloud activity occurs in the southeastern semicircle where upward motion is suppressed in the inner-core region by intense southwesterly to southerly VWS, and in the outer region due to the presence of diffluence (i.e., frontolysis). As a result, Sandy exhibits three convective bands: one in the partial eyewall, and the others along the two warm fronts; but two major wind streaks corresponding to the two frontal bands, and a minor one coinciding with the eyewall convection (Figs. 3.1d,k). It is the amplitude changes of the wind streaks that account for the fluctuation of the RMW in Fig. 2.3b. Note the absence of wind streaks along the western rainband at 28/00-96, even in the presence of strong frontogenetic forcing. This can be understood as a result of the radially outward advection of AAM by the intense easterly flow (Figs. 3.1d,k).

Sandy's re-intensification stage is dominated by (i) a well-developed wavenumber-1 precipitation pattern on the downshear left, as southerly VWS increases to about 20 m s^{-1} (Figs. 3.1f,g and 2.3a); (ii) the generation of a localized wind streak associated with the partial eyewall in the northern semicircle (Figs. 3.1f,m);(iii) merging of the final two frontogenetic zones/rainbands and partial eyewall into a spiral intensifying frontogenetic zone/rainband "D" extending from the southwestern partial eyewall to outer northeastern quadrant (Figs. 3.1m,n), as the frontal rainband "A" diminishes shortly after 28/00-96; and (iv) an inward-spiraling jet of greater than 55 m s^{-1} along the merged frontogenetic zone and eyewall (Fig. 3.1n). Note that the vortex contraction, as shown in Fig. 2.3b, may be considered as

the cyclonic inward contraction of the jet core, representing Sandy's intensity, along the intensifying frontogenetic zone, where the cyclonic inward advection of AAM is further enhanced. Note also the substantial reduction of the higher than θ_e = 345K coverage after 28/00-96, due partly to Sandy's movement over cooler water and partly to the evaporation of precipitation falling through low-θ_e layers above, indicating the importance of baroclinic processes in determining Sandy's re-intensification. It should be mentioned that Galarneau et al. (2013) have also simulated the development of a warm-frontal rainband, which is anchored to the Gulf Stream, in Sandy's northwestern quadrant during this stage.

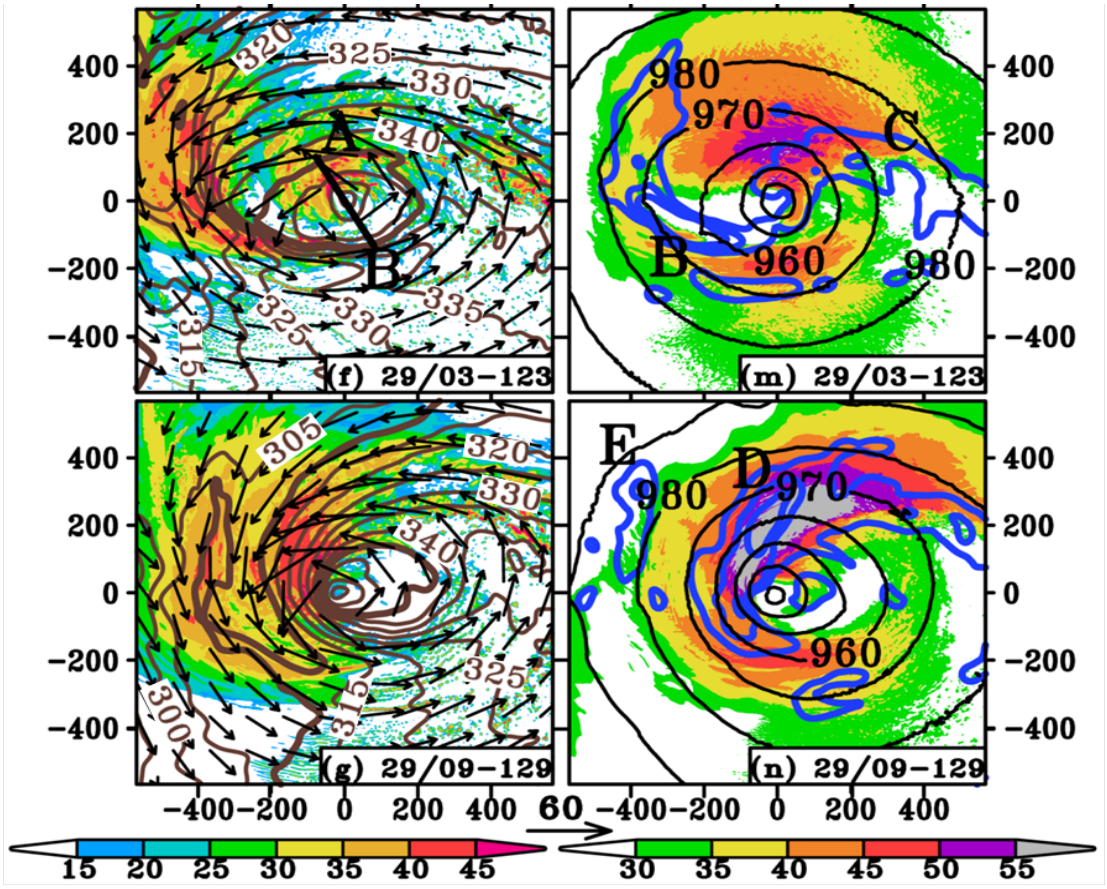

Figure 3.1. (Continued)

Apparently, *it is (i) convectively enhanced (warm) frontogenesis resulting from interaction of the high-θ_e southeasterly flow with the low-θ_e easterly flow(i.e., moist frontogenesis) within Sandy's internal circulation that leads to the generation and continued size expansion of the tropical-storm-force wind, and (ii) partial eyewall convection invigoration, the merging of two frontogenetic zones/rainbands and this eyewall convection, and the subsequent cyclonic inward progression of the jet core along the enhanced frontal rainband that account mostly for Sandy's re-intensification.* In fact, the cold front, traced by θ_e = 310K at z = 1 km (Figs. 2.2a and 2.1b), just enters the western boundary of the analysis domain at 29/03-123 (Fig. 3.1f), and it generates an elongated narrow rainband along a frontogenetic zone, labeled as "E" in Fig. 3.1n, near R =400 km when converging with the east-Canadian air of the same coldness (as shown by a cyclonically oriented θ_e = 310K tongue) at 29/09-129 (Fig. 3.1g). There is no doubt that this cold front could influence the storm's intensity and structures after its landfall (Galarneau et al. 2013). Note that lower than 310K-θ_e air of polar origin has not encircled the warm-cored storm at 29/09-129, unlike the warm seclusion shown by Galarneau et al. (2013), and it should remain so as long as the warm frontogenesis continues.

Figs. 3.1i-m also show continuous meso-α scale SLP falls after 26/00-48, including P_{MIN} (Fig. 2.3), while V_{MAX} remains nearly a steady state. For example, the radius of the 980-hPa isobar expands from 80 km at 26/00-48 to 200 km at 28/00-96, and over 400 km at 29/03-123. The isobar keeps expanding eastward subsequently, while its western semicircle shrinks in radius in the presence of deep convection, thereby increasing local radial pressure gradient force (PGF_R) and rotational winds

(cf. Figs. 3.1g,n). One may ask: Why could the lower SLP coverage and the associated cyclonic circulation expand dramatically while V_{MAX} experiences little changes in amplitude? Is this expansion attributable to the outer spiral/frontal rainband? In this regard, Wang (2009) shows, using an axisymmetric TC-like model, that an outer spiral rainband tends to cause SLP falls on its inward side where the inertial stability is relatively high, increasing the coverage of SLP falls. Similar results have been shown by Hill and Lackmann (2009) in the context of convectively generated PV along spiral rainbands. This indicates that diabatic heating in the outer region would likely reduce PGF_R, thereby decreasing V_{MAX}. However, unlike in Wang's experiment, Sandy has highly asymmetric spiral rainband structures, and pronounced SLP falls occur on both inward and outward sides, especially in the outer southeastern quadrant where little convective activity takes place. Thus, diabatic heating along the outer spiral rainband cannot explain the rapid expansion of the SLP falling area. As will be shown in the next subsection, the meso-α scale SLP falls are associated mainly with the advection of warmer air in the lower stratosphere from the northwest. More pronounced SLP falls occur in both the inner-core and outer regions after entering the re-intensifying stage, which are qualitatively consistent with the contraction of Sandy's vortex and increasing rotational flows in both the eyewall and spiral rainband. Only near the western boundary of the analysis domain at 29/09-129, SLP exhibits a sign of slow rising as a result of the approaching cold front (cf. Figs. 3.1m and 3.1n).

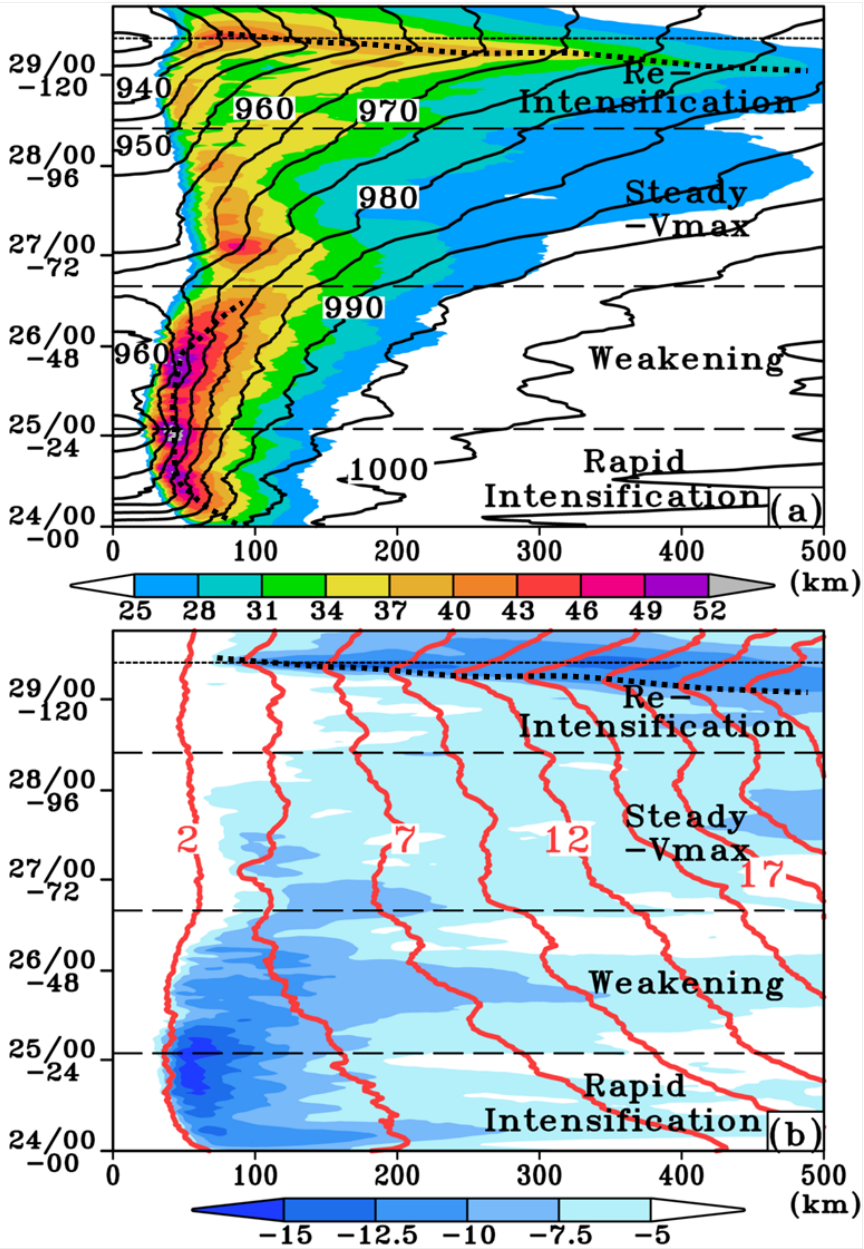

Figure 3.2. Time-radius cross section of the azimuthally averaged fields: (a) tangential wind speeds (shaded, m s^{-1}) at z = 0.5 km and SLP (contoured at 5-hPa intervals), and (b) radial wind speeds (shaded, m s^{-1}) and AAM (red-contoured at intervals of 2.5 × 10^6 m^2 s^{-1}) at z = 0.5 km from the 138-h simulation of the WRF 1.667-km resolution domain. Dotted lines in (a) and (b) denote the RMW, and the ridge axis of AAM, respectively (see text).

The time series of azimuthally averaged fields, given in Fig. 3.2a, summarizes Sandy's intensity and size changes during the four different stages. One can see

intensifying swirling winds accompanied by rapid central SLP falls with time, with strong radial SLP gradients in the inner-core region, and a rapidly reducing RMW (in the first 6-12 h) followed by a near-constant RMW during the RI stage; slowly weakening flows and SLP gradients with an increasing RMW, and slow central SLP filling during the weakening stage; slowly evolving swirling winds despite significant contraction, and the later formation of spiral rainbands, but pronounced central SLP falls during the steady-V_{MAX} stage; and a decreasing RMW, increasing winds and SLP falls during the final stage. Of significance is the expansion of intense swirling flows (e.g., greater than 25 m s^{-1}) and storm-scale SLP drops (e.g., encompassed by the 990-hPa isobar) from R = 120 km at 25/12-36 to R = 500 km at the end of the steady-V_{MAX} stage, and even larger at the later stages, making Sandy a record-breaking storm size. Note again that the SLP field keeps dropping in both the outer and inner-core regions during the steady-V_{MAX} stage, as also shown in Figs. 3.1i-l, and at a similar rate, as indicated by near-linear distribution of isobars out to R = 500 km.

An analysis of the azimuthally averaged AAM and radial flows in Fig. 3.2b indicates two pronounced radial flow regions: one within R = 200 km during the early two stages and the other in R = 80 - 500 km at the final stage, with a broad range of weaker inflows during the intermediate stages. The above-mentioned storm size growth results from continuous inward advection of AAM by *meso-α-scale* convergence associated with *a broader range of SLP falls*, except for the core region where little radial inflows and AAM advection are present. A comparison of Figs. 3.2b and 3.2a indicates that the azimuthally averaged peak rotational wind in the PBL

increases rapidly during the first 12-h RI stage because of the significant inward AAM advection and RMW contraction, maintains its strong intensity with a near-constant RMW until 26/00-48, and decreases later owing to the expansion of the RMW associated with the weakening eyewall convection but enhanced spiral rainband. The steady-V_{MAX} stage is characterized with much weaker (significant) inward AAM advection within (outside) R = 150 km. While the outer frontal rainband enhances cyclonic winds in the outer region via the inward AAM advection, the widespread SLP falls tend to suppress increases in PGF_R, thereby inhibiting the increase of the inward AAM advection to the core region. This appears to explain why the rotational speed of Sandy changes little during the steady-V_{MAX} stage. As a result, Sandy exhibits a weak but broad cyclonic circulation structure during this stage (Fig. 3.2a). On the other hand, we see increasing PGF_R and radial inflows at the re-intensification stage, allowing for more significant inward advection of AAM and spin up of tangential winds starting from the outer regions inward, namely, from R = 500 km at 29/00-120 to R = 100 km at 29/10-130 [see dotted lines denoting the ridge (trough) axes of AAM and V_{MAX} (SLP) in Figs. 3.2a, b].

3.2. Relationship between SLP falls and tropospheric-stratospheric warming

Because SLP falls are hydrostatically associated with temperature changes in vertical columns, Fig. 3.3a shows the height-time cross section of (10 km × 10 km) area-averaged temperature changes [i.e., $\Delta T(z,t)$] with respect to a vertical profile of the same area-averaged temperature at the initial time T(z,t=0 h), which could be considered as "warming tendencies," while Fig. 3.3b shows the time series of the calculated P_{MIN} associated with two distinct layers of warming tendencies during the

final two stages: one in the (low- to midtroposphere) z = 2-7 km layer of 2-8°C and the other in the layers above z = 12 km of up to 12°C, with little or negative warming tendencies in the intermediate layers. Zhang and Chen (2012) have demonstrated the more efficient roles of the upper-level warming than a lower-level one in reducing P_{MIN}. Figure3.3a shows increasing warmth in both the lower and upper troposphere during the RI stage, and more intense lower-tropospheric warming tendencies (denoted as "TW") but decreasing upper-level warming tendencies during the weakening stage. The more important roles of the upper-level warming can be more clearly seen from the subsequent steady-V_{MAX} stage, during which period the continuous P_{MIN} falls coincide well with increased warming tendencies in amplitude and depth in the lower stratosphere (denoted as "SW"), while the lower-tropospheric warming tendencies decrease. Note that the tropopause height becomes significantly lower after 26/16-64 as the storm moves to higher latitudes (cf. Figs. 3.3a and 2.2b). Rapid falls in P_{MIN} during the re-intensification stage is consistent with increasing warming tendencies in both the lower stratosphere and troposphere. We wish to mention, however, that none of the previous studies of Sandy, e.g., by Galarneau et al. (2013) and Magnusson et al. (2014), mentioned the presence of SW and its roles in determining the SLP (and P_{MIN}) changes.

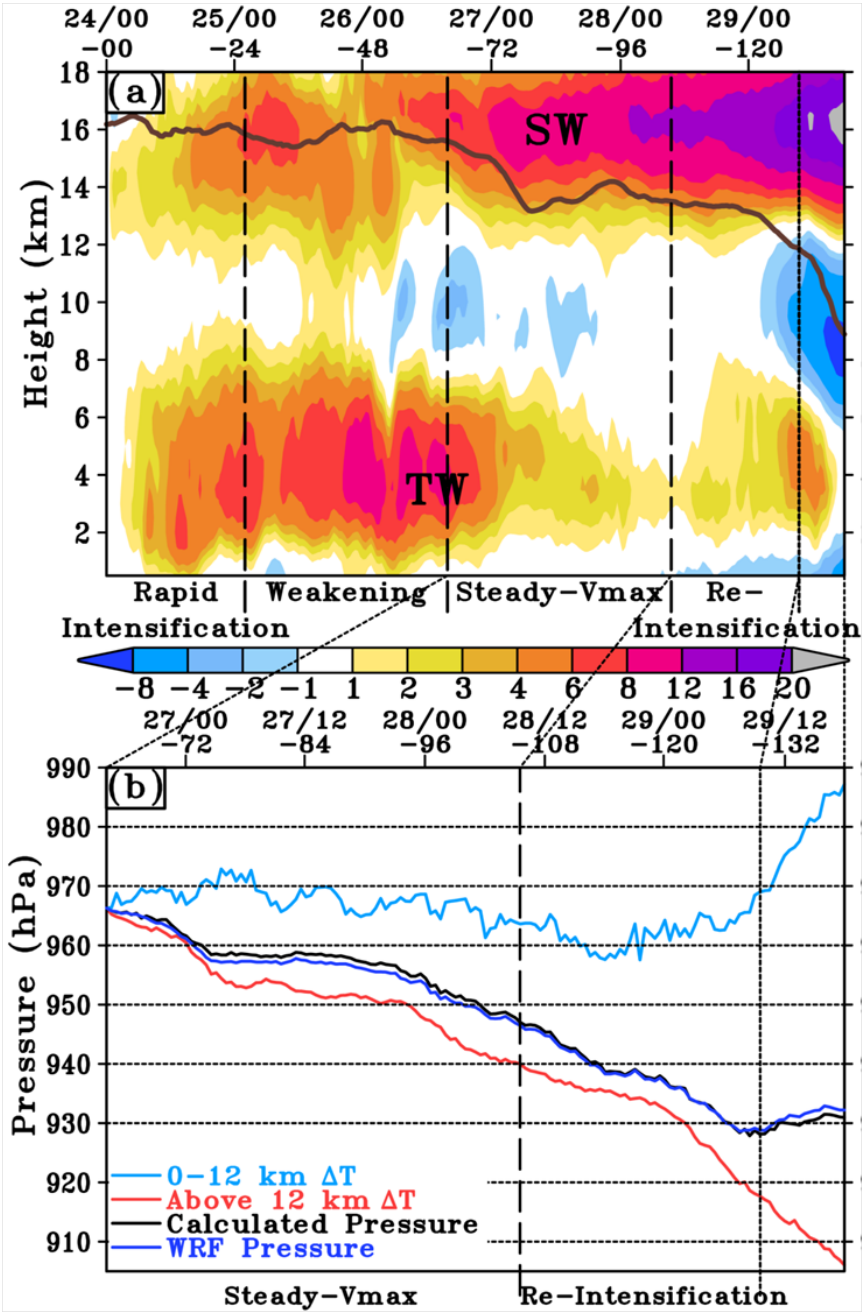

Figure 3.3. (a) Time-height cross section of temperature deviations ΔT(z,t) (shaded, °C), superimposed with the dynamical tropopause (in brown) defined as the 500 km × 500 km area-averaged 2-PVU surface, taken at the storm center from the 138-h simulation, where ΔT(z,t) is defined as the (10 km × 10 km) area-averaged temperature T(z,t) changes with respect to the same area-averaged temperature T(z,t=0 h) at the model initial time. Symbols, "SW" and "TW", denote stratospheric and tropospheric warm deviations, respectively. (b) Time series of the simulated P_{MIN} (dark blue) and the calculated P_{MIN} (black) in hPa from the hydrostatic equation by using the (10 km × 10 km) area-averaged temperature T(z,t)= T(z,t=64 h) + ΔT(z,t) during the final 74-h simulation, where T(z,t=64 h)

is the same area-averaged temperature at 26/16-64. The red (light blue) line is the calculated P_{MIN} following the same procedure as the black line except for using $\Delta T(z,t)$ above z=12 km layer (below z=12 km) only. Data from the WRF 1.667-km resolution domain are used.

To quantify the relative contributions of TW and SW to Sandy's P_{MIN} falls during the later two stages, the following procedures with the Equation (3.2), following Zhang and Zhu (2012), and Cecelski and Zhang (2013), are performed to estimate P_{MIN} changes with respect to 26/16-64 (i.e., the onset of the steady-V_{MAX} stage), where P_{TOP} is model top pressure, g is the gravitational acceleration, and R is the gas constant.

$$P_{MIN} = P_{TOP} \exp\left(\frac{g}{R} \int_{SFC}^{TOP} \frac{1}{T} dz \right) \quad (3.2)$$

(i) The above hydrostatic equation is vertically integrated from the model top to sea level by using the total temperature [i.e., $T(z,t) = T(z, t=64\ h) + \Delta T(z,t)$]; (ii) repeat step (i) by including $\Delta T(z,t)$ only for the layers above 12 km (near 200hPa); and (iii) repeat step (i) by including $\Delta T(z,t)$ only for the layers below 12 km. Step (i) is performed first to ensure that the time series of the simulated P_{MIN}, as given in Fig. 2.3, can be hydrostatically duplicated with little errors (Fig. 3.3b). It is evident from Fig. 3.3b that SW accounts for Sandy's continuous deepening in P_{MIN}, especially the P_{MIN}-falling tendencies associated with increasing SW that are similar to the simulated total rates up to 29/06-126 (see the red line in Fig. 3.3b). In fact, without the contribution of SW, the weak TW produces little changes in P_{MIN} during the steady-V_{MAX} stage (see the blue line in Fig. 3.3b), which is consistent with little

intensity changes in V_{MAX} given in Fig. 2.3a. Figure3.3b also shows that increasing TW during the re-intensification stage could produce about 5~6 hPa falls in P_{MIN} relative to 28/10/106 compared to the SW-induced about 24 hPa falls, indicating further the more important contributions of SW than TW to Sandy's P_{MIN} falls.

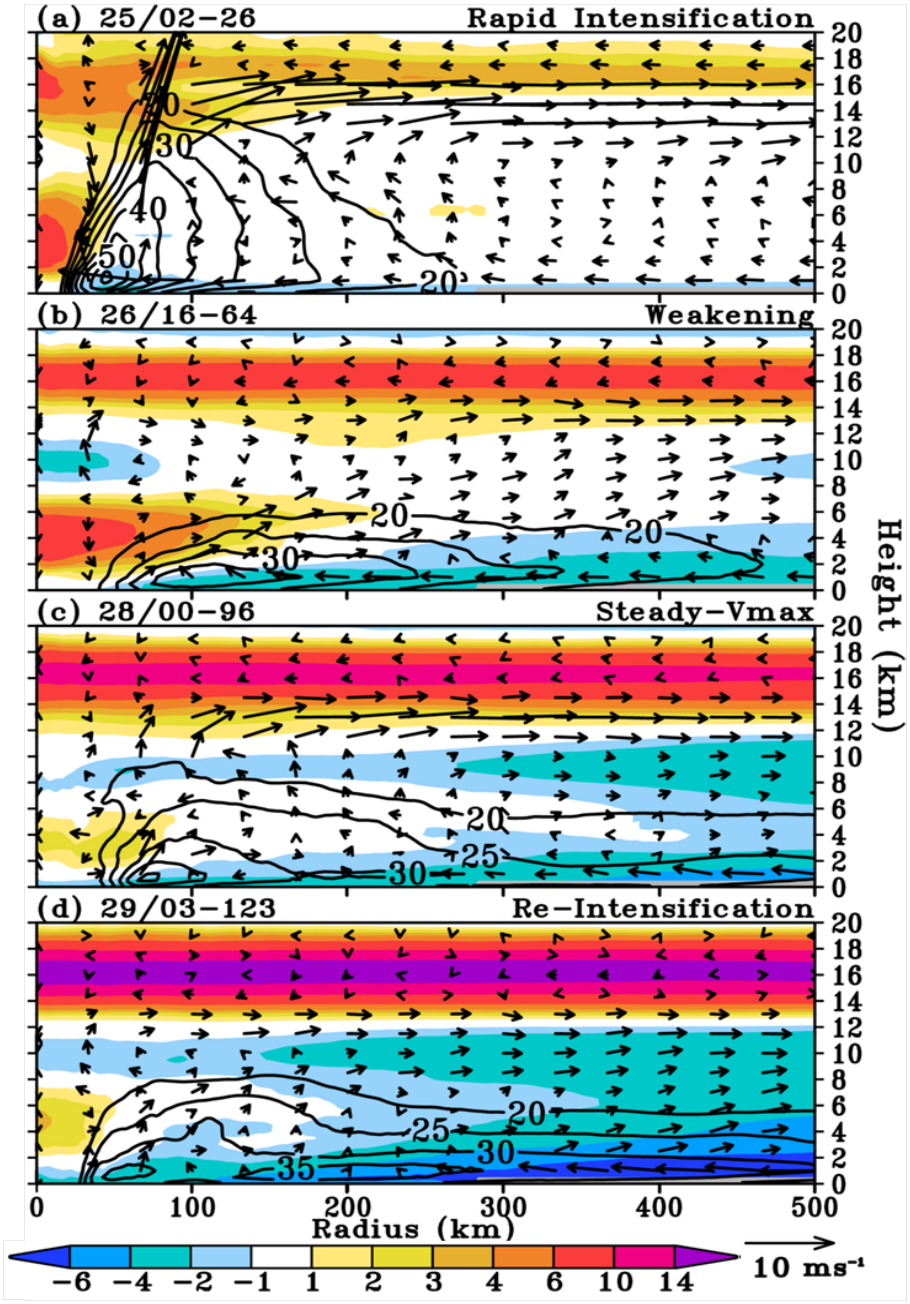

Figure 3.4. Radial-height cross section of the azimuthally averaged temperature deviations ΔT(r,z,t) (shaded, °C), and tangential wind speed (contoured at 5-m s^{-1}

intervals above 20 m s^{-1}), superimposed with in-plane flow vectors (with vertical velocity multiplied by 10) at (a) 25/02-26, (b) 26/16-64, (c) 28/00-96, and (d) 29/03-123 from the WRF 1.667-km resolution domain. $\Delta T(r,z,t)$ is defined as temperature changes with respect to T(r,z, t=0 h) that is azimuthally averaged temperature at the model initial time. Horizontal axis indicates the distance (km) from Sandy's vortex center.

Figure 3.4 shows the height-radius (z-r) maps of warming, i.e., $\Delta T(r, z)$, and tangential winds, superimposed with in-plane flow vectors during the four different stages. We see the development of an intense axisymmetric vortex with a peak intensity of more than 55 m s^{-1} at the end of the RI stage (i.e., 25/02-26), and then its peak intensity decreases to 35 m s^{-1} at 26/16-64, but re-intensifies at 29/03-123 as the 35 m s^{-1} wind area expands significantly. Corresponding to the decreasing intensity is the general weakening of TW, except at 29/03-123. Of importance is the continuous increase in amplitude (i.e., from 3°C to over 15°C) and depth (i.e., from 2.5 – 5 km) of SW near the tropopause or in the lower stratosphere, accompanied by the outward expansion of intense rotational flows. That is, the 30 m s^{-1} isotach coverage increases from R=130 km at 25/02-26 to R = 270 km at 28/00-96, and over R = 500 km at 29/03-123. Of further importance is that unlike in the studies of Chen and Zhang (2013), *this SW occurs above the upper outflow layer* even during the earlier stages when the upper outflows are intense (Figs. 3.4a,b). This implies that the overspread of the SW air is not related to Sandy's upper-level outflows. This is particularly true during the later stages when Sandy's rotation is shallow with little organized upper-level outflows (i.e., above z = 12 km; see Figs. 3.4c,d). Moreover, the SW air is not just distributed in the core region, unlike the presence of a typical TW core in the eye,

but spread from the west to east through the core region, as will be further seen in the next subsection.

Figure 3.4 also shows indirectly the intrusion of cold air from higher latitudes, which is consistent with that shown in Figs. 3.1a-f. The cold intrusion into the proximity of the storm occurs first in the lowest 4-km layer after entering the weakening stage (cf. Figs. 3.4b and 3.1b). This shallow, PBL-based cold air mass originates from the east-Canadian high (Fig. 2.1b), and it tends to wrap around the warm-cored storm except in the northeastern quadrant where frontal rainbands develop frequently (Figs. 3.4c,d and 3.1d-g). Despite the deep-layer cold intrusion, Sandy still keeps its TC-like characteristics with a distinct midlevel warm core, even at the end of the 138-h simulation, albeit with decreased depth (and pronounced frontogenesis). Nevertheless, the cold air intrusion appears to help maintain radial thermal gradients, thereby sustaining Sandy's cyclonic circulation at hurricane intensity. This will be further discussed in the next subsection.

3.3. Origin of the lower-stratospheric warm air and its influences

After seeing the important contributions of the lower-stratospheric warming to P_{MIN} falls, it is desirable to examine its origin and the evolution of tropopause height during Sandy's poleward movement.

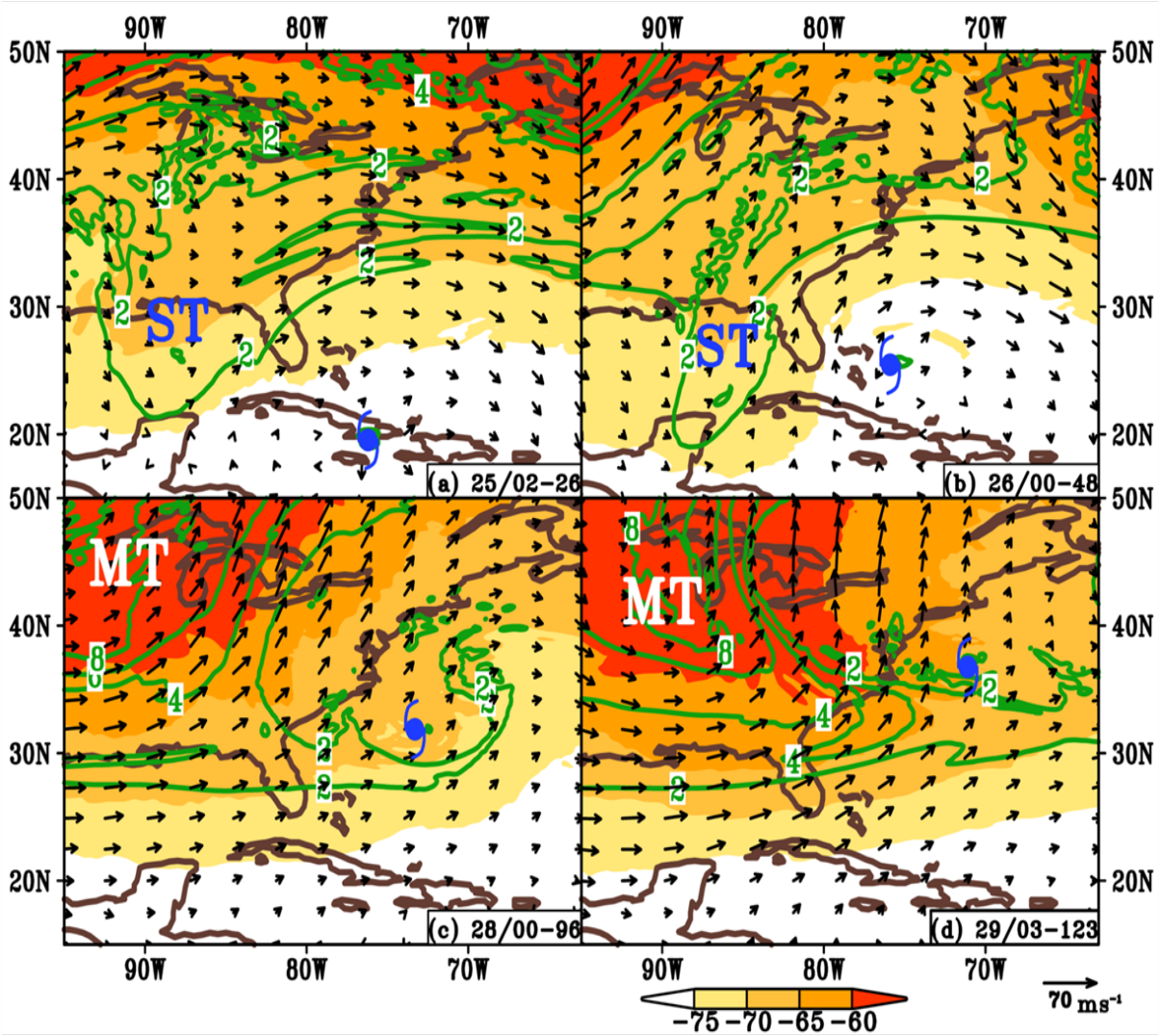

Figure 3.5. Horizontal distribution of potential vorticity (contoured at 2, 4, 6 and 8 PVU) at z = 12 km (near 200-hPa level), and temperature (shaded, °C) and horizontal wind vectors at z = 16 km at (a) 25/02-26, (b) 26/00-48, (c) 28/00-96, and (d) 29/03-123 from the WRF 15-km resolution domain. Symbols, "ST" and "MT", indicate a subtropical short-wave and a midlatitude long-wave trough, respectively.

Figure 3.5 presents the evolution of PV at z = 12 km, and temperature and horizontal wind vectors at z = 16 km where the lower-stratospheric warming is peaked (Fig. 3.4). The lower stratosphere exhibits clearly a reversed temperature gradient from that in the troposphere, i.e., with warmer air poleward, as has also been shown in Fig. 2.2b. Sandy is located ahead of a weak *subtropical trough* (ST in Figs. 3.5a,b) at the early stages and then an intense *midlatitude trough* (MT in Figs. 3.5c,d). The tropopause, as defined by 2 PVU, is relatively lower at higher latitudes, especially undulating in the two troughs regions. As the ST dips southward at 26/00-48 (Fig. 3.5b), its associated lower-stratospheric warm air begins to interfere with Sandy's upper anticyclonic outflow from the west. By 28/00-96, the core region has been warmed about 5°C (Fig. 3.5c). Note that the 2-PVU air wraps around the storm, implying that the ST with lower-tropopause heights has merged into Sandy's core region. Given the development of a shallow secondary circulation and weak intensity at this stage (Figs. 2.3a and 3.4c), the overspread of this warm air is clearly associated with the larger-scale circulation, rather than Sandy's upper-level outflows. This is more evident during Sandy's re-intensification stage when the MT becomes northwest-southeast-oriented across the storm, with little evidence of convectively generated anticyclonic outflows (Fig. 3.5d). By this time, Sandy's lower-stratospheric environment has been warmed more than 10°C, including the core region (cf. Figs. 3.5b,d). Clearly, this could hydrostatically induce a large area of pressure falls in the deep tropospheric layers. Note that due to its faster propagation the MT's influences on Sandy's inner-core circulation occur earlier than its corresponding surface cold front.

Figure 3.6 shows more clearly the vertical structure of tropopause undulation associated with the MT and its possible influences on Sandy's circulations. A 360-K isentropic surface analysis at 29/09-129 shows its rapid descent toward the bottom of the MT, forming a "warm pocket" in the southeastern quadrant of the storm (Fig. 3.6a). Figure 3.6b shows a sharp drop in tropopause height (down to 5.5 km) along the MT's cyclonic flow, which is more than 6 km lower than that in Sandy's immediate environment to the east. Associated with the lower tropopause height are the gentle descent of stratospheric air and downward sloping of isentropic surfaces, and the formation of a deep-layer (5.5 – 14 km) warm anomaly.

The above scenarios are similar to the work of Hirschberg and Fritsch (1991a, b) who studied the relationship between tropopause undulations and extratropical cyclogenesis downstream. They found that the tropopause height in the upper-level trough region is lower than its environment because of descending warm stratospheric air. They claimed that the upper-level warm advection from this upstream region induces surface SLP falls leading to surface cyclogenesis. Similarly, through the use of 54.96-GHz microwave images, Velden (1992) noted the important roles of a warm anomaly at the tropopause in extratropical surface cyclogenesis. Although some previous studies have shown the interaction between tropopause undulation and TCs (e.g., Bosart and Lackmann 1995; Atallah and Bosart 2003), few have examined the relative influences of the associated stratospheric warmth vs. diabatic heating on TC intensity and structures.

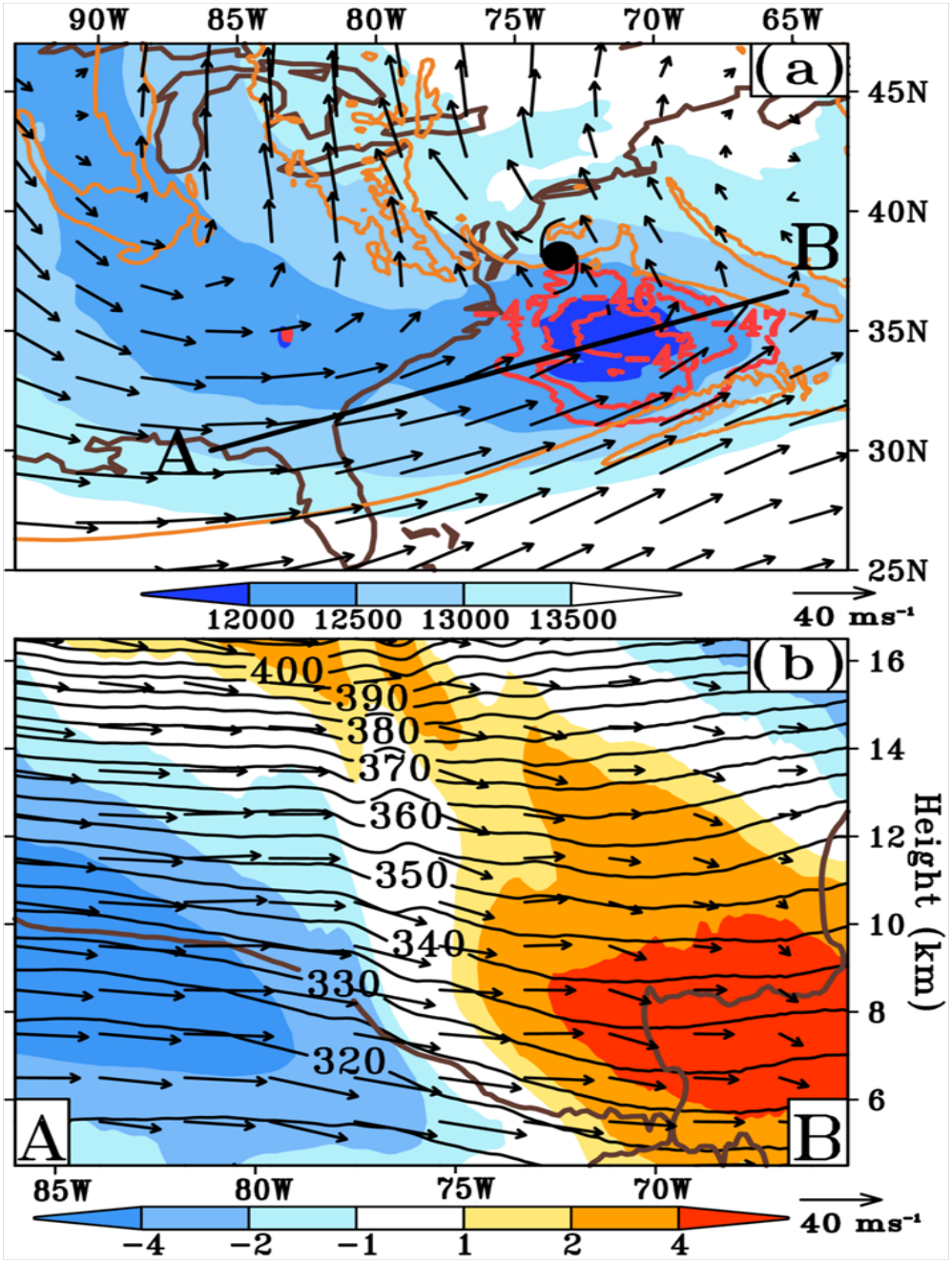

Figure 3.6. (a) Horizontal distribution of the 360-K isentropic surface height (shaded; m) and wind vectors, 12-km potential vorticity (orange-contoured at 2 and 8 PVU) and temperature (red-contoured at -47, -46 and -45°C) at 29/09-129. (b) Vertical cross section of potential temperature (black-contoured at 5K intervals), the dynamic tropopause defined by the 2-PVU line in brown, in-plane flow vectors (with vertical velocity multiplied by 100), and temperature deviations (shaded, °C) along line AB given in (a). Data from the WRF 15-km resolution domain are used.

It is obvious that the advection of the lower-stratospheric warm air across the storm must also affect Sandy's spatial distribution of SLP falls. To this end, the same methodology as that used to obtain Fig. 3.3b is adopted to estimate the relative influences of lower-stratospheric (SW_H) and tropospheric (TW_H) warming on the horizontal distribution of SLP falls. Again, as a first step, the model-simulated SLP distributions, like those shown in Figs. 3.1h-n, are reproduced by integrating the hydrostatic equation from the model top to sea level with the total temperature field, i.e., $T(x,y,z,t) = T(x,y,z, t = 64\ h) + \Delta T(x,y,z,t)$, where $\Delta T(x,y,z,t)$ is the temperature difference field between time t and 26/16-64. Then, $\Delta T(x,y,z,t)$ in the layers below (TW_H) and above (SW_H) z = 12 km is used, together with $T(x,y,z, t = 64\ h)$, to integrate the hydrostatic equation, respectively. The hydrostatically calculated results are given in Fig. 3.7, showing widespread SLP falls of large amplitudes (e.g., up to 15 - 36 hPa from 28/00-96 to 29/09-129, shown in purple contours) relative to 26/16-64 over the analysis domain. In the absence of TW_H, SW_H produces much greater SLP falls than the total (e.g., up to 21 – 60 hPa from 28/00-96 to 29/09-129), with the amplitudes decreasing cyclonically from the northwestern to southeastern corner (Figs. 3.7d-f). The general patterns of the SLP falls and mass-weighted SW_H at 29/09-129 correspond well to the cyclonic warm advection associated with the upper-level trough (cf. Figs. 3.7f and 3.6a). From PV perspective, we may attribute the large

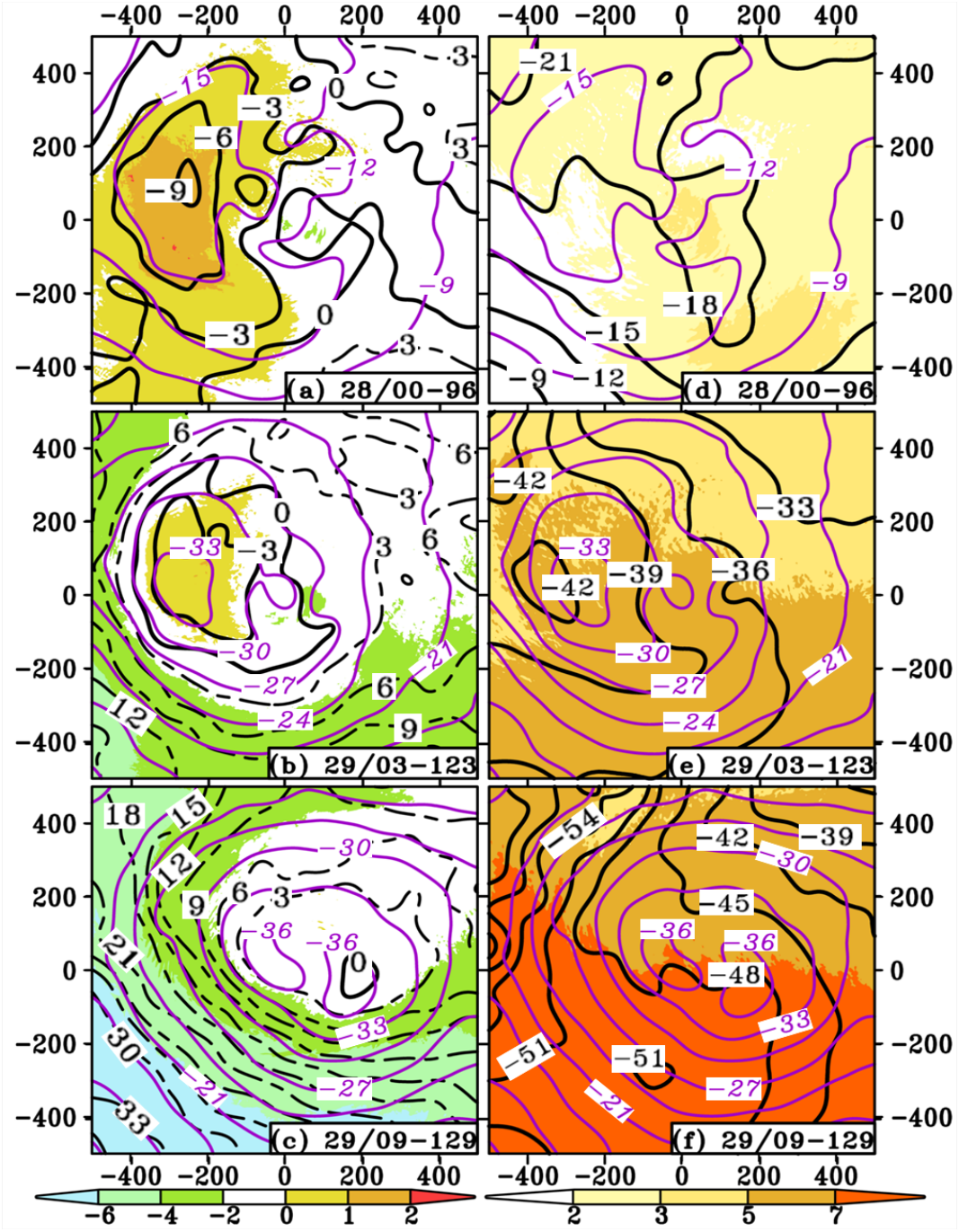

Figure 3.7. (a)-(c) Horizontal distribution of the hydrostatically calculated total SLP changes (purple-contoured at 3-hPa intervals), and the hydrostatically calculated SLP changes (black-contoured at 3-hPa intervals: solid/negative, dotted/positive) associated with the mass-weighted TW changes (shaded, °C), i.e., in the layers below 12 km (the mass-weighted temperature changes are estimated by $\int \Delta T(x,y,p,t)dp / \int dp$, valid at 28/00-96, 29/03-123, and 29/09-129, respectively, from the WRF 1.667-km resolution (500 km× 500 km) subdomain. Both the temperature and SLP changes are calculated with respect to 26/16-64. (d) – (f) As

in (a)-(c) but for the mass-weighted SW, i.e., in the layers above 12 km. See text for more details.

pressure falls to the arrival of upper-tropospheric cyclonic PV. Clearly, it is the eastward and then cyclonic progression of the SW_H air that results in the widespread SLP falls.

In contrast, the SLP falls induced by TW_H during the steady-V_{MAX} stage are small in both amplitude and coverage (Fig. 3.7a). Because the mass-weighted TW_H at 28/00-96 relative to 26/16-64 occurs mainly behind the western frontal rainband, it induces little SLP falls in the core region, but 6-9 hPa drops over an elliptic-shaped area corresponding to the TW_H distribution in the western semicircle (cf. Figs. 3.7a and 3.1d). Subsequently, the outer regions experience rapid SLP rises as they are gradually filled by colder air from the east-Canadian high, except in the northeastern quadrant that is influenced by warm frontogenesis (cf. Figs. 3.7c and 3.1n). For instance, the mass-weighted TW_H in the warm southern regions at 29/09-129 is more than 6K colder than that at 26/16-64 (Fig. 3.7c) and about 30K less in θ_e than that at 28/00-96 (Figs. 3.1d-g). Much less cooling occurs in the core region due to the presence of intense rotation, and over the cold northern regions, especially in the frontogenesis region. As a result, SLP rises of more than 35 hPa from that at 26/16-64 appear in the outer regions compared to little SLP changes in the core. From a mass-wind balance view, the resulting large radial SLP gradients and thermal gradients would superimpose pronounced tangential flows on the reference (26/16-64) flow field.

While SW_H induces larger SLP falls, its associated *radial SLP gradients* are smaller than those induced by TW_H, especially in the core region, as can be seen from the density of their falling SLP isobars. Only at 29/09-129, large falling-SLP gradients occur in the western semicircle due to the approaching of the cold front (cf. Figs. 3.7f and 3.1g, n). In general, SW_H causes SLP falls across the storm from the west to east, which generates asymmetries in horizontal winds, thereby expanding Sandy's lower pressure coverage and associated cyclonic circulation, as shown in chapter 3.1. In contrast, negative TW_H and its cyclonic advection account for larger (much less) SLP increases over the warm southern (cold northern) regions and frontogenetic forcing in the northeastern quadrant, respectively. Nevertheless, despite the large SW_H-induced SLP falls, it is still TW_H and its associated dynamical processes that are responsible for a sizeable amount of the intensity changes of rotational winds and the size expansion, especially at later stages. Unlike in some previous studies (e.g., Klein et al. 2000), the SW_H-induced SLP field presented herein just modulates these changes.

3.4. Inner-core vertical structures

So far, we have examined the vertical thermal structures with respect to two different reference times. When they are plotted with respect to *the storm environment* (Figs. 3.8b-d), the lower-stratospheric warmth is no longer visible because of the rapid overspread of the lower-stratospheric air across the storm. This appears to explain why the impact of the lower-stratospheric warmth on Sandy's large SLP falls was not noted by the previous studies of the case.

Figure 3.8a shows that the RI stage is characterized by nearly symmetric eyewall structures with a typical in-up-out secondary circulation. Note the development of double warm cores: a typical midtropospheric one of greater than 6°C located at z = 4 km (Zhang et al. 2000), and a lower-stratospheric one of more than 2°C at z = 16 km. The latter is not related to the horizontal advection of the lower stratospheric warm air from the west, but the descent of lower-stratospheric air above associated with convective bursts (see Chen and Zhang 2013); it diminishes rapidly after entering the weakening stage, as also shown in Figs. 3.3a and 3.4a,b. As VWS increases, wavenumber-1 convective asymmetry becomes more evident. The TC vortex, together with its warm column (Fig. 3.8b), tilts to the downshear left (Reasor et al. 2004; Davis et al. 2008), so the vertical cross section is taken along a line that is 45-60° rotated to the left of the VWS vector (see Figs. 2.3 and 3.1). Similarly, lower-level inflows and upper-level outflows are no longer symmetric, i.e., with a low-level inflow and an upper-level outflow on the downshear left, and a reversed flow configuration on the upshear right; they are similar to those observed and simulated in sheared TCs, e.g., Hurricanes Olivia and Jimena (Black et al. 2002) and Bonnie (Zhu et al. 2004). In particular, a deep inflow layer (i.e., z = 2-12 km) of lower-θ_e air occurs on the upshear right with some cloud hydrometeors, and an upper cloud mass (i.e., above z = 8 km), where rotational flows (and inertial stability) are weak (cf. Figs. 3.4b and 3.8b), intrudes into the eye center, thereby diminishing warm columns above through evaporative cooling of cloud hydrometeors. As a result, P_{MIN} rises notably as it is mainly associated with a warm column in the lowest 6 km (cf. Figs 3.8b, 2.3a and 3.1i).

The steady-V_{MAX} stage is seen with weakening convection in the partial eyewall and much reduced warm-core intensity (cf. Figs. 3.8c and 3.1d). Little eyewall characteristics are present on the upshear side where deep convection is suppressed. In spite of the weakening warm core, the SLP fields keeps dropping (cf. Figs. 2.3a, 3.2a and 3.3) as a result of the previously mentioned advection of stratospheric warm air, which can be seen from the lowering tropopause height from z = 16 to 14 km (cf. Figs. 3.8b and 3.8c). The tropopause height falls further to z = 12-13 km after entering the re-intensification stage, in which a robust midlevel warm core re-develops together with enhanced deep convection in the northwestern quadrant of the partial eyewall (Fig. 3.8d). The level of the peak warmth occurs near z = 5 km, which is similar to the satellite-observed warm core of Sandy by Zhu and Weng (2013). This warm core can be seen being more associated with compensating subsidence that is peaked near the top of the eyewall convection where inertial stability is weak. Note that the eyewall convection could only reach as high as 11 km, which is 4-5 km lower than that occurred earlier (cf. Figs. 3.8a-d), as has also been shown in Fig. 3.4. Note also the development of a deep outflow layer *below 6 km* and weak inflows above on the upshear side of the storm, where deep convection is suppressed due to the presence of intense VWS. This lower-tropospheric outflow is of non-typical for typical TCs, and it is associated with the southeastern portion of the frontal rainband (cf. Figs. 3.8d and 3.1f). Its development tends to weaken inner-core rotation, at least locally, because of the unfavorable AAM transport (Yau et al. 2004). Instead, two jets take place on the right and left region outside the cross section (i.e., near R = 200 km; see Figs. 3.1m,n), respectively, as mentioned before.

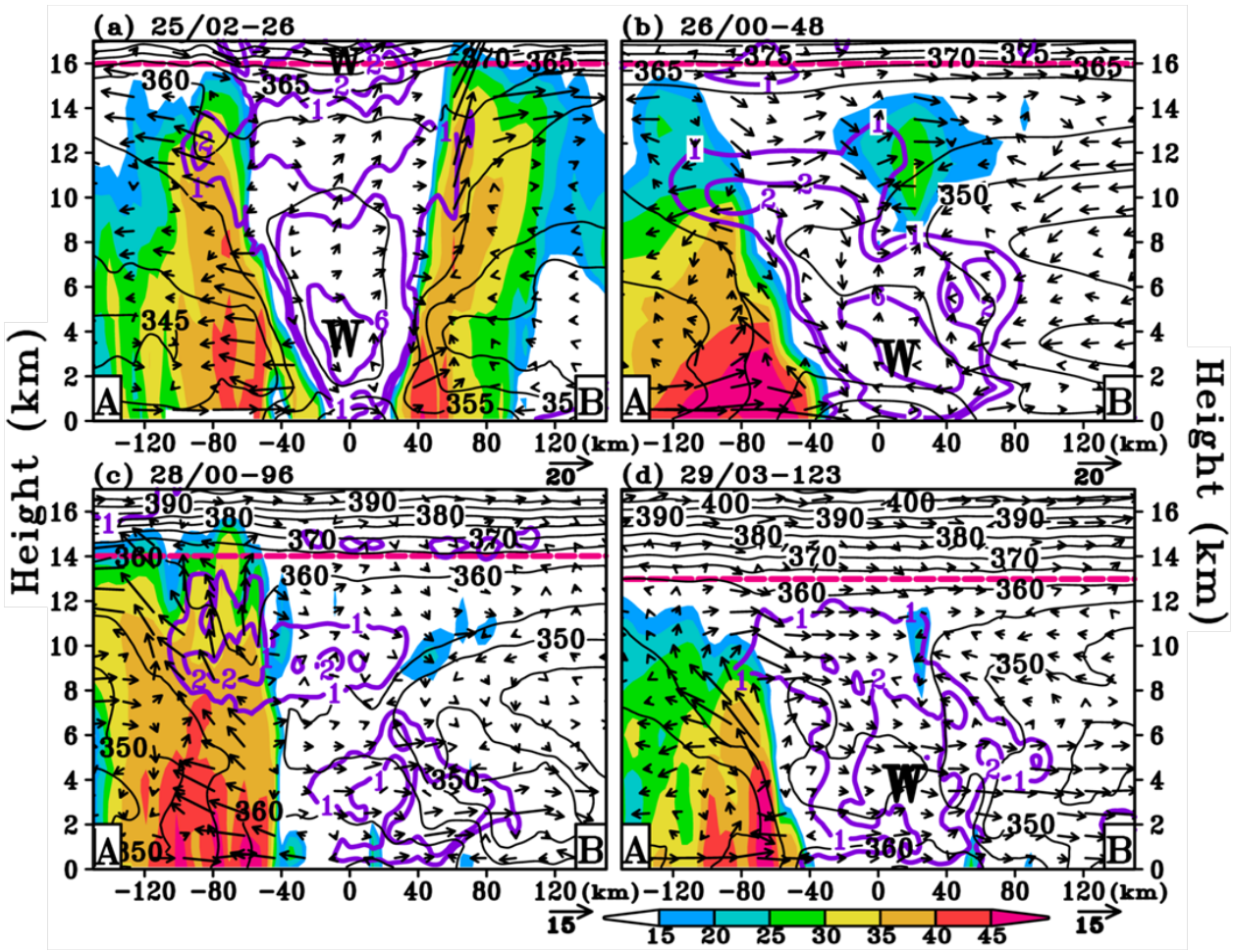

Figure 3.8. Vertical cross section of the simulated radar reflectivity (shaded, dBZ), equivalent potential temperature (θ_e) at 5K intervals, temperature deviations from the corresponding level-averaged value (purple-contoured at 1, 2,and 6K), and storm-relative in-plane flow vectors (with vertical velocity multiplied by 5) from the 1.667-km resolution domain at (a) 25/02-26; (b) 26/00-48; (c) 28/00-96; and (d) 29/03-123 along A-B (through the vortex center) given in Fig. 3.1. The tropopause height (defined in Fig. 3.3a) is denoted by dashed magenta lines. Horizontal axis indicates the distance (km) from the storm center. Letter, "W", indicates the warm-core center.

3.5. Chapter summary

In this part of the study, the relative importance of moist frontogenesis and tropopause undulation in determining the multiple intensity, size, and structural changes of Hurricane Sandy is examined using a 138-h (0000 UTC 24 – 1800 UTC

29 October 2012) cloud-resolving version of the WRF model. Results show that the WRF model reproduces Sandy's life cycle consisting of four distinct development stages: (i) rapid intensification, (ii) weakening, (iii) steady V_{MAX} but with large SLP falls, and (iv) re-intensification prior to landfall. Typical correlations between Sandy's intensity changes and SST and VWS are found during the first two stages. A time-height cross sectional analysis reveals that the large SLP falls during the steady-V_{MAX} and subsequent re-intensification stages result from Sandy's moving into lower-tropopause regions associated with an eastward-propagating MT, where the associated lower-stratospheric warm air is advected across the storm with higher PV wrapped into the core region. Despite the large SLP falls in Sandy's core and ambient regions, we do not see significant increases in PGF_R, and so little changes in the peak rotational wind during the steady-V_{MAX} stage, even in the presence of frontal rainbands in the outer region.

Results also show that Sandy's northward movement over cooler water toward a zonally distributed baroclinic zone associated with an east-Canadian high increases meridional θ_e gradients in the northern semicircle. As a result, a spiral frontogenetic zone/rainband begins to develop in the northeastern quadrant during the weakening stage, where Sandy's high-θ_e (warm) southeasterly flow converges with a low-θ_e easterly flow in the northern environment. The same processes occur for two subsequent spiral frontogenetic zones/rainbands during the steady V_{MAX} and early re-intensification stage, respectively, after the first one is quickly advected into the northwestern quadrant by the intense easterly flow and then diminishes. Cyclonical inward advection of AAM along each spiral frontal rainband tends to produce a spiral

jet extending from its inner V_{MAX} to outer northeastern quadrant. This appears to account for Sandy's continued expansion of the tropical-storm-force wind and structural changes. The merging of the final two frontal rainbands and the enhanced partial eyewall convection into a spiral intensifying frontal rainband results in a much enhanced spiral jet extending from its core (i.e., V_{MAX}) in the southwestern quadrant to the outer northeastern quadrant during the final stage. The subsequent cyclonic inward progression of the jet core (also implying contraction) along the spiral frontal rainband and eyewall leads to the re-intensification of the storm. Meanwhile, cyclonic advection of the low-θ_e (cold) air into Sandy's southern semicircle increases radial thermal contrasts and SLP gradients, thus generating and maintaining a (balanced) swirling jet in its southern sectors. Although some of the above results remain to be validated by high-resolution observations in the future, our work shows several interesting features related to the ET of TCs that have not been previously shown: (i) steady V_{MAX} with pronounced P_{MIN} falls; (ii) multiple warm frontogenesis events within Sandy's internal circulation; (iii) the important roles of the lower stratospheric warmth in generating widespread SLP falls, but with little impact on the maximum rotational wind speed of the storm; and (iv) re-intensification prior to a warm seclusion due mostly to Sandy's internal vortex dynamics.

In conclusion, we may state that it is mainly (i) the moist frontogenesis processes resulting from the convergence of Sandy's high-θ_e southeasterly flows with low-θ_e easterly flows from the northern environment that lead to the continued size expansion and structural changes, and (ii) eyewall convection invigoration, the merged spiral frontal rainband and partial eyewall convection, and the subsequent

cyclonic inward contraction of a well-developed jet core along the merged rainband that account for Sandy's re-intensification. The lower-stratospheric warmth makes large contributions to P_{MIN} and environmental SLP falls, and likely size expansion during the final stage, but it just plays a role in modulating Sandy's structural and intensity changes. Although the impact of lower-stratospheric warm air associated with tropopause undulation was studied for extratropical cyclogenesis (Hirschberg and Fritsch 1991a, b), this study reveals that this warmth can also affect TCs during ET.

Chapter 4. The upper-level outflow dynamics of Hurricane Sandy

4.1. Introduction

Although some previous ET studies (Klein et al. 2002; Evans and Prater-Mayes 2004) argued that the upper-level divergence associated with upper-level jet stream can re-intensify the storm during ET, they did not investigate the outflow structure and the influence of dynamic instabilities of the outflow layer on re-intensification. In this Chapter 4, we will focus on the outflow layer when Sandy undergoes ET and interacts with the upper-level jet stream.

Chapters 4.2 and 4.3 will describe the basic kinematic and physical characteristics of the outflow layer, as well as the methodology to distinguish the outflow layers of different origins (i.e., the outer frontal rainband vs. the eyewall convection), based on the equivalent potential temperature (θ_e). Chapters 4.4-4.6 investigate the dynamic instabilities of the outflow layer, and the possible roles of radiative process in dynamic instabilities. Chapter 4.7 discusses how these instabilities of the outflow layer can affect the re-intensification of Sandy based on the mass flux and buoyancy. Chapter 4.8 presents several sensitivity simulations in order to understand the impact of the Gulf Stream and the upper-level trough/jet stream on the intensity and structural changes of Sandy. Unlike Chapter 3, we will focus on the scenarios of 28 and 29 October 2012 when Sandy moves to the midlatitudes since the goal of this chapter is to study the impact of the upper-level jet on the outflow channel and Sandy's intensity changes. Note that the re-intensification

stage herein implies the period of 0000 UTC 29 to 0900 UTC 29 October when the cyclonic tangential wind (or storm vortex) in the lowest 1-km layer re-intensifies significantly, as shown in Fig. 3.2.

4.2. Kinematical structures of the outflow layer

Figure 4.1a illustrates the general synoptic and outflow patterns during the re-intensification stage, which were characterized by an upper-level trough/jet system with an extensive cirrus field. The gigantic trough accompanied by the upper-level jet was located over the Eastern Canada, and the outflow from Sandy blew towards this jet stream, forming the large cirrus cloud field. The western edge of the cirrus cloud field was almost collocated with the axis of the upper-level jet and exhibited sharp pattern, while the eastern edge was not well defined. The sharp edge appears to be caused by strong inertial stability along the axis of the jet stream, where strong horizontal potential vorticity (PV) gradient exists. The WRF model reproduces such observed synoptic pattern quite well. Relative humidity near 300 hPa, which represents the

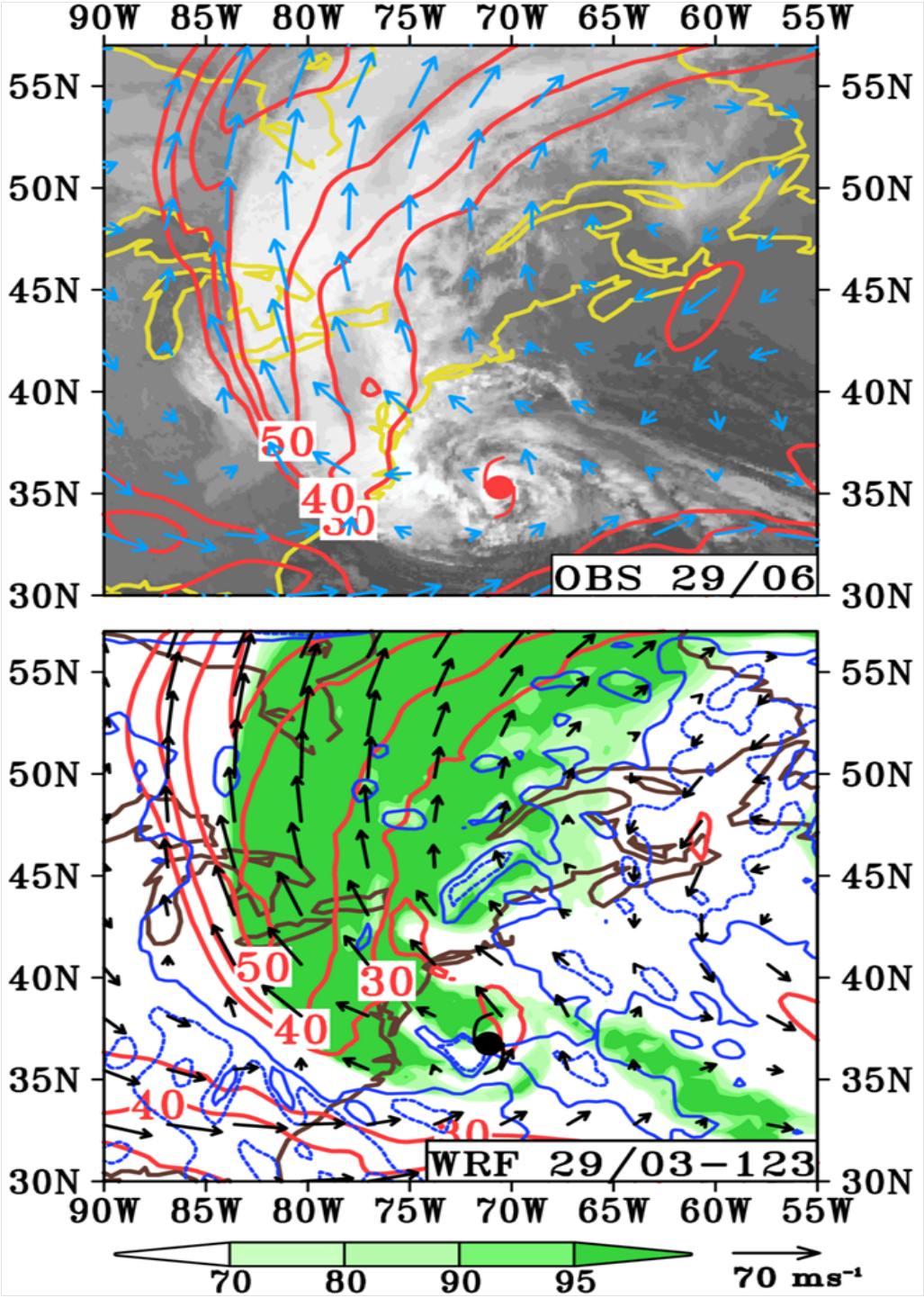

Figure 4.1. (a)The NCEP final analysis of the wind speed (contoured at 30, 40, 50, and 60 m s^{-1}), and horizontal wind vectors at 300 hPa, superimposed with satellite IR images from the Gridded Satellite (GridSat-B1) data archive of National Climatic Data Center of NOAA (http://www.ncdc.noaa.gov) at 0600 UTC 29 October 2012. (b) Horizontal distribution of simulated wind speeds (red-contoured at 30, 40, 50, and 60 m s^{-1}), relative humidity (shaded, %), vertical

velocity (blue-contoured at -1, and -5cm s^{-1}, with solid and dotted line, respectively), and horizontal wind vectors at z = 9 km (near 300-hPa level) at 29/03-123. A 9-point smoother is applied to the vertical velocity field. Data from the WRF 45-km resolution domain are used. Hurricane symbol indicates the location of Sandy.

cloud field, extends from the storm center to the eastern part of the upper-level jet stream. Based on the wind vector distribution, this cloud field is closely related to the outflow of Sandy. It is also interesting that there is a weak but widespread descending motion outside of the cirrus field, which could be due to a long-wave cooling.

Figure 4.1 suggests that Sandy's outflow is closely connected to the upper-level jet stream. However, both observation and coarse resolution data are not suitable to study the associated structures in detail. In addition, Sandy has two distinct convection areas (i.e., in the eyewall and frontogenesis) after it moves to the midlatitudes. Thus, Sandy may have complex outflow structures, and the high resolution data from 5- and 1.667-km domains will be utilized to investigate the detailed structures of the outflow layer. Like in Chapter 3, ground relative flows in cylindrical and Cartesian coordinates will be used for our analysis.

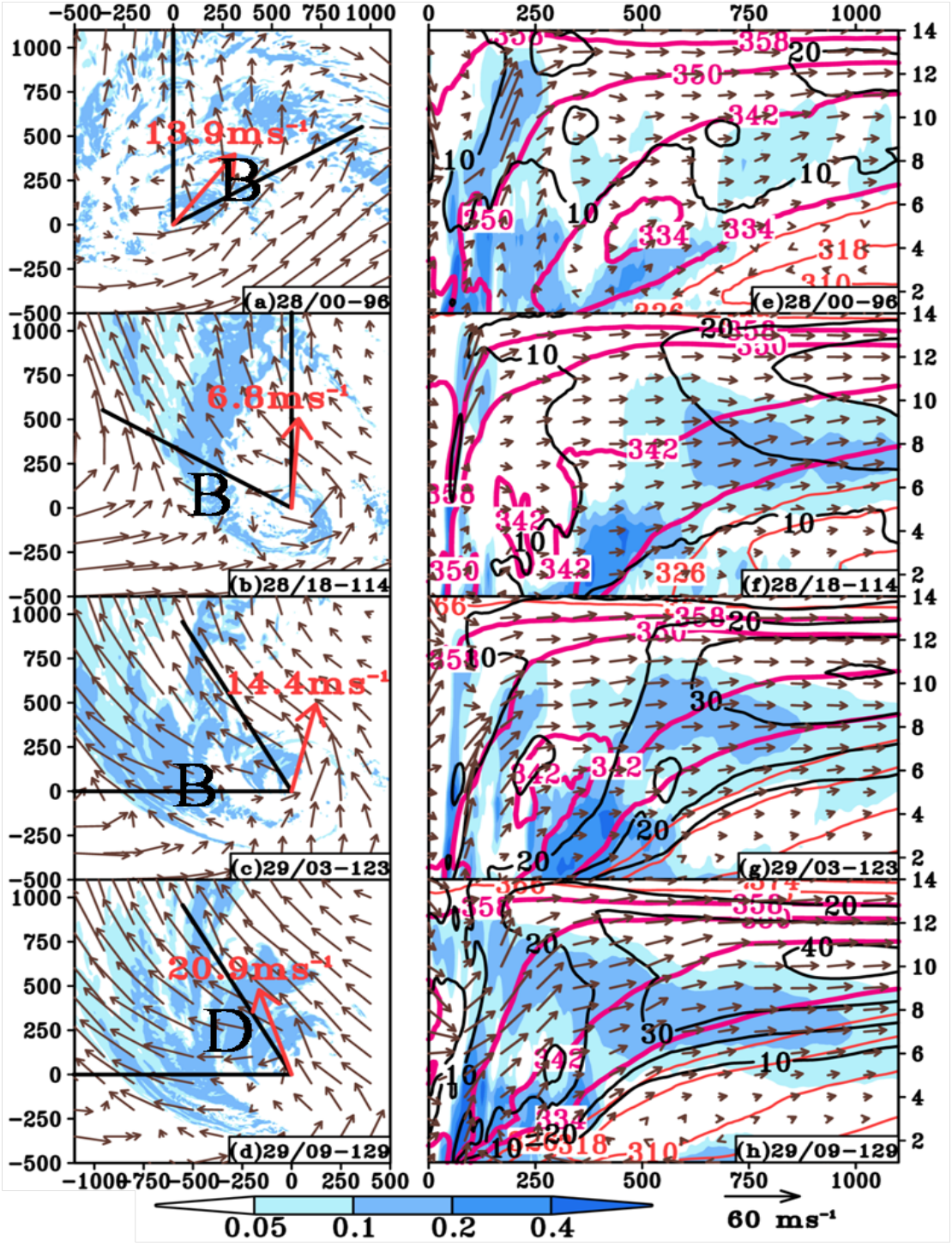

Figure 4.2. (a)-(d) Horizontal distribution of 9-km horizontal wind vectors, and cloud mixing ratio (shaded, g kg^{-1}), valid at 28/00-96, 28/18-114, 29/03-123, and 29/09-129, respectively. Horizontal and vertical axes indicate the distance (km) from the TC vortex center. Letters, "B", and "D" indicates various frontal rainbands as described in Fig. 3.1. The 200-850 hPa VWS direction and magnitude are denoted as red arrow and letters. (e) – (h) As in (a) – (d) but for radial-height cross section

of wind vectors, cloud mixing ratio (shaded, g kg^{-1}), equivalent potential temperature (θ_e, red-contoured at intervals of 8K with θ_e = 334, 342, 350, and 358K highlighted with magenta line), and the outward radial velocity (black-contoured at 10-m s^{-1} intervals). Cloud mixing ratio is defined as the summation of cloud water and ice. Same for the rest of figures. Fields are averaged between two azimuths which are indicated in (a)-(d). Horizontal axis indicates the distance (km) from the TC vortex center. Data from the WRF 5-km resolution domain are used.

Figure 4.2 depicts the rough evolution of the upper-level flow and the cloud patterns during the period of interest, i.e., 28~29 October 2012. At 0000 UTC 28 October, or after 96 h into the integration (hereafter 28/00-96), the cloud region exists near the center and at 500-km radius, which could be associated with the outer rainband (Fig. 4.2a). Due to high 200-850 hPa vertical wind shear (VWS) around this time, strong eyewall convection is collocated with a frontal rainband B in the northeastern quadrant (downshear) of the center. The vertical-radial cross section reveals that deep convection associated with the inner eyewall and relatively shallow convection related to the frontal rainband B within 300-km radius generate the outflow around 13 km and 10 km, respectively (Fig. 4.2e). Because Sandy has two distinct types of deep convection, it appears that the storm also has multiple outflows. Based on the vertical structures of θ_e surfaces, the outflow between 350-and 358-K isentropes is closely related to the tall eyewall convection, while the outflow of 342-350-K layer (and 334-342-K layer) is driven by the frontal rainband B, as also shown in Fig. 3.1k. It can be seen that the upper-level outflows associated with the eyewall and frontal convection are directed northeastward prior to the re-intensification stage. In the early stage of re-intensification (Figs. 4.2b and 4.2f), the outflow direction is shifted to northwest, where the upper-level jet stream is oriented. This directional

shift is caused by the following two processes. First, the frontal rainband B propagates from the northeastern to northwestern quadrant after 28/00-96 (Figs. 4.2a and 4.2e), and the direction of VWS changes from northeast to north. As a result, deep convection in the eyewall and frontal rainband (and its outflows) occurs in the northwestern quadrant. Second, as the frontal rainband B propagates westward, it is separated from the eyewall convection, and its outflow is almost merged with the upper-level jet stream, which is located at 1000 km from the center near z = 11-km level. Most of the outflow associated with the frontal rainband take place between 336-, and 342-K isentropes, while deep and weak radial outflow occurs above the 342-K isentrope within 500-km radius, which is driven by the eyewall convection. Outside the 500-km radius is the frontal rainband B with strong θ_e gradient in the lower troposphere. When Sandy undergoes re-intensification around 29/03-123, the upper-level wind is shifted more to the west (Fig. 4.2c). This suggests strong interaction between the convectively generated outflow and the upper-level jet stream approaching from the west (Fig. 4.1b). Unlike that at 28/18-114, the outflow increases significantly within the 500-km radius and between 342-, and 350-K isentropes (Fig. 4.2g). Thus, the eyewall convection has a quite deep outflow layer (where the radial velocity is greater than 10 m s^{-1}) that extends from 6- to 12-km level. The frontal convection also has a significant outflow between 334-and 342-K isentropes.

Figure 4.2g also shows some interesting features of the outflow from the eyewall convection; (i) it has some slantwise pattern, and (ii) it is located just above the outflow of the frontal convection. Also the isentropes and radial velocity fields indicate that the outflow with a θ_e value lower than 350K is influenced by the jet

stream, while the outflow with a θ_e value greater than 350K is not. Further discussion will be provided in relation to Fig. 4.3. Near the second intensity peak at 29/09-129 (Figs. 4.2d and 4.2h), the eyewall and the frontal rainband B are totally merged, and the deep slantwise ascent exists beyond 100-km radius. Like that at 29/03-123, the eyewall exhibits a significant slantwise convection pattern which is quite different from a typical mature TC.

Vertical-radial cross sections show that *the outflow structure is stratified; the outflow layer of the frontal rainband exists beneath that of the eyewall convection*. The former has relatively lower values of θ_e than the latter because it is originated from the outer region of the storm, where surface temperature is not as warm as the core region. Therefore, θ_e is a useful variable to separate atmospheric fields as noted by Pauluis and Mrowiec (2013), and Mrowiec et al. (2016). Based on this perspective and Fig. 4.2, Sandy's outflow can be roughly divided into three components, (i) the lowest outflow layer from 334 to 342K, which is mostly originated from the outer frontal convection, (ii) the intermediate layer from 342 to 350K, which plays an important role during the re-intensification stage because another outflow channel associated with the eyewall convection develops in this layer on 29 October, and (iii) the layer from 350 to 358K that is related to the innermost part of the eyewall convection. These multiple outflow layers appear to be different from those discussed by Emanuel and Rotunno (2011).

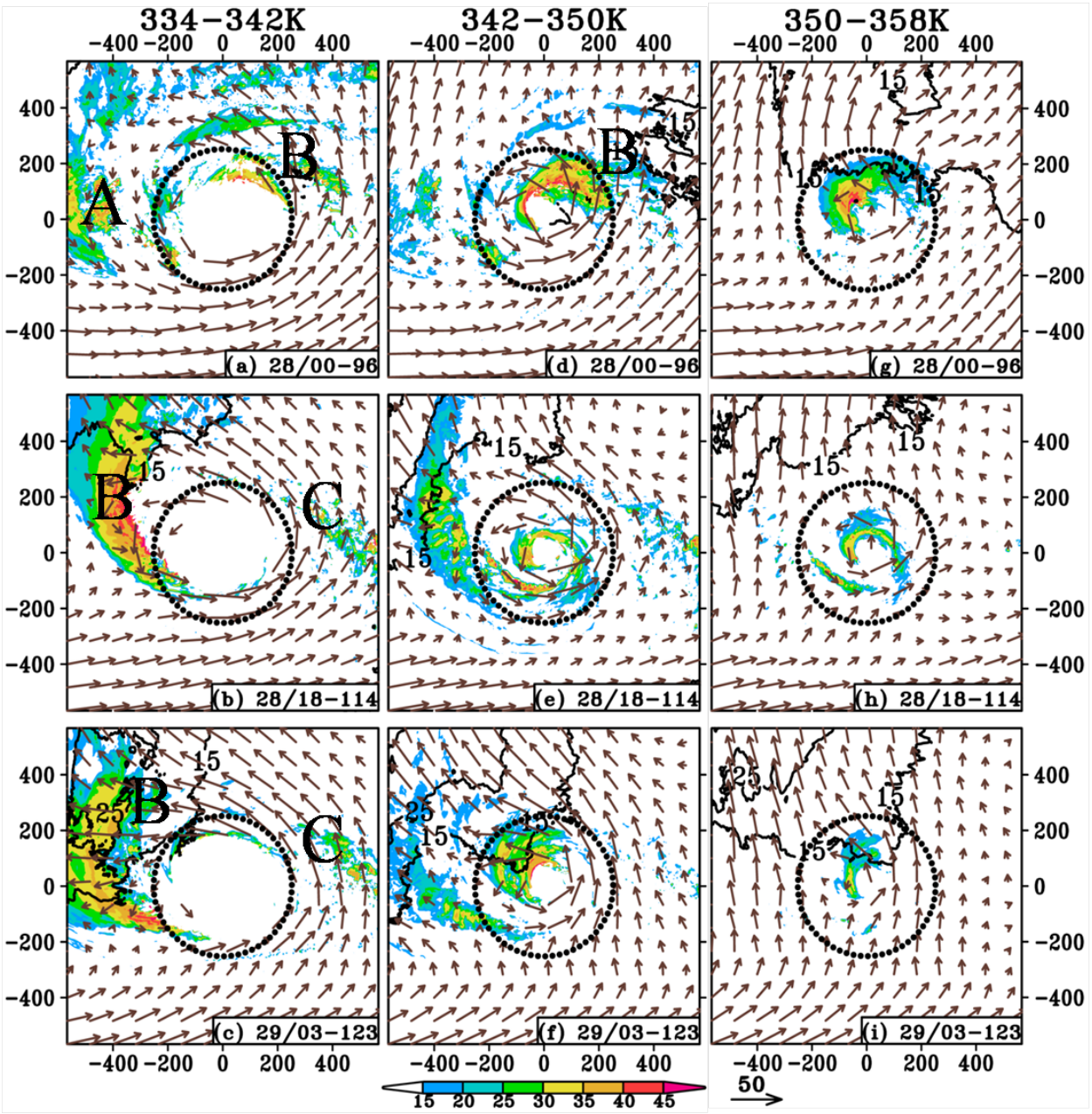

Figure 4.3. (a)-(c) Radar reflectivity (shaded, dBZ), horizontal wind vectors, and outward radial velocity (contoured at 15, and 25 m s^{-1}) vertically averaged over the equivalent potential temperature range (θ_e) 334-342K valid at 28/00-96, 28/18-114, and 29/03-123, respectively.(d) – (f) As in (a) – (c) but for θ_e range 342-350K. (g) – (i) As in (a) – (c) but for the θ_e range 350-358K. 250-km radius is indicated by dotted circle. Letters, "A", "B", and "D" indicate various frontal rainbands as described in the Fig. 3.1. Horizontal and vertical axes indicate the distance (km) from the TC vortex center. Data from the WRF 1.667-km resolution domain are used.

Figure 4.3 shows vertically averaged radar reflectivity (dBZ), wind vectors, and outward radial velocity in each layer (334 ~ 342K, 342 ~ 350K, and 350 ~ 358K) at different time levels. Radar reflectivity and outward radial velocity are plotted to indicate the location of deep convection and the outflow intensity, respectively. The vertical averaging is applied above 1.5 km to minimize the impact of the boundary layer inflow. Radar reflectivity and wind fields are not defined within 250-km radius in Figs. 4.3a-c, suggesting that the fields between 334-and 342-K levels (above 1.5 km) are not related to the core region.

At 28/00-96, between 334- and 342-K isentropes (Fig. 4.3a) the significant radar reflectivity signal which is related to the frontal rainband A, exists in the western quadrant. Figure 4.3d (between 342- and 350-K levels) shows that the significant radar reflectivity signals associated with the eyewall and the frontal rainband Bare located near the TC center. At this level there is some northward outflow which is caused by the frontal rainband B (Fig. 4.2e), but the outward radial velocity field (black contour) shows that this outflow is weak. In the top layer (350-358-K layer, Fig. 4.3g), the significant outflow mostly occurs in the north-northeast direction, where the outward radial velocity is greater than 15 m s^{-1}. Definitely, this outflow is dominant and related to the tall and strong eyewall convection around this time (Fig. 4.2e). As the frontal rainband B moves to the northwestern quadrant at 28/18-114, the convective signal mostly exists in the western semicircle region of the 334-342-K layer, not the 342-350-K layer (cf. Fig. 4.3b and 4.3d). In the northern semicircle region of this layer, the easterly wind blows toward the strong convection area associated with the frontal rainband B, causing a frontal lifting in this region, as

shown in Fig. 4.2b. The 342-350-K layer (Fig. 4.3e) shows the eyewall convection signal and weak north-northwestward outflow in the core region. In the 350-358-K layer, the direction of the outflow is almost north, but the distribution of the outward radial velocity indicates the intensity of the outflow weakens, as compared to that at 28/00-96. In summary, at 28/00-96 the 342-350-K and the 350-358-K layers are the outflow channel of the frontal rainband B and the eyewall convection, respectively. However, at 28/18-114 both layers become the outflow channels of the eyewall convection, while the outflow of the frontal rainband B is shifted to the 334-342-K layer from the original 342-350-K layer. By this time, the intensity of two outflow layers which are rooted in the eyewall convection, are not strong.

The time of 29/03-123 is an important moment during the re-intensification stage. In the 334-342-K layer (Fig. 4.3c) the easterly wind in the northern semicircle region enhances and blows toward the frontal rainband B. This easterly wind creates another outflow which has a slantwise convection feature, as shown in Fig. 4.2g. This pattern is consistent with Harr and Elsberry (2000) and Colle (2003), who found the slantwise convection in the frontogenesis region during extratropical transition (ET). They pointed out that the symmetric instability or neutrality in the low- to midlevel caused such slantwise ascent. Moreover, the outward radial velocity increases to 25 ms^{-1}, suggesting the enhancement of the frontal circulation. Again, the flow between 334 and 342K is not related to the eyewall convection. In the 342-350-K layer, there is a significant increase of the west-northwestward outflow, compared to that at 28/18-114 (cf. Figs. 4.3e and 4.3f). The strong convection or high dBZ values near the center, which is not detected in the 334-342-Klayer (Fig. 4.3c) is clearly captured

in the 342-350-Klayer. The distributions of the wind vector and the radar reflectivity of Fig. 4.3f show that *the direction of the outflow from the core convection is on the west-northwest or northwest*. The outflow direction of the 334-342-K and the 342-350-K layer is on the west and north-northwest, respectively, where the upper-level jet stream exists. On the contrary, the outflow in the 350-358-K layer heads north-northwest without a significant changes since 28/00-96. This suggests that the outflow above the 350-K level does not interact with the upper-level jet stream, while the outflow below 350K interacts with it, forming the large scale cirrus field as illustrated in Fig. 4.1. The most interesting feature is that during the re-intensification stage (29/03-123), the eyewall convection has two distinct outflow channels in the 342-350-K and the 350-358-K layers (Figs. 4.3f, 4.3i, and 4.2g). Among them the 342-350-K layer plays a dominant role during the re-intensification stage because it develops dramatically between 28/18-114 and 29/03-123 and forms the large scale outflow channel which is connected to the core region. The reason of unique dual outflow channels feature will be discussed further in chapter 4.5.

4.3. Physical characteristic at the vicinity of the outflow channel

This section discusses the descending motion above and on the side of the outflow channel by utilizing the inner most domain data. Figure 4.4a illustrates that the eyewall convection generates a strong outflow with the radial velocity exceeding 20 ms^{-1} below the tropopause near 300-km radius. Although the storm does not re-intensify until 28/00-96, it still possesses strong convection in the eyewall. But the strong outflow occurs locally because it accelerates between 150- and 300-km radii and decelerates beyond 300-km radius. Thus, the strong outflow region is limited

within 400-km radius. The cloud top is the highest near the center, and decreases with radius, as indicated by the 0.01-gkg^{-1} contour. This pattern is similar to the observational study of Kowacs and McCormik (2003), who shows that the cirrus cloud top height decreases with radius from the TC center. The radiative cooling layer prevails at the cloud top, and strong cooling exists locally above the high cloud concentration region, where the cloud mixing ratio is greater than 0.1 g kg^{-1}. The θ_e surface shows the upward bulge pattern above and near the tropopause, which is associated with the cold dome induced by deep convection in the eyewall (Fig. 4.4d). From the observational data Koteswaram (1967), and Waco (1970) verified the presence of an upper-level cold dome near the tropopause, or above deep convection of mature TCs. Due to the upward bulge of θ_e surfaces and the moderate outward flow pattern above the tropopause, there is a gentle descending motion above the tropopause and beyond 300-km radius. In addition, this region exists above the radiative cooling layer, which implies that the descending motion above the outflow layer and the tropopause is not closely related to the radiative cooling. This is consistent with Johnson et al. (1990), who argued that the downward motion can still occur near the tropopause without the radiative cooling, due likely to the deformation of isentropes.

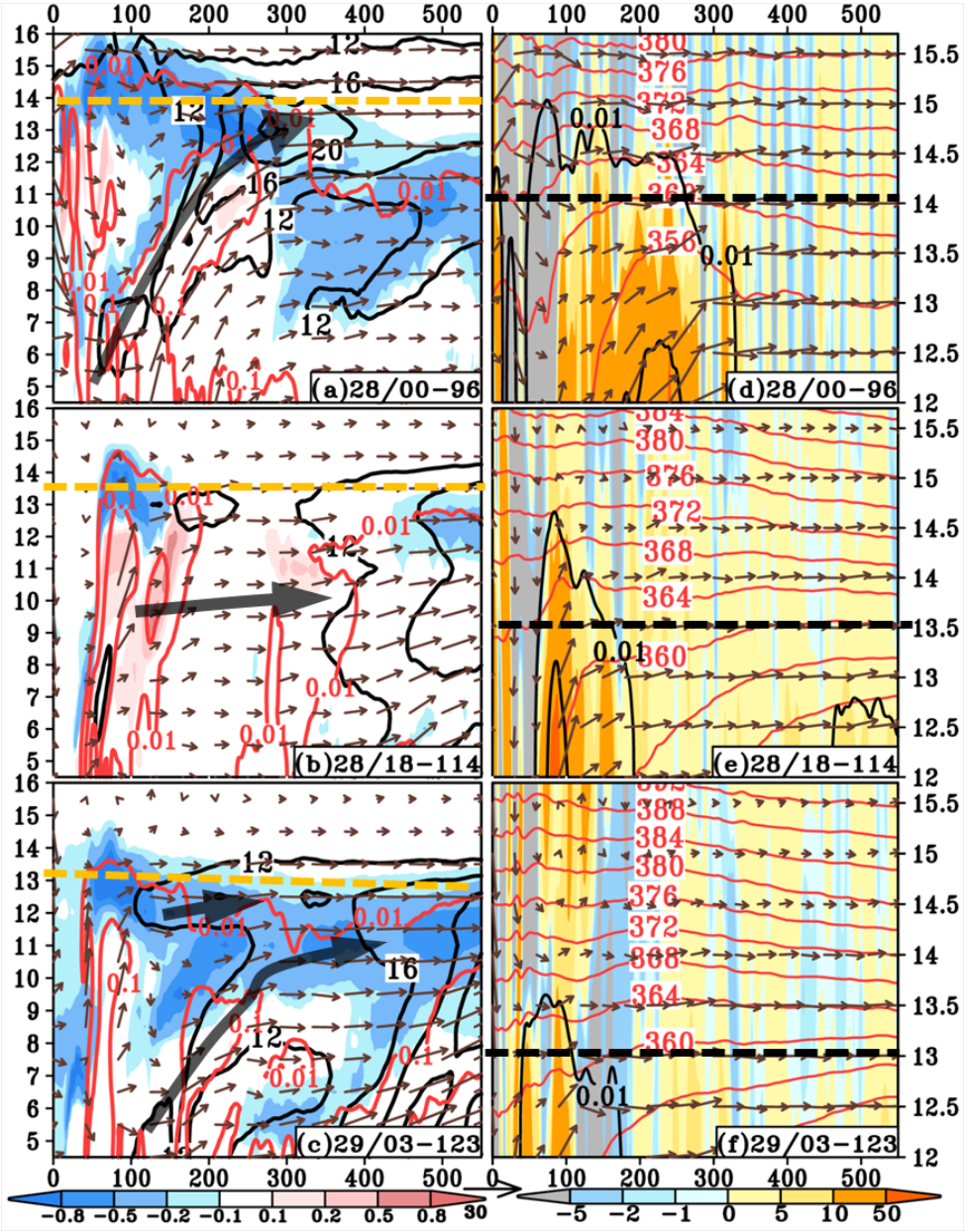

Figure 4.4. (a)-(c) Radial-height cross section of in-plane flow vectors, radiative heating rate (shaded, K h^{-1}), outward radial velocity (black-contoured at 4-m s^{-1} intervals above 12 m s^{-1}), and cloud mixing ratio (red-contoured at 0.01 and 0.1 g kg^{-1}). Thick gray arrow indicates outflows associated with eyewall convection. (d) – (f) As in (a) – (c) but vertical velocity (shaded, cm s^{-1}), equivalent potential temperature (θ_e, red-contoured at intervals of 4K), and cloud mixing ratio (black-contoured at 0.01 and 0.1 g kg^{-1}). Horizontal axis indicates the distance (km) from the TC vortex center. The tropopause height (defined in Fig. 3.3a) is denoted by orange dashed, and black dashed line. Fields are averaged between two azimuths, which are indicated in Figs. 4.3a-d. Data from the WRF 1.667-km resolution domain are used.

At 28/18-114, (Figs. 4.4b and 4.4e) the frontal rainband B and the eyewall convection are separated, as identified by the 0.01-g kg^{-1} contour. Only moderate and deep outflows associated with the eyewall exist, due to the relatively weaker convection in this period. The weaker convection may explain little significant upward bulge of isentropes, as shown in Fig. 4.4d. The extensive and strong radiative cooling layer almost disappears because the cloud top does not extend continuously, and the shortwave warming compensates some portion of the cooling effect during the daytime at 28/18 corresponding to 14:00 LST (Melhauser and Zhang 2014).

When Sandy re-intensifies at 29/03-123 (Fig. 4.4c), the cloud field and the strong radiative cooling layer expand again in response to the enhancement of the outward radial velocity. Consistent with Figs. 4.3f and 4.3i, the 12-m s^{-1} contour implies that two outflows develop (indicated as black arrows) associated with the eyewall. The shallow and horizontal outflow are located below the tropopause, while another significant and slantwise outflow develops at 200~300-km radius. It will be explained in chapters 4.4 and 4.5 that the latter is mostly located in the 342-350-K layer and also plays an important role in the re-intensification stage. In short, during the re-intensification the eyewall convection has two outflows, and one of them has slantwise pattern. The secondary strong outflow associated with the frontal rainband B is observed beyond 400-km radius and below 10 km. Right panel (Fig. 4.4f) shows that isentropes above the tropopause are tilted downward with radius, which results in a weak descending motion in this altitude. At this time, the eyewall convection is not

strong enough to deform isentropes above the tropopause, as shown in 28/00-96, it is the approaching trough that causes the deformation of isentrope.

Figures 4.4a and 4.4c show the following important features of the outflow; the outflow layer is usually present at the vicinity of the radiative cooling layer. The distribution of the cloud mixing ratio 0.01-, and 0.1-g kg^{-1} contours reveals that usually in the upper level, *the high cloud concentration layer is located beneath the level of maximum outward radial velocity (i.e., the core of the outflow layer).* Such vertical configuration is also supported by Molinari et al. (2014), who showed that the level of maximum relative humidity was present beneath that of the maximum radial outflow velocity (their Figs. 8 and 11). In other words, because the outflow channel is located just above the cloud top, it is affected by the radiative cooling. It also suggests that the subsidence above the outflow channel is not closely related to this diabatic process because the descending motion usually occurs where the radiative cooling does not exist. The impact of radiative cooling on the outflow layer will be discussed in chapter 4.6.

In Fig. 4.1b, we have shown that the descending motion prevails outside of the cloud field. The lateral mixing, which is observed at the cloud boundary, could induce subsidence through evaporative cooling (Rodts el al. 2003; Wang and Geerts 2010). To verify if a similar mechanism occurs at the edge of the outflow layer, we investigate the southwestern boundary of the frontal convection outflow (indicated as the two black dashed lines in Fig. 4.5a), where dry air blows toward the cloud boundary (Fig. 4.1b). Temporal averaging is applied to display some persistent features and remove gravity-wave-related noise.

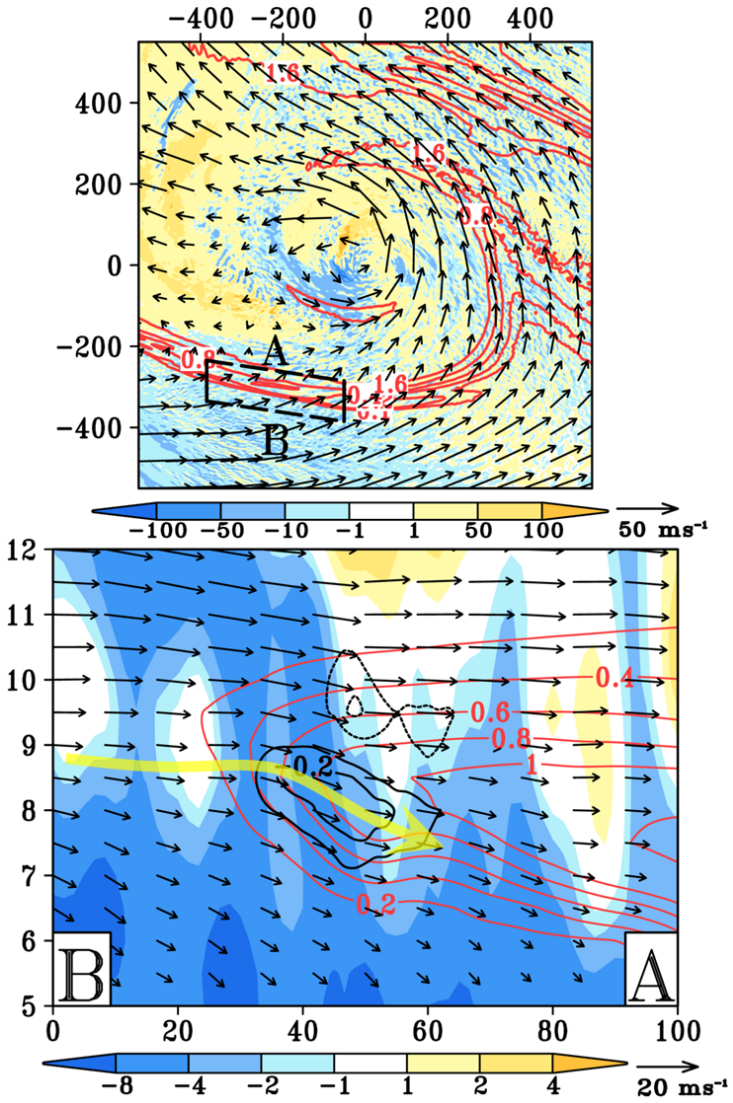

Figure 4.5. (a) Horizontal distribution of horizontal wind vectors, vertical velocity (shaded, cm s^{-1}), and total water content (red-contoured at 0.1, 0.2, 0.4, 0.8, and 1.6 g kg^{-1}) at z = 7 km at 29/03-123. Horizontal and vertical axes indicate the distance (km) from the TC vortex center. (b) Vertical cross section of wind vectors, vertical velocity (shaded, cm s^{-1}), total water content (red-contoured at 0.1, 0.2, 0.4, 0.8, and 1.6 g kg^{-1}), and diabatic heating rate (black-contoured at -0.2, -0.1, 0.1, and 0.2 K h^{-1}: solid/negative, dotted/positive) from the model cloud physics. Fields are zonally-averaged along A-B shown in (a). Yellow arrow indicates entrainment flow. Horizontal axis indicates the length of cross section in meridional direction. Total water contents are defined as the summation of water vapor, rain water, and cloud water. All fields are temporally averaged (±1 hour) with 1.667-km resolution data.

We can see from Fig. 4.5a that the subsidence area prevails in the southwestern quadrant, where the distinct boundary between moist cloudy and dry air (as shown by the strong total water content gradient) exists. Also the wind pattern reveals that dry air entrainment could occur in this area. Figure 4.5b illustrates that the evaporative cooling exists between 7 and 9 km, where the dry environment air interacts with the moist cloudy air. And between the two levels the local maximum of the descending motion occurs approximately near the evaporative cooling region. The flow pattern implies that some flow in the 8-9-km layer begins to descend at the cloud boundary, where the evaporative cooling occurs. Although some subsidence is found within the moist cloudy air, the descending motion greater than 4 cm s^{-1} is present outside of the 1-g kg^{-1} contour. In short, Fig. 4.5 shows that the evaporative cooling is present where dry environment air interacts with moist cloudy air, and it seems that there is a relationship between this cooling and the descending motion at the cloud boundary.

4.4. Inertial instability in the outer region

In chapter 4.2 we have shown that the 342-350-K outflow layer is dominant in the core region during the re-intensification process. Based on this result, the influence of dynamic instabilities (symmetric and inertial instability) in the 342-350-K outflow layer will be examined in this section. We have seen from Fig. 4.1 that the upper-level jet stream exists approximately 500~600 km from the TC center during the re-intensification stage. Therefore, it appears that the impact of inertial instability may be significant in the outer region (i.e., beyond 600-km radius) of the storm. Based on this observation, we will investigate the inertial instability in the outer region first, and then verify the symmetric instability in the inner region.

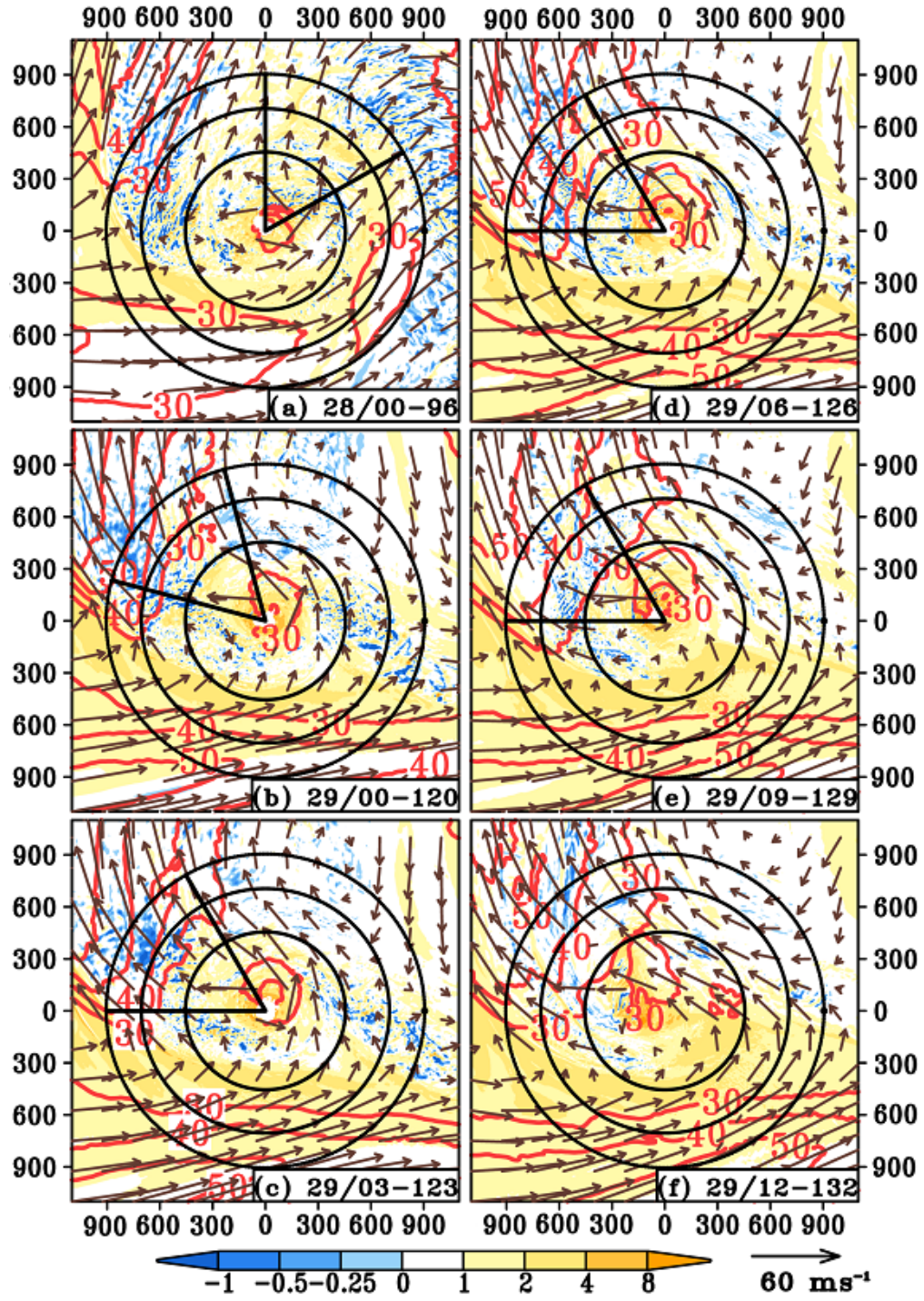

Figure 4.6. (a) – (f) The 342-350-K layer-averaged absolute vorticity (shaded, $\times 10^{-4}$ s^{-1}), isotach (contoured at 10-m s^{-1} intervals above 30 m s^{-1}), and horizontal wind vectors, valid at 28/00-96, 29/00-120, 29/03-123, 29/06-126, 29/09-129, and 29/12-132, respectively. The 450-, 700-, and 900-km radii are indicated as references. The two lines (through the center) in black indicate approximately the outflow region associated with the eyewall convection. Horizontal and vertical

axes denote the distance (km) from the TC vortex center. Data from the WRF 5-km resolution domain are used.

Figure 4.6 shows the evolution of the 342-350-K layer-averaged absolute vorticity and wind fields on 28 and 29 October. During the steady-V_{MAX} stage (Fig. 4.6a, 28/00-96) when the upper-level jet stream is located in the northwestern quadrant, the outflow of the frontal rainband B heads north; similarly for the direction of the 350-358-K outflow originated from the eyewall convection (Fig. 4.3g). This implies that none of the outflow channels are influenced by the upper-level jet stream. Negative absolute vorticity areas are detected on the right side of the jet stream entrance, where the anticyclonic shear is strong enough to generate inertial instability. We have checked the distribution of the composite radar reflectivity in the 5-km domain, and most convection associated with the frontal rainband or the eyewall exists within around 600-km radius. It confirms that the negative absolute vorticity beyond the 600-km radius is not caused by deep convection, but due to the anticyclonic shear of the upper-level jet stream. However, when Sandy re-intensifies around 29/00-120, the 342-350-K layer begins to act as the major outflow channel of the eyewall convection, which is directed west-northwestward or northwestward (Fig. 4.6b). This suggests that the outer region of the outflow channel becomes inertially unstable, providing a favorable condition for the outflow development. Besides, after 29/00-120 Sandy begins to move northwestward toward the upper-level jet stream, facilitating the interaction between the upper-level jet stream and the outflow channel. Until 29/09-129 (Figs. 4.6b-d), when significant re-intensification lasts, the outer region of Sandy's northwestern quadrant is generally inertially unstable. In short,

between 29/00-120 and 29/09-129 the outflow is exposed in the inertially unstable environment, due to the movement of the storm and the direction of outflow. However, around 29/09-129, it appears that negative absolute vorticity near the upper-level jet stream is significantly reduced (Fig. 4.6e). Such a pattern is also found during the decaying stage of the storm (29/12-132), as shown in Fig. 4.6f. An interesting feature in Fig. 4.6 is that the inertial instability at the vicinity of the upper-level jet stream begins to weaken when the re-intensification process is ended. The disappearance of the inertially unstable region is due to the retrograde motion of the upper-level trough/jet stream system on 29 October (not shown). The location of 40 and 50 m s^{-1} isotachs relative to the 700-km radius circle supports such a movement. Due to the westward movement of the upper-tropospheric jet stream, the interval between isotachs is not dense around on 29/09-129 and 29/12-132. In other words, the anticyclonic shear (i.e., negative relative vorticity) of the jet stream is not strong enough to compensate for positive planetary vorticity.

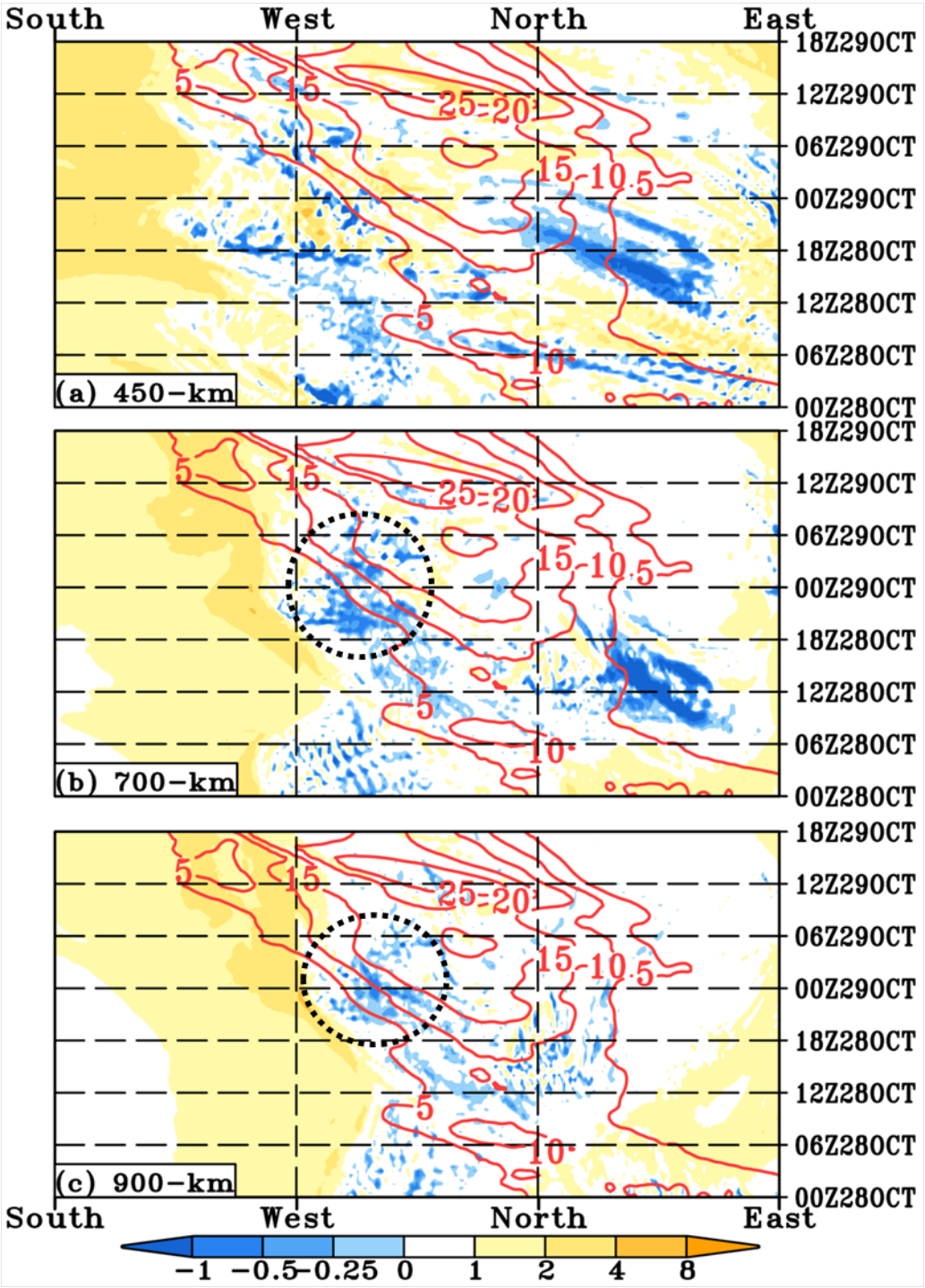

Figure 4.7. Time-azimuth distribution of the 342-350-K layer-averaged absolute vorticity (shaded, $\times 10^{-4}$ s^{-1}), which is ±25 km radially-averaged at (a) 450-, (b) 700-, and (c) 900-km radius, and the outward radial velocity (red-contoured at 5-m s^{-1} intervals) at 250-km radius. The black dotted circle indicates negative absolute vorticity due to the upper-level jet stream. Data from the WRF 5-km resolution domain are used.

To find a clear relationship between the outflow near the core region and the environmental inertial instability, the time-azimuth distributions of 342-350-K layer-averaged environmental absolute vorticity and outward radial velocity are plotted in Fig. 4.7. We assume that the upper-level inertial instability at the outer region may cause the acceleration of the outflow near the core region. Based on this assumption, the radial velocity at 250-km radius is carefully chosen as the outflow of the core region because the eyewall convection mostly exists within this radius, as illustrated in Fig. 4.3, whereas the absolute vorticity at 450-, 700-, and 900-km radii represent the environmental inertial instability. At a glance, Fig. 4.7 illustrates that the outflow of the 342-350-K layer slowly propagates from the northeastern to northwestern quadrant, as shown in Figs. 4.2 and 4.3. As a result, between 28/00-96 and 28/18-114 when Sandy does not intensify, the outflow in the northeastern quadrant reduces, but it increases slowly in the northwestern quadrant. From 28/15-111 to 28/21-117, there is some increase in radial velocity from 5 to 15 m s^{-1} in the north-northwest direction, but it is related to the temporal increase of the eyewall convection, as will be shown in Fig. 4.11, rather than the environmental inertial instability. After 28/21-117, red contours in Fig. 4.7 show a noticeable increase of the outward radial velocity in the west-northwest direction, where inertial instability associated with the upper-level jet stream exists beyond the 600-km radius. This pattern suggests that as the outflow channel propagates to the northwestern quadrant, strong acceleration of the outflow occurs in the west-northwest direction. However, after 29/06-126, the increase of the outward radial velocity in the west-northwest direction ceases when the negative

absolute vorticity at 700- and, 900-km radii almost disappears (Figs. 4.7b and 4.7c). This disappearance of the negative absolute vorticity is also found in Fig. 4.6. The correlation between the negative absolute vorticity in the outer region and the strong acceleration of outflow in the core region implies that the outflow develops when the outer region is inertially unstable. However, Fig. 4.7a shows no such clear relationship between the negative absolute vorticity at the inner core (450-km radius) and the outflow. Also, there is another negative absolute vorticity region in the northeastern quadrant, but it is associated with the anticyclonic curvature of the outflow itself, not caused by the upper-level jet stream or any type of environmental disturbance (not shown).

4.5. Symmetric instability in the inner region

While Figs. 4.6 and 4.7 illustrate the horizontal view of the outflow structure with more focus on the outer region, the following part will discuss the symmetric instability of the inner core outflow. Height-radial cross sections of the outflow structures within the 600-km radius are displayed between the early stage of re-intensification (28/18-114) and the second intensity peak (29/09-129) in Fig. 4.8. Fields in Figs. 4.8, 4.9, and, 4.10 are averaged between two azimuths, as indicated in Figs. 4.3 and 4.6, and represent the rough outflow region of the core convection. In the early stage of re-intensification, i.e., at 28/18-114 (Fig. 4.8a), deep and weak tropospheirc outflow (~5 m s^{-1}) from the center exists above 5 km. The strong outward velocity beyond 400-km radius is associated with the frontal rainband B, rather than the core convection. When re-intensification is underway, the slantwise outflow intensifies from 12 to 20 m s^{-1} between 29/03-123 and 29/06-126 (Figs. 4.8b

and 4.8c) approximately at 250-km radius. Another important feature is the depth and extent of the anticyclonic tangential wind associated with the approaching upper-level jet stream during the re-intensification process. When Sandy re-intensifies between 28/18-114 and 29/06-126, the negative tangential wind area expands downward significantly between 150- and 550-km radii. This pattern is caused by the northwestward movement of the storm when it approaches to the upper-level jet stream. By the time the storm reaches the second intensity peak, it still exhibits the slantwise convection as noted in Fig. 4.2h. The extent of the upper-level anticyclonic tangential wind reduces noticeably between 29/06-126 and 29/09-129 (cf. Figs. 4.8c and 4.8d). As noted in chapter 4.4, the retrogration of the upper-level jet stream/trough explains the contraction of anticyclonic tangential wind area. The occurrence of the slantwise ascent beyond 100-km radius, which is a unique feature of Sandy, is due to a large size (~150 km) of the eyewall convection (Fig. 3.1f). Besides, this outflow feature strongly suggests the presence of the symmetric instability in the outflow layer within 600-km radius.

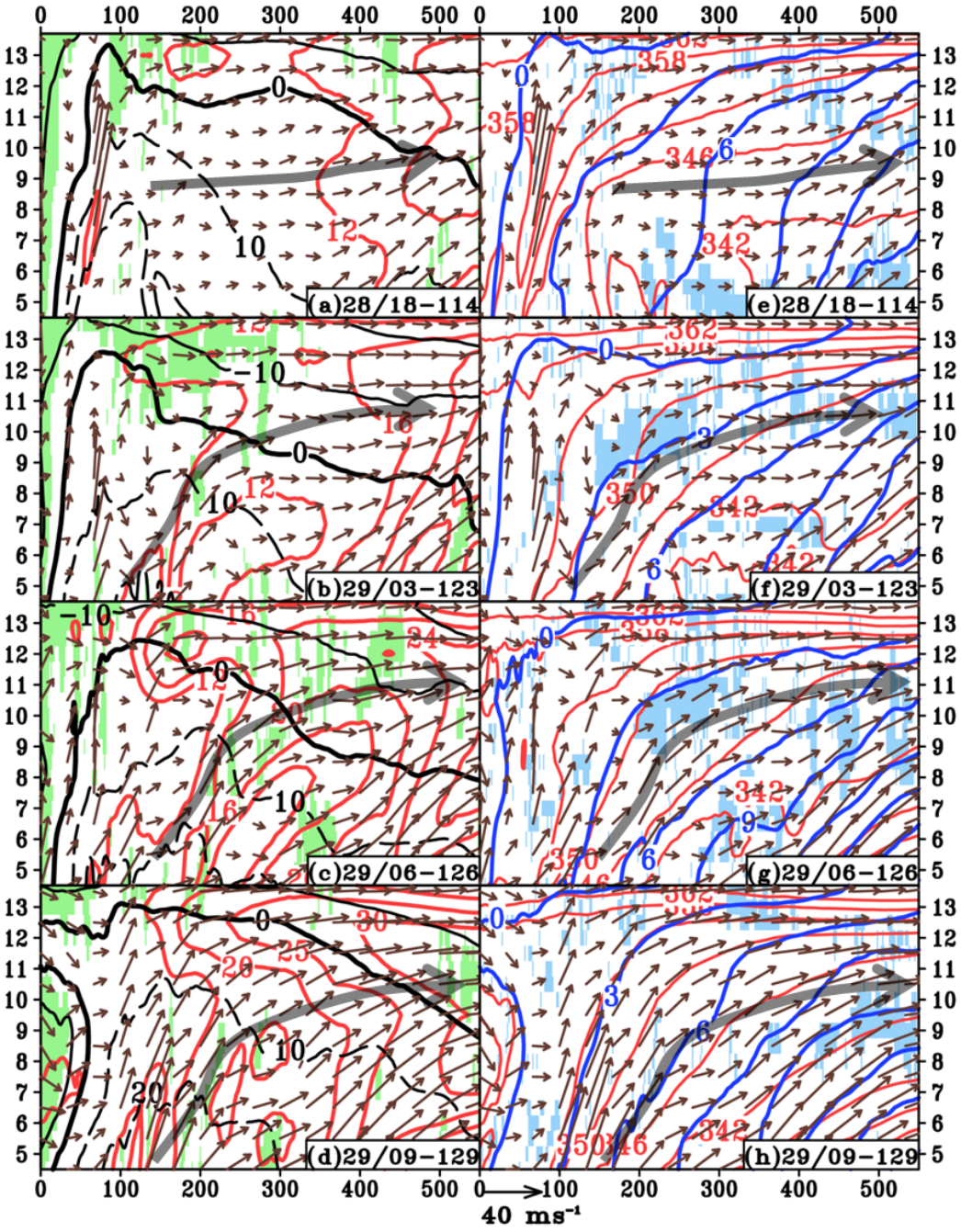

Figure 4.8. (a)-(d) Radial-height cross section of wind vectors, tangential wind (black-contoured at 10-m s^{-1} intervals), and outward radial velocity (red-contoured at 4-m s^{-1} intervals above 12 m s^{-1}, but at 5-m s^{-1} intervals for Fig. 4d), valid at 28/18-114, 29/03-123, 29/06-126, and 29/09-129, respectively. Green shaded region indicates where absolute vorticity is negative. (e) – (h) As in (a) – (d) but for equivalent potential temperature (θ_e, red-contoured at intervals of 4K), and AAM (blue-contoured at intervals of 3×10^6 m^2 s^{-1}). Blue shaded region indicates where moist Richardson number is between 0 and 1. Thick gray arrow indicates the outflow between 342- and 350-K isentropes. Horizontal axis

indicates the distance (km) from the TC vortex center. Fields are averaged between two azimuths, which are indicated in Figs.4.3a-d and Fig. 4.6. Data from the WRF 1.667-km resolution domain are used.

Since the analyses of isentropes (for θ_e) and absolute angular momentum (AAM) are useful diagnostic tools to study the symmetric neutrality or instability in the core region of TCs (Zhang et al. 2000; Molinari and Vollaro 2014), their distributions will be investigated in this section. However, an additional parameter moist-Richardson number (Ri_m) is utilized to study the location of symmetrically unstable layer (Seltzer et al. 1985; Reuter and Yau 1990). It is given by

$$Ri_m = \frac{\left(\overline{f} + \frac{1}{r}\frac{\partial r\overline{V}}{\partial r}\right)}{\overline{f}} \frac{\Gamma_m}{\Gamma_d} \frac{g}{\overline{\theta_e}} \frac{\frac{\partial \overline{\theta_e}}{\partial z}}{\left(\frac{\partial \overline{V}}{\partial z}\right)^2} \quad (4.1)$$

where V is the tangential wind, g is the gravitational acceleration, $\left(\overline{f} + \frac{1}{r}\frac{\partial r\overline{V}}{\partial r}\right) \Big/ \overline{f}$ is the inertial stability (or absolute vorticity) term; $\frac{\partial \overline{\theta_e}}{\partial z}$ is the static stability term; $1 \Big/ \left(\frac{\partial \overline{V}}{\partial z}\right)^2$ is the vertical shear term; Γ_m / Γ_d is the ratio between dry lapse rate and moist lapse rate. Here overbar indicates that fields are averaged between two azimuths denoted in Figs. 4.2 and 4.6. Γ_m / Γ_d is also calculated from the Eq. 19 of Durran and Klemp (1982) by using the averaged fields. If Ri_m is between 0 and 1, the atmosphere is in symmetric unstable condition. This implies that even though the outflow layer is inertially stable (i.e., absolute vorticity > 0), if the static stability is reduced by strong radiative cooling, the outflow layer can become symmetrically

unstable. Since Molinari et al. (2014) shows that the radiative cooling can reduce the static stability of the outflow layer from dropsonde data, we are going to examine whether such cooling can also reduce Ri_m below 1.

At 28/18-114, the orientation of AAM surfaces are vertical below 9 km, and steeper than that of θ_e surfaces in most of the region, except above 9 km and beyond 400-km radius (Fig. 4.8e). Ri_m falls below 1 in this region, as indicated by blue shadings, where isentropic surfaces are slightly steeper than AAM surfaces, suggesting that the use of Ri_m is consistent with the graphical relationship between AAM and θ_e surfaces. However, Figs. 4.8f and 4.8g show that by 29/03-123 and 29/06-126, *AAM surfaces (e.g., values with* 3×10^6, and 6×10^6 m^2 s^{-1}) *are significantly tilted outward above 6 km*. Thus, the slopes of isentropes are steeper than those of AAM surfaces in a large portion. Simultaneously, blue shaded areas emerge above 8 km, where inertial instability (green shaded) is not significant. Although there are some layers where the absolute vorticity is less than 0, it appears that this local inertial instability is not generated by the upper-tropospheric jet stream, but by changes in the sign of tangential winds outside of the TC vortex. This result suggests the increase of symmetric instability in the upper troposphere. The reason of outward tilting of AAM surfaces can be found in Figs. 4.8b and 4.8c. As Sandy approaches the upper-level jet stream with the anticyclonic wind at 29/03-123 and 29/06-126, AAM decreases in the upper troposphere. In other words, it is the upper-level jet stream that causes the outward tilting of AAM surfaces and symmetric instability. The change of AAM surfaces is consistent with the merging of frontogenesis region and eyewall convections, as noted in Chapter 3. According to the thermal wind balance, the upper-

level jet stream appears above a cold frontal zone to the west. As Sandy moves toward the upper troposphric jet stream, where the baroclinicity is large, the tilting of AAM surfaces increases to reflect such a baroclinic structure. Such tilted absolute momentum surfaces were also observed in the ET case of Hurricane Floyd (Atallah and Bosart 2003). The slantwise outflow, which can be identified from 12 and 16 m s^{-1} contours (or gray arrows) in Figs. 4.8b and 4.8c, occurs where AAM slopes are gentler than θ_e slopes or Ri_m is less than 1. However, the slope of AAM contours at the second intensity peak is much steeper than that at 29/03-123 and 29/06-126, due to the weakening of anticyclonic wind (Figs. 4.8d and 4.8h). As a result, AAM surfaces are generally steeper than θ_e surfaces within 400-km radius, suggesting the weakening of symmetric instability. Blue shaded area is also reduced significantly, except beyond 400 km radius, where the slope of θ_e surfaces is still steeper than that of AAM surfaces.

To examine the symmetric instability within the outflow layer between 28 and 29 October, the evolution of AAM along the θ_e surfaces is plotted as illustrated in Fig. 4.9.

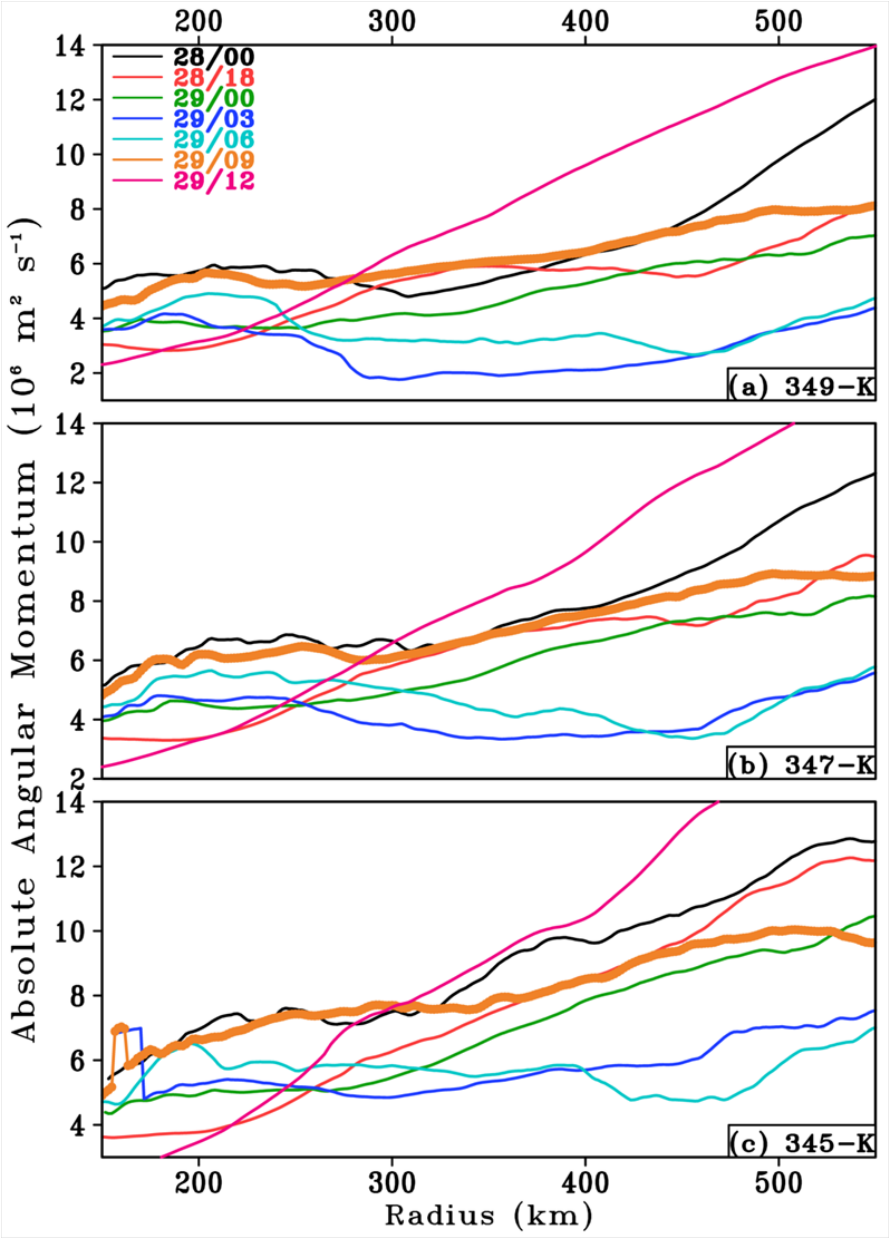

Figure 4.9. Time evolution of AAM (10^6 m^2 s^{-1}) on (a) 349-K, (b) 347-K, and (c) 345-K isentropic (θ_e) surface. Horizontal axis indicates the distance (km) from the TC vortex center. Fields are averaged between two azimuths, which are indicated in Figs. 4.3a-d and 4.6. Data from the WRF 1.667-km resolution domain are used. Significant re-intensification occurs at 29/00-120, 29/03-123, and 29/06-126 (cold colored lines). Secondary intensity peak time (29/09-129) is indicated by thicker line.

The AAM field is vertically interpolated into 345-, 347-, and 349-K isentropic surfaces based on AAM and θ_e fields, which are averaged between two azimuths, as

indicated in Figs. 4.2 and 4.6. The 345-, 347-, and 349-K isentropic surfaces are chosen because the 342-350-K layer plays an important role in the re-intensification stage. When the outflow channel heads northeastward at 28/00-96, AAM increases outward with radius along isentropic surfaces (the black line in Fig. 4.9). However, as the outflow channel changes from northeast to northwest between 28/00-96 and 29/00-120, the AAM beyond 250-km radius reduces, and this tendency is very prominent in the outer region (see black, red, green lines in Fig. 4.9). As shown in Fig. 4.7, the outflow channel moves to the northwestern quadrant, where the upper-level jet stream reduces AAM after 28 October, and this movement decreases the AAM beyond 250-km radius of the outflow channel region. At 29/03-123 and 29/06-126 when the storm approaches to the upper-level jet stream, the AAM along isentropic surface reduces further (see blue and dark blue line in Fig. 4.9). This reveals the presence of symmetric instability (or neutrality) in the outflow layer when a significant re-intensification is underway between 29/00-120 and 29/09-129. Figure 4.9 shows further that symmetric instability (or neutrality) is more prominent in the upper portion of the 342-350-K layer (i.e., on 347- and, 349-K isentropic surfaces). When Sandy reaches its second intensity peak at 29/09-129 (thick orange line in Fig. 4.9), the AAM beyond 250-km radius increases again, so it appears that it already begins to increase between 29/06-126 and 29/09-129. At 29/12-132, the outflow becomes symmetrically stable since AAM increases significantly. Again, the increase of the AAM beyond 250-km radius is caused by the weakening of anticyclonic flows. In short, Figs. 4.8 and 4.9 indicate that the 342-350-K outflow layer is generally symmetrically unstable when Sandy re-intensifies, but it already becomes stable again

by the time the storm reaches the second intensity peak. Combining with the results from inertial instability (Figs. 4.6 and 4.7), the *outer and inner region are inertially and symmetrically unstable, respectively between 29/00-120 and 29/09-129 during the re-intensification stage. The upper-tropospheric jet stream contributes to the formation of i) inertial instability in the outer region via the generation of negative absolute vorticity, and ii) symmetrical instability in the inner region via the outward tilting of AAM surfaces.*

Compared to the results from Molinari and Vollaro (2014) it appears that AAM surfaces are more tilted outward when Sandy re-intensifies, which is more favorable for the formation of symmetric instability. Unlike their results the AAM distribution of Sandy suggests the presence of the upper-level jet stream can tilt AAM surfaces outward, generating symmetric instability.

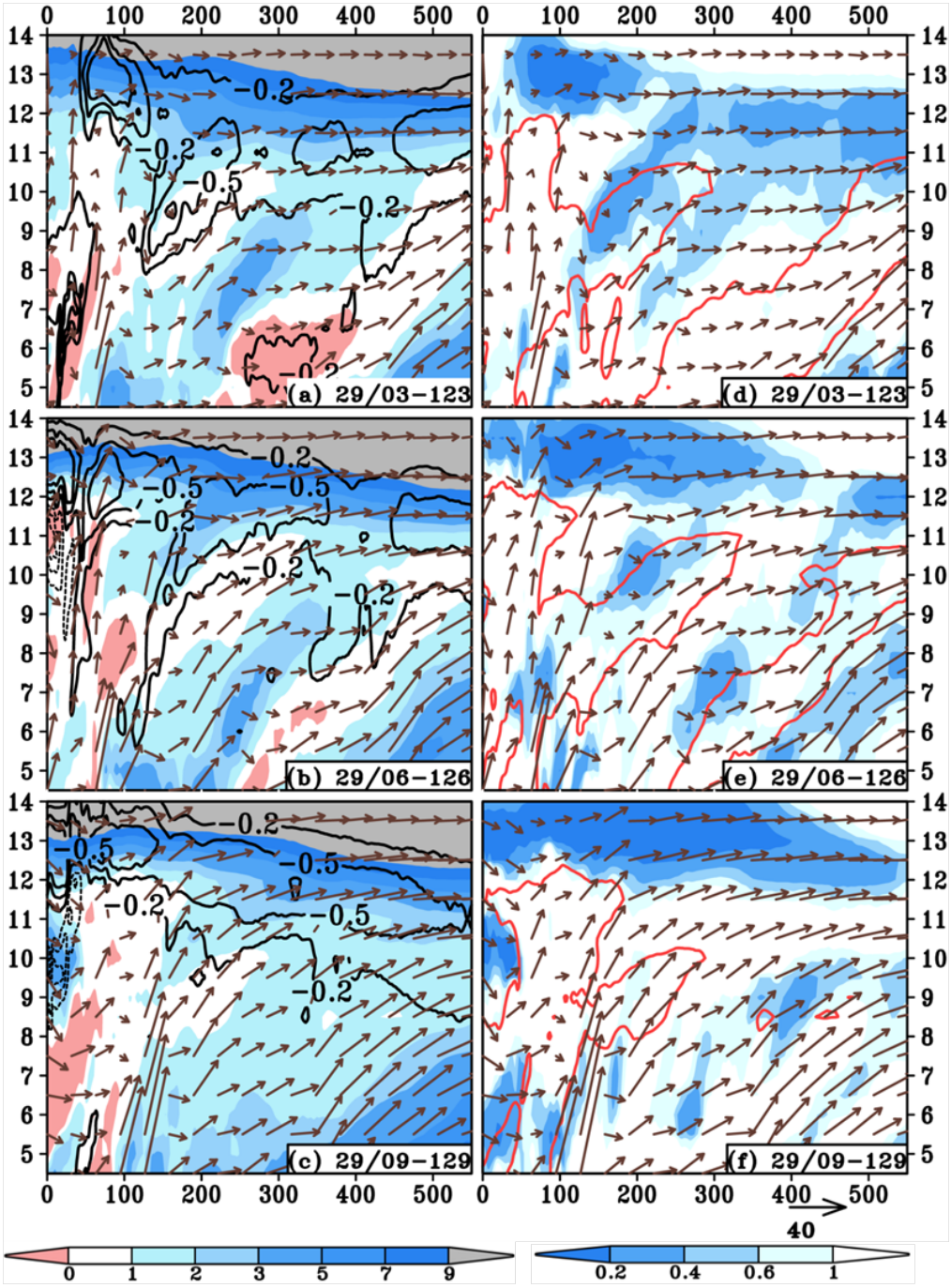

Figure 4.10. (a)-(c) Radial-height cross section of wind vectors, radiative heating rate (black-contoured at -0.8, -0.5, -0.2, 0.2, 0.5, and 0.8K h^{-1}: solid/negative, dotted/positive) from model output, vertical stability (shaded, K km^{-1}) , valid at 29/03-123, 29/06-126, and 29/09-129, respectively. (d) – (f) As in (a) – (c) but for vertical shear term (shaded, 10^{-5}), and vertical stability (red-contoured at 1K km^{-1}). Horizontal axis indicates the distance (km) from the TC vortex center. Fields are averaged between two azimuths, which are indicated in Figs.4.3a-d and 4.6. Data from the WRF 1.667-km resolution domain are used.

4.6. The roles of radiative forcing in symmetric instability

The right panel of Fig. 4.8 also implies the impact of the radiative cooling on the symmetric instability of the outflow layer. At 29/03-123 and 29/06-126, although the region, where Ri_m is below 1 (blue shading), prevails between 342- and 350-K isentropes, there are two noticeable regions in the 9-11-km layer; near 250-, and 500-km radii (Figs. 4.8f and g). Compare to the status at 28/18-114 (Fig. 4.8e) in those regions the interval between isentropes is large or with steep isentropes, suggesting low static stability. Especially at 250-km radius where blue shading area is large, the slope of isentropes increases between 28/18-114 and 29/06-126. This change of θ_e surfaces supports the significant decrease of the static stability during this period due to diabatic processes.

To examine the role of the radiative cooling in symmetric instability (or Ri_m), the radiative heating ($\overline{D\theta/Dt}$), the static stability ($\partial\overline{\theta_e}/\partial z$) and the vertical shear ($\left(\partial\overline{V}/\partial z\right)^{-2}$) terms are plotted in Fig. 4.10. Between 29/03-123 and 29/06-126, we can see the low static stability region is developing beneath the strong local radiative cooling layer, which is indicated by -0.5-K h^{-1} contour (Fig. 4.10a and b) near 250-km radius and within the 9-11-km layer. Similar feature is also found near 500-km radius at the same level. Such vertical configuration verifies that strong local radiative cooling at the cloud top reduces the static stability in the upper level. Besides, low Ri_m is frequently observed in the low static stability layer (Figs. 4.8f and 4.8g), and Figs. 4.10d and 4.10e show the location of minimum vertical shear term is somewhat

deviated from the low Ri_m region. *The coincidence of low static stability and low Ri_m area implies that a strong local radiative cooling has more significant influence on the formation of symmetric instability than vertical wind shear effect in the outflow layer.* Although this mechanism is different from that of Molinari and Vollaro (2014), who hypothesized that the long-wave warming within (and the cooling outside of) the cirrus overcast can cause symmetric instability by increasing the slope of θ_e surfaces in the upper-level outflow channel, *it appears that radiative cooling has an impact on the dynamic instability of the outflow layer*. By 29/09-129, the low static stability layer almost disappears when the symmetric instability area (where $Ri_m < 1$) is almost gone (Fig. 4.10c). At this time, the symmetric instability area near 500-km radius and in the 9-11-km layer is caused by the vertical shear term. In summary, even though it is the upper tropospheric jet stream that causes symmetric instability by tilting AAM surfaces outward, the long-wave cooling also plays some role in creating symmetric instability by changing the static stability. Especially, near 250-km radius the long-wave cooling makes the slope of isentropes steeper than that of AAM surfaces.

4.7. The impact of dynamic instabilities on the storm re-intensification

In the previous sections, we verify that (i) the outer (inner) region of the 342-350-K outflow layer is inertially (symmetrically) unstable between 29/00-120 and 29/09-129, and (ii) those dynamic instabilities disappear around 29/09-129 (i.e., the second intensity peak). These results suggest that the outflow layer could be well developed during this period, enhancing the secondary circulation of the storm. To examine the development of the secondary circulation, area-integrated vertical (F_{5km}

), vertically-integrated outward ($F_{OUTWARD}$), and vertically-integrated inward mass fluxes (F_{INWARD}) are calculated with the following methodologies, where w is the vertical velocity, V_r is the radial wind velocity and ρ is the density.

$$F_{5km} = \int_{0km}^{250km} \int_{0}^{2\pi} \rho w r d\theta dr, \quad F_{OUTWARD} = \int_{5km}^{13.5km} \int \rho V_r r d\theta dz, \quad F_{INWARD} = \int_{0km}^{1km} \int_{0}^{2\pi} \rho V_r r d\theta dz$$

The area-integrated mass flux at 5-km level (F_{5km}) is calculated within 250-km radius because, as shown in Fig. 4.3, 250-km radius covers the core convection properly. For the same reason, the vertically-integrated outward mass flux ($F_{OUTWARD}$) at 250-km radius is plotted. $F_{OUTWARD}$ is integrated from 5 to 13.5 km since 13.5 km is the approximated tropopause height on 28 and 29 October (see Fig. 3.3). To examine the contribution of the 342-350-K layer, which is closely related to the eyewall convection, F_{5km} is recalculated or integrated only over different θ_e ranges 334~342K (green line), 342~350K (red line), and 350~358K (blue line), as shown in Fig. 4.11a. The time series of F_{5km} shows two peaks of convection activity at 28/06-102 and 29/09-129, and its pattern is similar to the red line, suggesting the total vertical mass flux in the eyewall is dominated by the mass flux in the range 342~350 K. Total $F_{OUTWARD}$ (the blue line in Fig. 4.11b) includes the outward mass flux in the northern semicircle region because the outflow is directed northeastward or northwestward after 28/00-96. Between 28/00-96 and 28/12-108 the pattern of total $F_{OUTWARD}$ is similar to that of $F_{OUTWARD}$ in the northeastern quadrant, however, after 28/12-108 it is mostly determined by the $F_{OUTWARD}$ in the northwestern quadrant. This pattern is caused by the change of the outflow direction (from the northeastern to

northwestern quadrant) and also implies that during the re-intensification stage, $F_{OUTWARD}$ in the northwestern quadrant is closely related to this process. For this reason, we are going to focus on the $F_{OUTWARD}$ in the northwestern quadrant. Again, in Fig. 4.11b, $F_{OUTWARD}$ in the northwestern quadrant is integrated only over the θ_e range of 342~350 K (red line: $F_{OUTWARD}^{342-350K}$); although $F_{OUTWARD}^{342-350K}$ increases later than total $F_{OUTWARD}$ in the same quadrant, it increases rapidly during the re-intensification stage. For F_{INWARD}, the calculation is performed from 0 to 1 km and, the integration over different θ_e ranges is not calculated. Since the boundary layer inflow is not stratified like the outflow layer, it is unnecessary to differentiate F_{INWARD} based on the range of θ_e. In Fig. 4.11c, the F_{INWARD} at different radii are examined, and it increases rapidly after 29/00-120 at the outside of 250-km radius (blue and green lines).

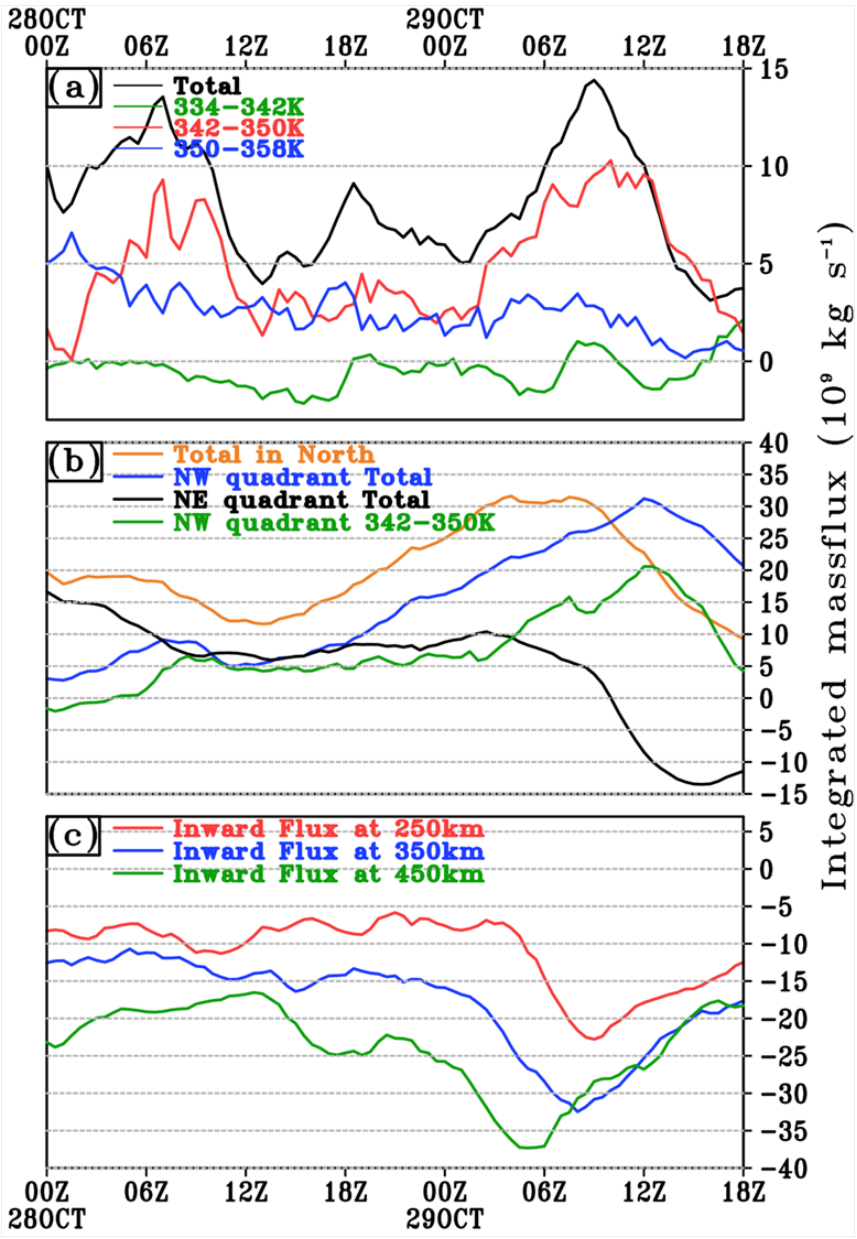

Figure 4.11. (a) Time series of total area-integrated vertical mass flux (black, F_{5km}), area-integrated vertical mass flux over different equivalent potential temperature ranges; 334-342K (green), 342-350K (red), and 350-358K (blue). Area-integration is performed within 250-km radius at 5-km level. (b) Time series of vertically-integrated total radial mass flux (orange/northern semi-circle region, blue/northwestern quadrant, black/northeastern quadrant), radial mass flux over equivalent potential temperature range 342-350K (green, $F_{OUTWARD}^{342-350K}$). Vertical integration is performed within 5-13.5 km layer. Radial mass flux at 250-km radius is plotted. (c) Time series of vertically-integrated total radial mass flux (F_{INWARD}) at 250- (red), 350- (blue), and 450-km (green) radii in the boundary layer (0-1 km); Unit: kg s^{-1}. Data from the WRF 1.667-km resolution domain are used.

Figure 4.11 reveals that Sandy's secondary circulation intensifies significantly between 29/00-120 and 29/09-129. Note that there are even large and small increases of total F_{5km} at 28/06-102 and 28/18-114, respectively, $F_{OUTWARD}$ does not show significant increases in the northeastern and the northwestern quadrants. In addition, little increases in F_{INWARD} occur at the two times, which is consistent with the near steady intensity of Sandy's secondary circulation. Only until 29/02-122, total F_{5km}, $F_{OUTWARD}^{342-350K}$, and F_{5km} of the 342~350K range begin to increase significantly, similarly for F_{INWARD}.The increase of the convective activity and outflow associated with the eyewall (i.e., within the 342-350K range) are closely connected to the enhanced boundary layer inflow. This pattern is consistent with that in Fig. 4.7, showing that the upper-level outward radial velocity from the eyewall convection begins to accelerate by 28/21-117 in the northwestern quadrant. Such a relationship verifies that the intensification of the secondary circulation associated with the eyewall (in-up-out flow pattern) occurs on 29 October. Total F_{5km}, $F_{OUTWARD}^{342-350K}$ in the northwestern quadrant, and F_{INWARD} increase until around 29/09-129. Since chapters 4.4 and 4.5 describe that both the outer and the inner regions of the outflow channel are dynamically unstable between 29/00-120 and 29/09-129, there is a high possibility that such instabilities can accelerate the outward motion at the upper levels, enhancing the secondary circulation. The large amount of total $F_{OUTWARD}$, and $F_{OUTWARD}^{342-350K}$ near 29/12-132 suggests that the outflow is strong during the re-

intensification period. To verify whether or not the enhanced secondary circulation by the strong outflow channel intensifies the storm, it is required to check other factors that can intensify the storm; such as the decrease of vertical wind shear (VWS), and the increase of [1]convective available potential energy (CAPE). Since Chapter 3 has shown that VWS increases from 9 to 21 m s^{-1} during the re-intensification stage due to the approaching jet stream, it is necessary to examine only the change of CAPE between 28 and 29 October. At a glance, Fig. 4.12 shows that CAPE decreases steadily after 28 October because of the intrusion of cold-dry air in the low levels. On 28 October, i.e., prior to the onset of Sandy's re-intensification, CAPE in the core region, as denoted by dotted circle, has a range from 200 to 1000 J kg^{-1}, which is enough to induce deep convection. Judging from the distribution of 340-K θ_e contour and the axis of the Gulf Stream, it appears that CAPE is highly influenced by the low-level θ_e since high CAPE (greater than 400 J kg^{-1}) generally exists where θ_e is larger than 340K. However, at 29/00-120, the size of area, where CAPE is greater than 400 J kg^{-1}, shrinks rapidly as the cold-dry air intrudes into the core region. Then, during the next 9 hours *when Sandy undergoes re-intensification, CAPE continues to decrease; it suggests that buoyancy does not increase during this period* (Figs. 4.12c-f). In other words, the intensification of the secondary circulation is not induced by buoyancy, but it could be driven by the enhancement of the outflow channel. As shown in Figs. 4.7 and 4.10, by the time (i.e., 29/09-129) inertial and symmetric instability are removed at the upper-levels, vertical, outward, and inward mass flux stop increasing or begin to decrease, even though the simulated storm does not make

[1] In here CAPE indicates the maximum CAPE which is calculated from the ARWpost. The ARWpost estimates maximum CAPE for the air parcel which has maximum equivalent potential temperature in the certain column.

landfall yet. It suggests that not only the beginning, but also the end of re-intensification is determined by the presence of the upper-tropospheric dynamic instabilities. This pattern is similar to that of Morinali and Vollaro (2014), who suggested that the intensification period of TCs may be determined by the removal of the upper-level dynamic instabilities.

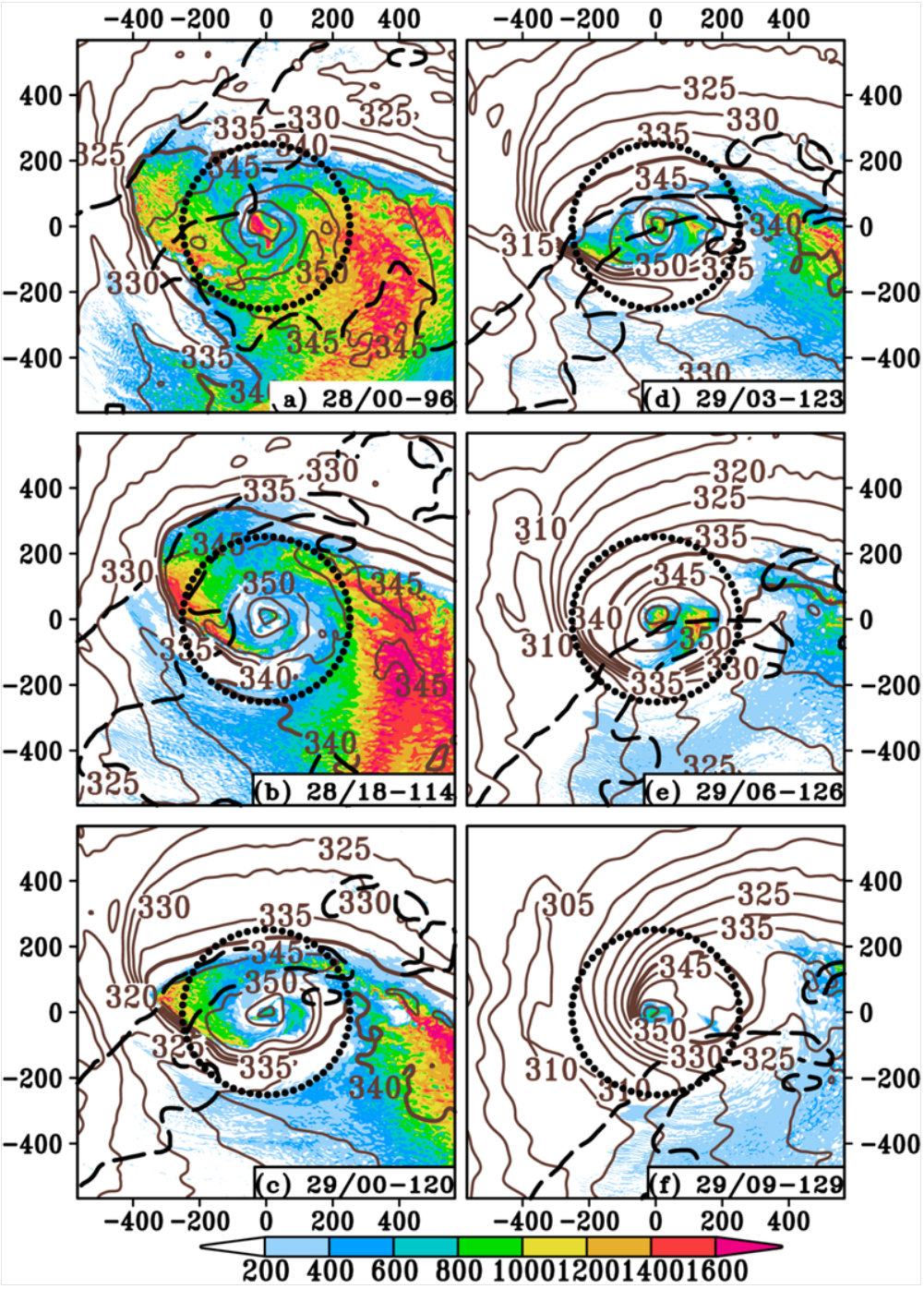

Figure 4.12. Horizontal distribution of maximum CAPE (shaded, J kg^{-1}), 1-km equivalent potential temperature (θ_e, brown-contoured at interval of 10K with θ_e= 340K highlighted), and SST (black dashed contoured at 26.5C°) at (a) 28/00-96, (b) 28/18-114, (c) 29/00-120, (d) 29/03-123, (e) 29/06-126, and (f) 29/09-129 from the WRF 1.667-km resolution domain. 250-km radius is indicated by dotted circle. Horizontal and vertical axes indicate the distance (km) from the TC vortex center.

Our case study of Sandy suggests that the upper-level dynamic instabilities may facilitate the re-intensification of TCs during ET. The development of outflow channel due to the upper-level dynamic instabilities enhances the secondary circulation of Sandy, based on the mass continuity.

4.8 Sensitivity simulations

Results from the above sections show that *the northwestward movement of Sandy during the re-intensification stage increases inertial and symmetric instabilities of the outflow layer, leading to the re-intensification.* In other words, *if the storm does not recurve and keeps moving northeastward, the storm would be less influenced by the upper-level jet stream, and there would be no re-intensification.* To test this hypothesis two sensitivity experiments are performed, while keeping the identical physics options and domain configurations to the control simulation described in Chapters 3 and 4. They are shown in Table 1.

Table 1. Model configurations used for sensitivity experiments

Experiment name	PV50 run	PV100 run
Physics options	Identical to the control simulation	
Resolution	45/15/5/1.667 km Identical to the control simulation	
Grid dimension	Identical to the control simulation	
Initial and boundary condition	NCEP final analysis with bogussing scheme Identical to the control simulation	

SST	Uniformly specified as 27.25 °C (AVHRR-SST)	
Model integration time	0000 UTC 27 to 1800 UTC 29 October	
Initial field modification	Add 50 % of the upper-level PV perturbation	Add 100 % of the upper-level PV perturbation

The two sensitivity experiments are initialized at 0000 UTC 27 and ended at 1800 UTC 29 October. In these experiments, the PV inversion methodology (Davis and Emanuel 1991) is applied to change the track of Sandy, and SST is set to 27.25°C uniformly to remove the possible impact of SST (or CAPE) on the intensity change. By adding 50 and 100 % of the upper-level PV perturbation in the initial field, the trough in the central US is enhanced as shown in Fig. 4.13. Hereafter, the experiment with adding 50 % (100 %) of the PV perturbation is defined as the 50PV run (100PV run).

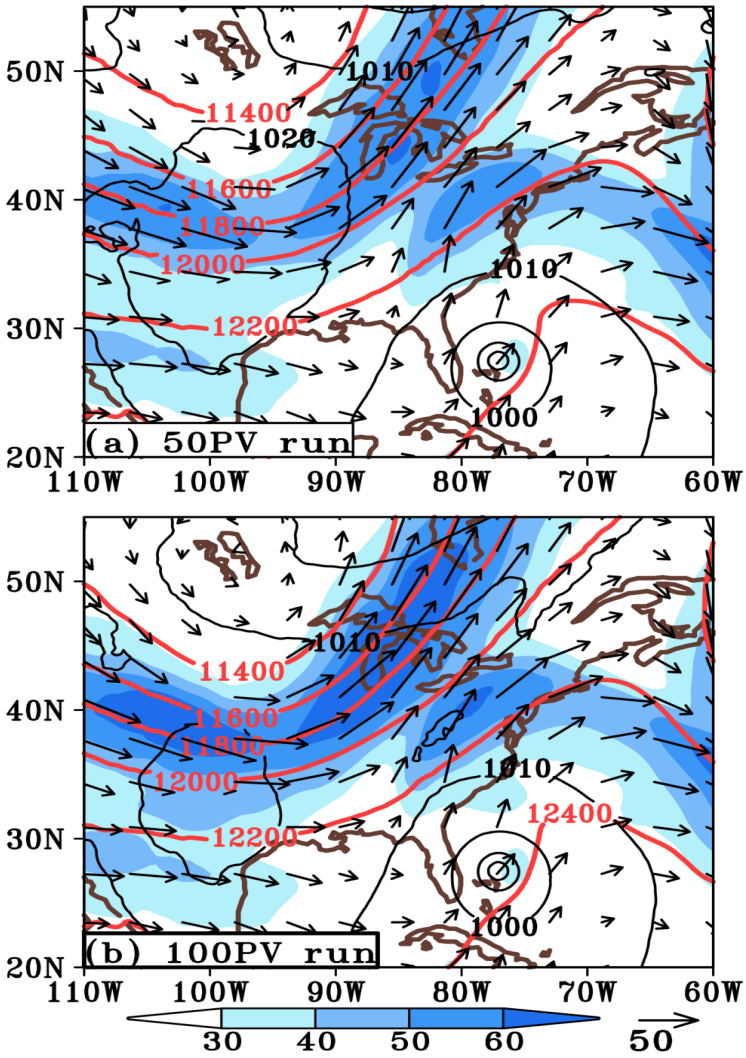

Figure 4.13. Geopotential height (red-contoured at intervals of 200 m), wind speed (shaded, m s^{-1}) and horizontal wind vectors at 200 hPa at the model initial time (0000 UTC 27 October 2012) for (a) 50PV run, and (b) 100PV run. Data from the WRF 45-km resolution domain are used.

The track of simulated storm in the 50PV run shows the northwestward movement, similar to the observation, but the 100PV run does not (Fig. 4.14). Because the storm of the 100PV run recurves much later than that of the 50PV run (or current simulation), we may expect this storm to be less affected by inertial and symmetric instabilities, which are generated by the upper-level jet stream. As shown in Fig. 4.15, the synoptic situation on 29 October from these experiments already implies that the distance between the storm and upper-level jet stream (and trough) is larger in the 100PV run than the 50PV run.

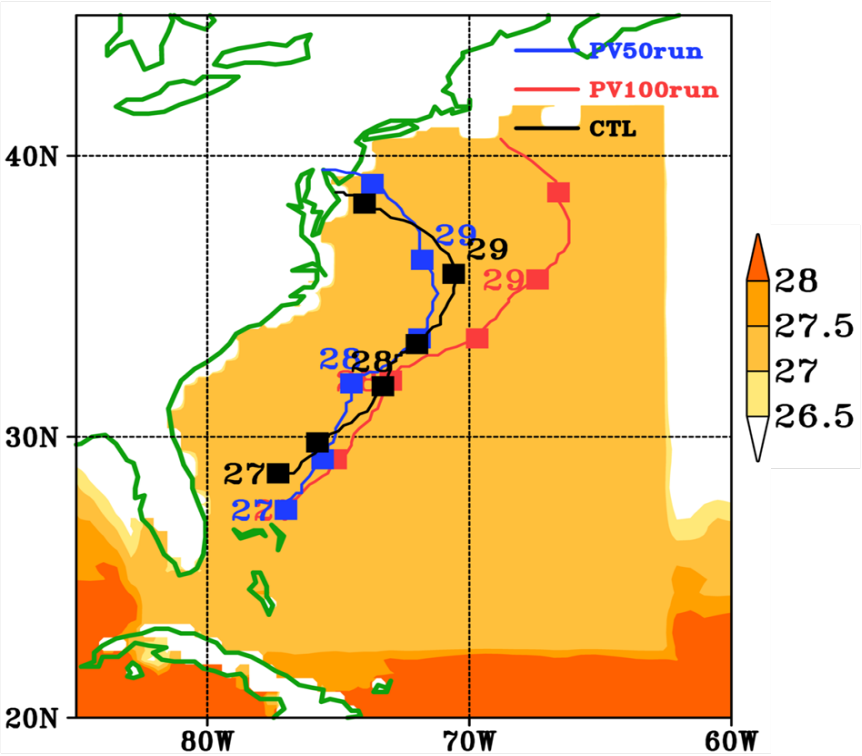

Figure 4.14. Comparison of the simulated track (50PVrun: blue, 100PVrun: red) to the control simulation (black) of Hurricane Sandy during the period of 0000 UTC 27 to 1800 UTC 29 October 2012, superimposed with the SST (shaded, °C) distribution. Data from the WRF 15-km resolution domain are used.

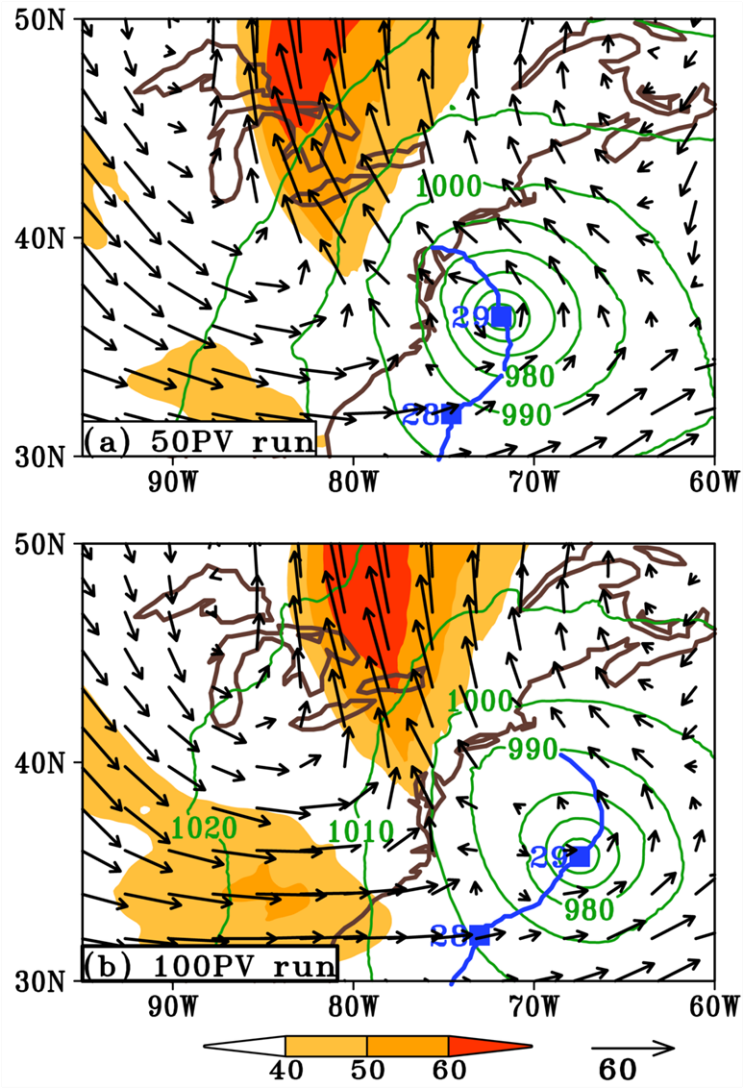

Figure 4.15. Horizontal distribution of isobars (green-contoured at intervals of 10 hPa), wind speed (shaded, m s^{-1}) and horizontal wind vectors at z = 9 km (near 300-hPa level), at 0000 UTC 29 October for (a) 50PV run, and (b) 100PV run. Data from the WRF 15-km resolution domain are used.

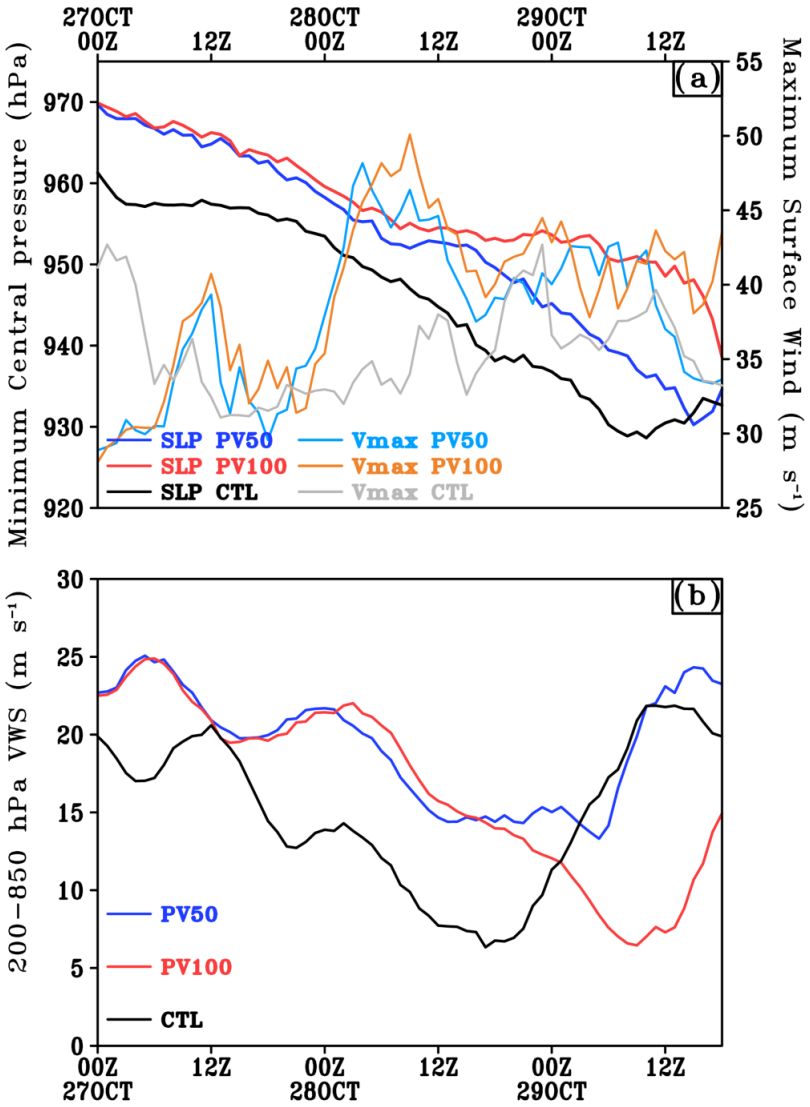

Figure 4.16. (a) Time series of the simulated minimum central pressure (PV50run: dark blue, PV100run, red, black: control run) and maximum surface wind (PV50run: light blue, PV100run, orange, gray: control run) during the period of 0000 UTC 27 to 1800 UTC 29 October 2012. Note that maximum surface wind is obtained within a 300 km radius from Sandy's vortex (b) Time series of (1000 km × 1000 km) area-averaged vertical wind shears (PV50run:dark blue, PV100run, red, black: control run) in the 200-850 hPa layer. Data from the WRF 15-km resolution domain are used.

The storm of the PV50run is much deeper than that of PV100run after 29 October, although two sensitivity runs show similar 10-m wind speed during this period (Fig. 4.16a). The vortex of the 50PV run exhibits stronger intensity than that of the 100PV run after 0000 UTC 29 October, that is, the storm intensifies more in the 50PV run in spite of strong VWS (Figs. 4.16b and 4.17).

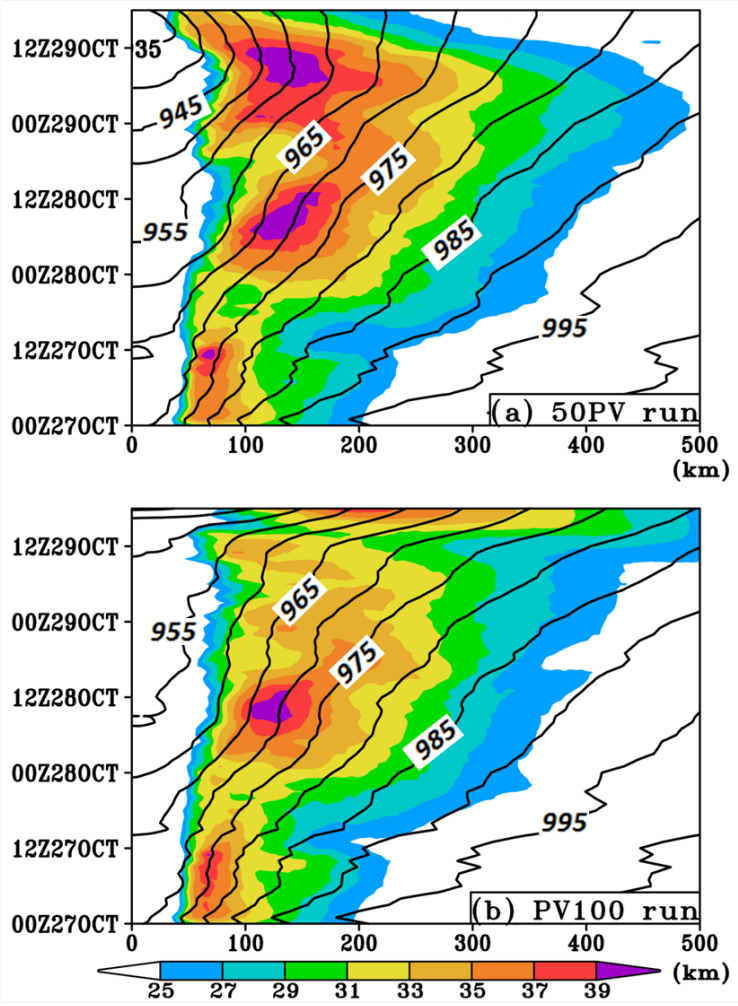

Figure 4.17. Time-radius cross section of the azimuthally averaged tangential wind speeds (shaded, m s^{-1}) at z = 0.5 km and SLP (contoured at 5-hPa intervals) for (a) 50PV run, and (b) 100PV run. Data from the WRF 1.667-km resolution domain are used.

Because the storm is more intense when it is closer to the upper-level jet stream, we are going to compare (i) inertial and symmetric instabilities of the outflow layer, (ii) CAPE, (iii) moist frontogensis process, and (iv) the impact of merging the frontal rainband and eyeall convection on Sandy's re-intensification. If the storm in the 50PV run intensifies under (i) more symmetrically and inertially unstable conditions, and (ii) more hostile conditions (i.e., low CAPE and high VWS) than the 100PV run, the result will firmly support the conclusion what we obtained from the present dissertation.

4.9. Chapter summary

In the second part of the study, we have investigated kinematic, physical features, as well as dynamic instabilities of the outflow layer, and its impact on the intensity change. When TC convection is intense, or as an upper-level trough approaches, isentropes above the outflow layer (or tropopause) slope downward with radius. This isentrope distribution results in weak subsidence above the outflow layer. The level of the maximum outward radial velocity is present above that of maximum cloud mixing ratio, i.e., above the cloud top. As a result, radiative cooling does not affect above the outflow channel. This implies that the descending motion above the outflow layer is not influenced by the radiative cooling. Additionally, when cirrus shields develop in the outflow channel, the detrainment of dry environment air generates weak subsidence at the edge of cloud via the evaporative cooling.

Based on the stratified characteristic of the outflow layer, its flow pattern is distinguished by a certain range of θ_e. Because Sandy has two convective regions

(i.e., associated with the outer frontal rainband and eyewall convection), it has two to three outflow channels by the time it moves to the midlatitudes. The outflow channel rooted in the outer frontal rainband has relatively lower θ_e values than the outflow layer originated from the eyewall convection. When Sandy undergoes re-intensification, it has two outflow channels in the range of 342~350K, and 350~358K, which are originated from the eyewall convection. At 24 hours before the re-intensification (i.e., at 28/00-96), the former is located in the northeastern quadrant and acts as the outflow channel for the frontogenesis region. However, during the next 24 hours, i.e., between 28/00-96 and 29/00-120, the 342-350-K outflow layer propagates to the northwestern quadrant, becoming the outflow channel of the eyewall convection, and simultaneously the upper-level jet stream approaches to the storm from the west. Between 29/00-120 and 29/09-129, during the re-intensification process, the upper-tropospheric jet stream generates the negative absolute vorticity in the outer region and the outward tilting of AAM surfaces in the inner region, respectively. This effect creates dynamic instabilities (i.e., inertial and symmetric instability) in the 342-350-K layer, allowing the acceleration of the outflow channel. Due to a symmetric instability within 500-km radius, the 342-350-K outflow layer exhibits slantwise outflow, which could be a unique characteristic of Sandy. It appears that the northwestward movement of Sandy on 29 October causes the merging of the eyewall convection and frontogenesis region (i.e., baroclinic zone associated with the upper-level jet stream), increasing symmetric instability, which is quite similar to that shown in Galarneau et al. (2013). Radial outward mass flux and layer-averaged radial outward velocity increase rapidly in the northwestern quadrant

on early 29 October. Inward mass flux in the boundary layer and vertical mass flux increase simultaneously, despite the increases in VWS, while CAPE decreases. These results simply that in the re-intensification stage the secondary circulation enhances in response to the acceleration of the outflow due to dynamic instabilities. In short, it appears that Sandy's re-intensification process is driven by the upper-level dynamic instabilities. The fact that the storm stops intensifying when dynamic instabilities disappear also implies the importance of the upper-level process.

The relationship between radiative cooling and symmetric instability is examined by analyzing the slopes of isentrope and AAM, and Ri_m. Low Ri_m is frequently observed near the slantwise outflow region, where the slope of isentrope is steeper than that of AAM surfaces. Within the 342-350-K outflow layer near 250- and 500-km radii, there is a thick layer, where Ri_m is below 1. This layer is located beneath a strong local radiative cooling layer, suggesting that this diabatic process results in symmetric instability ($Ri_m < 1$) via reducing the static stability in those areas. Although the upper-level jet stream mainly contributes to the generation of symmetric instability through the tilting of AAM surfaces, the radiative cooling also generates such instability locally by changing the static stability (i.e., isentrope slopes).

Chapter 5. Summary and future work

5.1. Summary of the research

This study examines the life cycle of Hurricane Sandy and factors that cause an unusual structural and intensity changes of the storm. The first part of study (Chapter 3) shows that Sandy has four distinct stages during its life cycle; rapid intensification (RI), weakening, steady-V_{MAX} and, re-intensification stages. During the RI stage while the central pressure decreases, the maximum wind speed increases and the opposite changes happen during the following weakening stage. That is, during the first two stages of Sandy, the storm follows a typical wind-pressure relationship. However, the maximum wind speed does not increase during the steady-V_{MAX} stage, it increases during the following re-intensification stage, even though the central pressure continues to decrease. This unusual wind-pressure relationship is caused by the unusual structural change of Sandy in responding to the interaction with midlatitude synoptic systems.

After the weakening stage, i.e., as Sandy enters the midlatitude region, it is affected by the lower-stratospheric warmth associated with tropopause undulation and low-level cold dry air related to an East Canadian High. Strong lower-stratospheric warming results in widespread surface pressure falls, expanding the low pressure area of the storm. As a result, during the steady-V_{MAX} stage, the radial pressure gradient does not increase, even though the central pressure decreases. This effect inhibits the inward absolute angular momentum (AAM) advection in the boundary layer, suppressing the intensification of storm's wind field. Simultaneously, the interaction

between the cold dry air associated with the eastern Canadian high and the storm causes continuous frontogenesis in the outer region, expanding the wind field of Sandy during the last two stages. During the re-intensification stage the eyewall convection invigoration and the merging of two remained frontogenesis regions intensify the horizontal wind field in the northern semicircle. The results suggest that (i) the intensity and structural changes of Sandy are determined by the lower-stratospheric warmth and low-level frontogenesis, and (ii) the eyewall convection plays a role in the re-intensification of the storm. Hydrostatic analysis reveals that the lower-stratospheric warmth above tropopause undulation region can affect the SLP field of transforming TCs. Although previous studies (Hirschberg and Fritsch 1991a, b; Velden 1992) showed the relationship between lower-stratospheric warm air and extratropical cyclone development, this research suggests that this warm air could also be important during the ET of TCs.

The second part of this study (i.e., Chapter 4) focuses on the outflow channel of the eyewall during the last two stages. Because Sandy has the frontal convection in the outer region and the eyewall convection in the core region, it has multiple outflow layers. To distinguish outflow channels which have different origins (frontal convection vs eyewall convection), outflow layers are sorted by the equivalent potential temperature (θ_e) because of its conservative property under saturated conditions. The outflow channel associated with the central eyewall convection has higher θ_e values than those in the outflow that is originated from the outer frontal convection. In other words, the outflow channels may be stratified as a warmer outflow layer of the eyewall convection above a colder outflow channel rooted in the

frontal rainband. These multiple outflow structures seem to be different from those shown by Emanuel and Rotunno (2011), who focused on the self stratification of eyewall's outflow. This stratified structure suggests that unlike mature TCs the storm that undergoes ET may exhibit multiple outflow layers.

Due to strong eyewall convection or approaching trough, isentropes above the outflow layer exhibits an upward bulge pattern, causing weak descending motion at this altitude. The axis of the outflow channel is located just above the cloud top where the radiative cooling effect is large. As Sandy moves northwestward during the re-intensification stage, the outflow layer of the eyewall convection is influenced by the upper-level jet stream. The upper-tropospheric jet stream generates the negative absolute vorticity in the outer region and the outward tilting of AAM surfaces in the inner region, respectively. As a result, the outer (inner) portion of the outflow layer becomes inertially (symmetrically) unstable, facilitating the outward acceleration of the outflow. Simultaneously the environment becomes hostile (i.e., low CAPE and high VWS), but the storm's secondary circulation keeps intensifying. When Sandy reaches the end of re-intensification stage, dynamic instabilities of the outflow layer disappears, and the storm ceases intensifying, which is similar to Morinali and Vollaro (2014). The re-intensification in the hostile environment strongly suggests that the impact of dynamic instabilities overcomes this condition, and facilitates Sandy's re-intensification through increased upward mass fluxes. While previous ET studies (Klein et al. 2002; Evans and Prater-Mayes 2004) focused on the divergence effect near the entrance region of an upper-level jet stream, this study examines the impact of dynamic instabilities induced by an upper-level jet stream on the re-

intensification of a TC during its ET. Also it seems that the upper tropospheric jet stream may affect the AAM fields in the upper level, which could be different from mature TCs as shown in Molinari et al. (2014). Thus, we may emphasize the important role of outflow layer's instabilities in the intensity changes of the storm. In summary, the outflow and intensity changes of transforming TCs appear to be influenced by dynamic instabilities.

In addition, from the moist Richardson number analysis, it is found that the radiative cooling at the cloud top reduces the stability of the outflow layer, contributing the formation of symmetric instability. Thus, it seems that radiative cooling affects the dynamic instabilities of the outflow layer as hypothesized by Dunion et al. (2014) and Morinali and Vollaro (2014). But the long-wave radiative cooling at the cloud top may play dominant roles in this process which is different from that discussed by Morinali and Vollaro (2014).

5.2. Future work.

Although in the present study we have examined the dynamic and physical processes leading to the structural and intensity changes of Sandy, several challenging issues remain to be addressed, due to highly nonlinear scale interactions among the processes. For example, what drives the broad scale inflows causing the expansion of the storm size, given the widespread SLP fall and moist frontogenesis? How do various dynamical instabilities in the upper outflow layer affect the mass fluxes in the eyewall, eventually determining the intensity changes of Sandy? To address properly the above questions, the following research tasks will be carried out:

1) Quantify the processes that drive the broad scale inflow during the steady-V_{MAX} stage and the intense inflow during the re-intensification phase through AAM budget and frontogenesis analysis. It is hypothesized that the PBL inflow is driven by deep convection in both the eyewall and frontal rainbands but their relative importance may differ during the two stages.

2) Examine moist frontogenesis when uniform SST is assumed in sensitivity simulations, as shown in chapter 4.8. Analyses of the sensitivity simulations will allow us to see to what extent the Gulf Stream affects the storm development, as claimed by Galarneau et al (2013).

3) Investigate the development of dynamical stability of the upper-level jet stream in relation to Sandy's intensity and structural changes from the sensitivity tests, as shown in chapter 4.8. We hypothesize that merging between the eyewall convection and frontal rainbands may not be significant in the PV100 run, because of the northeastward displacement of the storm, as compared to the control simulation. Since the merging process results in symmetric instability of the eyewall outflow channel, we would expect symmetric instability to be weaker in the PV100 run. Moreover, the larger distance between the storm and upper-level jet stream of the PV100 run would result in weaker inertial instability of the upper outflow layer. Thus, we may expect the storm in the PV100 run to be weaker than that of the PV50 run due to weak dynamic instabilities of the outflow layer.

In this study, we have simulated a series of moist frontogenesis events, but these events could not be verified by detailed observations over the vast oceans. So we may wait to obtain more observations, even from field observations to verify our simulated results. More case studies could also be conducted to examine the ET of TCs in which moist frontogenesis interacts with the tropopause undulation.

Bibliography

Atallah, E., and L. F. Bosart, 2003: The extratropical transition and precipitation distribution of Hurricane Floyd (1999). *Mon. Wea. Rev.*, **131,** 1063–1081.

Barnes, E. A., L. M. Polvani, and A. H. Sobel, 2013: Model projections of atmospheric steering of Sandy-like superstorms. *Proc. Natl. Acad. Sci. USA,* **110,** 15211–15215.

Bassill, N. P., 2015: An analysis of the operational GFS simplified Arakawa Schubert parameterization within a WRF framework: A Hurricane Sandy (2012) long-term track forecast perspective. *J. Geophys. Res. Atmos.*, **120**, 378–398.

Black, M. L., J. F. Gamache, and Co-authors, 2002: Eastern Pacific Hurricanes Jimena of 1991 and Olivia of 1994: The effect of vertical shear on structure and intensity. *Mon. Wea. Rev.*, **130,** 2291–2312.

Blake, E. S., T. B. Kimberlain, and Co-authors, 2013: National Hurricane CenterTropical Cyclone Sandy Preliminary Report. 157pp. (Available from NHC webpage http://www.nhc.noaa.gov/2012atlan.shtml)

Bosart, L. F., and G. M. Lackmann, 1995: Postlandfall tropical cyclone reintensification in a weakly baroclinic environment: A case study of Hurricane David (September 1979). *Mon. Wea. Rev*, **123,** 3268–3291.

Browning, K. A., G. Vaughan, and P. Panagi, 1998: Analysis of an ex-tropical cyclone after reintensifying as a warm-core extratropical cyclone. *Quart. J. Roy. Meteor. Soc.*, **124,** 2329–2356.

Bu, Y. P., R. Fovell, and K. L. Corbosiero, 2014: Influence of cloud–radiative forcing on tropical cyclone structure. *J. Atmos. Sci.,* **71,** 1644–1662.

Carrasco, C. A., C. W. Landsea, and Y.-L. Lin, 2014: The influence of tropical cyclone size on its intensification. *Wea. Forecasting*, **29,** 582–590.

Cecelski, F. S., and D.-L. Zhang, 2013: Genesis of Hurricane Julia (2010) within an African easterly wave: Low-level vortices and upper-level warming. *J. Atmos. Sci.*, **70,** 3799–3817.

Chen, H., and D.-L. Zhang, 2013: On the rapid intensification of Hurricane Wilma (2005). Part II: Convective bursts and the upper-level warm core. *J. Atmos. Sci.,* **70,** 146–162.

Colle, B. A., 2003: Numerical simulations of the extratropical transition of Floyd (1999): Structural evolution and responsible mechanisms for the heavy rainfall over the northeast United States. *Mon. Wea. Rev.*, **131,** 2905–2926.

Davis, C. A., and K. E. Emanuel, 1991: Potential vorticity diagnostics of cyclogenesis. *Mon. Wea. Rev.*, **119,** 1929–1953.

_____, S. C. Jones, and M. Riemer, 2008: Hurricane vortex dynamics during Atlantic extratropical transition. *J. Atmos. Sci.*, **65,** 714–736.

_____, W. Wang, S. S. Chen, Y. Chen, and Coauthors, 2008: Prediction of landfalling hurricanes with the Advanced Hurricane WRF Model. *Mon. Wea. Rev.*, **136,** 1990–2005.

Donelan, M. A., B. K. Haus, N. Reul, W. J. Plant, and Co-authors, 2004: On the limiting aerodynamic roughness of the ocean in very strong winds. *Geophys. Res. Lett.*, **31,**L18306, doi:10.1029/2004GL019460.

Dudhia, J., 1989: Numerical study of convection observed during the winter monsoon experiment using a mesoscale two-dimensional model. *J. Atmos. Sci.*, **46,** 3077-3107.

Dunion, J. P., C. D. Thorncroft, and C. S. Velden, 2014: The tropical cyclone diurnal cycle of mature hurricanes. *Mon. Wea. Rev.*, **142**, 3900–3919.

Durran, D. R., and J. B. Klemp, 1982: On the effects of moisture on the Brunt-Väisälä frequency. *J. Atmos. Sci.*, **39**, 2152–2158.

Duran, P.D., and J. Molinari, 2016: Upper-tropospheric low Richardson number in tropical cyclones: Sensitivity to cyclone intensity and the diurnal cycle. *J. Atmos. Sci.*, in press.

Emanuel, K. A., 1986: An air–sea interaction theory for tropical cyclones. Part I: Steady-state maintenance. *J. Atmos. Sci.*, **43,** 585–605.

_____, and R. Rotunno, 2011: Self-stratification of tropical cyclone outflow. Part I: Implications for storm structure. *J. Atmos. Sci.*, **68,** 2236–2249.

Evans, J. L., and B. E. Prater-Mayes, 2004: Factors affecting the posttransition intensification of Hurricane Irene (1999). *Mon. Wea. Rev.,* **132,** 1355–1368.

Evans, J. L., and R. E. Hart, 2003: Objective indicators of the life cycle evolution of extratropical transition for Atlantic tropical cyclones. *Mon. Wea. Rev.*, **131,** 909–925.

Evans, C., and R. E. Hart, 2008: Analysis of the wind field evolution associated with the extratropical transition of Bonnie (1998). *Mon. Wea. Rev.*, **136,** 2047–2065.

Frank, W. M., and E. A. Ritchie, 1999: Effects of environmental flow upon tropical cyclone structure. *Mon. Wea. Rev.*, **127,** 2044–2061.

Galarneau, T. J., C. A. Davis, and M. A. Shapiro, 2013: Intensification of Hurricane Sandy (2012) through extratropical warm core seclusion. *Mon. Wea. Rev.*, **141,** 4296–4321.

Harr, P. A., and R. L. Elsberry, 2000: Extratropical transition of tropical cyclones over the Western North Pacific. Part I: Evolution of structural characteristics during the transition process. *Mon. Wea. Rev.*, **128,** 2613–2633.

Heymsfield, G. M., J. B. Halverson, J. Simpson, L. Tian, and T. P. Bui, 2001: ER-2 Doppler radar investigations of the eyewall of Hurricane Bonnie during the Convection and Moisture Experiment-3. *J. Appl. Meteor.*, **40,** 1310–1330.

Hill, K. A., and G. M. Lackmann, 2009: Influence of environmental humidity on tropical cyclone size. *Mon. Wea. Rev.*, **137**, 3294–3315.

Hirschberg, P. A., and J. M. Fritsch, 1991a: Tropopause undulations and the development of extratropical cyclones. Part I: Overview and observations from a cyclone event. *Mon. Wea. Rev.*, **119,** 496–517.

____, and____, 1991b: Tropopause undulations and the development of extratropical cyclones. Part II: Diagnostic analysis and conceptual model. *Mon. Wea. Rev.*, **119,** 518–550.

Hong, S.-Y., J. Dudhia, and S.-H. Chen, 2004: A revised approach to ice microphysical processes for the bulk parameterization of clouds and precipitation. *Mon. Wea. Rev.*, **132,** 103–120.

____, and J.-O. Lim, 2006: The WRF single-moment 6-class microphysics scheme (WSM6). *J. Korean Meteor. Soc.*, **42,** 129–151.

____, Y. Noh, and J. Dudhia, 2006: A new vertical diffusion package with an explicit treatment of entrainment processes. *Mon. Wea. Rev.*, **134,** 2318–2341.

Johnson, R. H., W. A. Gallus Jr., and M. D. Vescio. 1990. Near-tropopause vertical motion within the trailing-stratiform region of a midlatitude squall line. *J. Atmos. Sci.,* **47,** 2200–2210.

Jones, S. C., P. A. Harr, J. Abraham, L. F. Bosart, and Coauthors, 2003: The extratropical transition of tropical cyclones: Forecast challenges, current understanding, and future directions. *Wea. Forecasting*, **18**, 1052–1092.

Kain, J. S., 2004: The Kain-Fritsch convective parameterization: An update. *J. Appl. Meteor.*,**43,** 170-181.

Kaplan, J., and M. DeMaria, 2003: Large-scale characteristics of rapidly intensifying tropical cyclones in the North Atlantic basin. *Wea. Forecasting,* **18,** 1093–1108.

Keyser, D., M. J. Reeder, and R. J. Reed, 1988: A generalization of Petterssen's frontogenesis function and its relation to the forcing of vertical motion. *Mon. Wea. Rev.,* **116,** 762–780.

Kieu, C. Q., and D.-L. Zhang, 2008: Genesis of tropical storm Eugene (2005) from merging vortices associated with ITCZ breakdowns. Part I: Observational and modeling analyses. *J. Atmos. Sci.*, **65,** 3419–3439.

Klein, P. M., P. A. Harr, and R. L. Elsberry, 2000: Extratropical transition of Western North Pacific tropical cyclones: An overview and conceptual model of the transformation stage. *Wea. Forecasting*, **15,** 373–395.

Klein, P. M., P. A. Harr, and R. L. Elsberry, 2002: Extratropical transition of Western North Pacific tropical cyclones: Midlatitude and tropical cyclone contributions to reintensification. *Mon. Wea. Rev.,* **130,** 2240–2259.

Knapp, K. R., S. Ansari, C. L. Bajn, M. A. Bourassa, and Coauthors, 2011: Globally gridded satellite observations for climate studies. *Bull. Amer. Meteor. Soc.*, **92**, 893–907.

Koteswaram, P, 1967: On the structure of hurricanes in the upper troposphere and lower stratosphere. *Mon. Wea. Rev.,* **95,** 541–564.

Kovacs, T. A., and M. P. McCormick, 2003: Observations of Typhoon Melissa during the Lidar In-Space Technology Experiment (LITE). *J. Appl. Meteor.,* **42,** 1003–1013.

Kwon, I.-H., and H.-B. Cheong, 2010: Tropical cyclone initialization with a spherical high-order filter and an idealized three-dimensional bogus vortex. *Mon. Wea. Rev.*, **138,** 1344–1367.

Lackmann, G. M, 2015: Hurricane Sandy before 1900 and after 2100. *Bull. Amer. Meteor. Soc.,* **96**, 547–560.

Leroux, M.-D., M. Plu, D. Barbary, F. Roux, and P. Arbogast, 2013: Dynamical and physical processes leading to tropical cyclone intensification under upper-level trough forcing. *J. Atmos. Sci.*, **70**, 2547–2565.

Liu, Y., D.-L. Zhang, and M. K. Yau, 1999: A multiscale numerical study of Hurricane Andrew (1992). Part II: Kinematics and inner-core structures. *Mon. Wea. Rev.,* **127,** 2597–2616.

Magnusson, L., J.-R. Bidlot, S. T. K. Lang, A. Thorpe, and N. Wedi, 2014: Evaluation of medium-range forecasts of Hurricane Sandy. *Mon. Wea. Rev.,* **142**, 1962–1981.

Melhauser, C., and F. Zhang, 2014: Diurnal radiation cycle impact on the pre-genesis environment of Hurricane Karl (2010). *J. Atmos. Sci.*, **71**, 1241–1259.

Mlawer, E. J., S. J. Taubman, and Co-authors, 1997: Radiative transfer for inhomogeneous atmospheres: RRTM, a validated correlated-*k* model for the longwave. *J. Geophys. Res.*, **102,** 16663–16682.

Molinari, J., and D. Vollaro, 1989: External influences on hurricane intensity: Part I. Outflow layer eddy angular momentum fluxes. *J. Atmos. Sci.*, **46**, 1093–1105.

Molinari, J., and D. Vollaro, 2014: Symmetric instability in the outflow layer of a major hurricane. *J. Atmos. Sci.*, **71**, 3739–3746.

Molinari, J., P. Dodge, D. Vollaro, K. L. Corbosiero, and F. Marks Jr., 2006: Mesoscale aspects of the downshear reformation of a tropical cyclone. *J. Atmos. Sci.*, **63,** 341–354.

Molinari, J., P. Duran, and D. Vollaro, 2014: Low Richardson number in the tropical cyclone outflow layer. *J. Atmos. Sci.*, **71**, 3164–3179.

Mrowiec, A.A., O. M. Pauluis and F. Zhang, 2016: Isentropic analysis of a simulated hurricane. *J. Atmos. Sci.*, **73**, 1857-1870.

Newman, S., and J. G. Boyd, 1962: Hurricane movement and variable location of high intensity spot in wall cloud radar echo. *Mon. Wea. Rev.,* **90,** 371–374.

Pauluis, O. M., and A. A. Mrowiec, 2013: Isentropic analysis of convective motions. *J. Atmos. Sci.*, **70**, 3673–3688.

Powell, M. D., 1990a: Boundary layer structure and dynamics in outer hurricane rainbands. Part I: Mesoscale rainfall and kinematic structure. *Mon. Wea. Rev.,***118,** 891–917.

_____, 1990b: Boundary layer structure and dynamics in outer hurricane rainbands. Part II: Downdraft modification and mixed layer recovery. *Mon. Wea. Rev.,* **118,** 918–938.

_____, S. H. Houston, L. R. Amat, and N Morisseau-Leroy, 1998: The HRD real-time hurricane wind analysis system. *J. Wind Engineer. And Indust. Aerodyn.***77&78,** 53-64.

Rappin, E. D., M. C. Morgan, and G. J. Tripoli, 2011: The impact of outflow environment on tropical cyclone intensification and structure. *J. Atmos. Sci.*, **68**, 177–194.

Reasor, P. D., M. T. Montgomery, and L. D. Grasso, 2004: A new look at the problem of tropical cyclones in vertical shear flow: Vortex resiliency. *J. Atmos. Sci.*, **61,** 3–22.

Reuter, G. W., and M. K. Yau, 1990: Observations of slantwise convective instability in winter cyclones. *Mon. Wea. Rev.*, **118,** 447–458.

Riemer, M., M. T. Montgomery, and M. E. Nicholls, 2010: A new paradigm for intensity modification of tropical cyclones: thermodynamic impact of vertical wind shear on the inflow layer. *Atmos. Chem. Phys.,* **10,** 3163-3188.

Ritchie, E. A., and R. L. Elsberry, 2007: Simulations of the extratropical transition of tropical cyclones: Phasing between the upper-level trough and tropical cyclones. *Mon. Wea. Rev.*, **135,** 862–876.

Rodts, S. M. A., P. G. Duynkerke, and H. J. J. Jonker, 2003: Size distributions and dynamical properties of shallow cumulus clouds from aircraft observations and satellite data. *J. Atmos. Sci.*, **60,** 1895–1912.

Seltzer, M. A., R. E. Passarelli, and K. A. Emanuel, 1985: The possible role of symmetric instability in the formation of precipitation bands. *J. Atmos. Sci.*, **42,** 2207–2219.

Shapiro, M. A., and D. Keyser, 1990: Fronts, jet streams, and the tropopause. *Extratropical Cyclones: The Erik Palmén Memorial Volume,* C. W. Newton and E. O. Holopainen, Eds., *Amer. Meteor. Soc.,* 167–191.

Sitkowski, M., J. P. Kossin, and C. M. Rozoff, 2011: Intensity and structure changes during hurricane eyewall replacement cycles. *Mon. Wea. Rev.*, **139,** 3829–3847.

Skamarock, W. C., J. B. Klemp, J. Dudhia, D. O. Gill, and Coauthors, 2008: A description of the Advanced Research WRF version 3. NCAR Tech. Note NCAR/TN-475+STR, 125 pp.

Tang, X., and F. Zhang, 2016: Impacts of the Diurnal Radiation Cycle on the Formation, Intensity and Structure of Hurricane Edouard (2014). *J. Atmos. Sci.*, in press.

Tao, W.-K., J. J. Shi, S. S. Chen, S. Lang, P.-L. Lin, S.-Y. Hong, C. P.- Lidard, and A. Hou, 2011: The impact of microphysical schemes on hurricane intensity and track. *Asia-Pacific J. Atmos. Sci.* **47(1),** 1-16.

Thorncroft, C. D., and S. C. Jones, 2000: The extratropical transitions of Hurricanes Felix and Iris in 1995. *Mon. Wea. Rev.*, **128,** 947–972.

Torn, R. D., J. S. Whitaker, P. Pegion, T. M. Hamill, and G. J. Hakim, 2015: Diagnosis of the source of GFS medium-range track errors in Hurricane Sandy (2012). *Mon. Wea. Rev.*, **143**, 132–152.

Vecchi, G., S. Fueglistaler, I. Held, T. Knutson, and M. Zhao, 2013: Impacts of atmospheric temperature trends on tropical cyclone activity. *J. Climate*, **26,** 3877–3891.

Velden, C., 1992: Satellite-based microwave observations of tropopause-level thermal anomalies: Qualitative application in extratropical cyclone events. *Wea. Forecasting*, **7,** 669–682.

Waco, D. E, 1970: Temperatures and turbulence at tropopause levels over hurricane Beulah (1967). *Mon. Wea. Rev.,* **98,** 749–755.

Wang, Y., 2009: How do outer spiral rainbands affect tropical cyclone structure and intensity? *J. Atmos. Sci*., **66,** 1250–1273.

Wang, S., S. J. Camargo, A. H. Sobel, and L. M. Polvani, 2014: Impact of the tropopause temperature on the intensity of tropical cyclones: An idealized study using a mesoscale model. *J. Atmos. Sci.*, **71,** 4333–4348.

Wang, Y., and B. Geerts, 2010: Humidity variations across the edge of trade wind cumuli: Observations and dynamical implications. *Atmospheric Research* **97**, 144-156.

Willoughby, H. E., J. Clos, and M. Shoreibah, 1982: Concentric eye walls, secondary wind maxima, and the evolution of the hurricane vortex. *J. Atmos. Sci.*, **39,** 395–411.

Yau, M.K., Y. Liu, D.-L. Zhang, and Y. Chen, 2004: A multiscale numerical study of Hurricane Andrew (1992). Part VI: Small-scale inner-core structures and wind streaks. *Mon. Wea. Rev.*, **132**, 1410-1433.

Zhang, D.-L., Y. Liu, and M. K. Yau, 2000: A multiscale numerical study of Hurricane Andrew (1992). Part III: Dynamically induced vertical motion. *Mon. Wea. Rev.*, **128,** 3772–3788.

____, and H. Chen, 2012: Importance of the upper-level warm core in the rapid intensification of a tropical cyclone. *Geophys. Res. Lett.*,**39,** L02806, doi:10.1029/2011GL050578.

____, and L. Zhu, 2012: Roles of upper-level processes in tropical cyclogenesis. *Geophys. Res. Lett.*,**39,** L17804, doi:10.1029/2012GL053140.

Zhu, T., D.-L. Zhang, and F. Weng, 2004: Numerical simulation of Hurricane Bonnie (1998). Part I: Eyewall evolution and intensity changes. *Mon. Wea. Rev.*, **132,** 225–241.

_____, and _____, 2006a: Numerical simulation of Hurricane Bonnie (1998). Part II: Sensitivity to cloud microphysical processes. *J. Atmos. Sci.*, **63,** 109–126.

____, and F. Weng, 2013: Hurricane Sandy warm-core structure observed from advanced Technology Microwave Sounder. *Geophys. Res. Lett.,***40,** 3325–3330, doi:10.1002/grl.50626.